Towards Analog Quantum Simulation of Dynamical Gauge Theories

by

Christopher Warren

A thesis
presented to the University of Waterloo
in fulfillment of the
thesis requirement for the degree of
Master of Science
in
Physics

Waterloo, Ontario, Canada, 2017

Author's Declaration

I hereby declare that I am the sole author of this thesis. This is a true copy of the thesis, including any required final revisions, as accepted by my examiners.

I understand that my thesis may be made electronically available to the public.

Abstract

A system which can implement an analog quantum simulation of lattice gauge theories has been proposed. In particular, the Schwinger model is formulated in terms of a lattice and superconducting qubit implementation is found which maps onto these dynamics. This thesis details the design of the superconducting circuit implementation of the model. The Hamiltonian of the superconducting circuit is designed to exhibit the gauge invariant dynamics of a U(1) symmetry. The gauge invariant set of states corresponds to those that are in the subspace of states that are shared by the Hamiltonian and the symmetry. Gauge invariance is simulated by looking at the dynamics of those states which obey a lattice version of Gauss' law.

The device is simulated in an open quantum system and the measurable observables are extracted and mapped onto processes which can be observed in the lab. We find that the dynamics occur over realistic time scales that can be observed with current laboratory equipment. These dynamics occur over hundred nanosecond timescales well within the minimum resolution of our equipment as well as well within the decoherence times of current superconducting devices.

Acknowledgements

Our experiments exist under vacuum that doesn't mean that our research needs to. That is the mentality I chose to pursue when I began my career in research. Nothing can get done without constructive and engaging collaboration. With that being said there are many individuals I would like to thank.

First, I would like to thanks my friends and family for their support and encouragement over the years. It has been incredibly useful to know that even if I never asked for it help would always be available for me.

I would also like to thank my fellow group members and friends, Helen, Vadiraj, Sandbo, and Ibrahim. Your friendship and guidance has pushed me along to where I am today. Your insightful conversations have helped to expand my experimental knowledge immensely after coming from a theoretical background. When I began my masters I barely knew how to approach experimental work, but your encouragement and patience has helped tremendously throughout.

I would like to extend special thanks to our ex-post-doc, Pol Forn-Díaz. Your insight has been incredible over the years I have known you and I have learned a tremendous amount working closely with you. The research we did has been some of the most fun that I have had and I know you will continue to do fantastic research in the future. Soccer has not been the same without you on the team.

I would like to extend thanks to our theory collaborator Enrique Rico. It was always a pleasure discussing the basics of the model with you and the possible extensions of the model. I could feel myself getting back to my undergraduate roots and feeling excited about the prospects whenever we talked. I thank you also for showing me such a fantastic time in Bilbao.

A non-exhaustive list of individuals I feel deserve a special shout-out include Guillaume Verdon, Jérémy Béjanin, Matt Brown, Ramy Tannous, Nachiket Sherlekar, Martin Laforest, Jeremy Flannery, Cliff Plesha, Kayla Hardie, Morgan Mastrovich, Dan Grimmer, Christian Mastromattei. I have certainly missed people who have helped me academically and personally at IQC, but this was sure to fail as everyone at IQC affects everyone else. That is just how the institute is.

Last but certainly not least I would like to thank my advisor Chris Wilson. For your hard work, dedication, and assistance in this project I would like to thank you. I would also like to thank you for showing me what it means to be so truly dedicated to a craft. Your intensity is inspiring.

Table of Contents

List of Figures

Chapter 1

Introduction

> ...because nature isn't classical, dammit, and if you want to make a simulation of nature, you'd better make it quantum mechanical, and by golly it's a wonderful problem, because it doesn't look so easy
>
> *Richard P. Feynman*

Quantum computing is often traced back to Richard Feynman's 1981 keynote address to the MIT Physics of Computation Conference[21] where he argued that what we think of as a classical computer is insufficient to adequately describe the full physical world. However, the origins of the field actually go back two years earlier to Paul Benioff[7] who created a Hamiltonian description Turing machine and later showed that this quantum Turing machine could simulate a classical computer[9, 8]. To Feynman's credit though he was the first person to really play with the idea that quantum mechanics could really do something new in terms of computability, that is quantum mechanics has access to a larger space of efficiently computable problems. The first hints that quantum computing offered something new came from David Deutsch and Richard Jozsa[18] where they discovered a class of problems which the fastest classical algorithm scaled exponentially with the size problem, but the quantum version could evaluate the problem with a single query. This opened the floodgates for computer scientists. They suddenly had a new ontological toy to play with and new rules to explore quickly leading to the much celebrated Shor's algorithm[60] and Grover's search[28]

algorithm. This expanded the field from Feynman's original proposal of simulating physics with physics.

There are two major goals of quantum computing. The first has been alluded to in the previous paragraph. The expansion of our understanding of computational complexity and what it means to be "efficiently" computable has driven much of the research in the field. With this comes the push for implementing these efficient algorithms on a physical quantum computer and understanding the limitations nature imposes on a physical system. The second goal of quantum computing is very much at the heart of the epigraph at the beginning of this chapter and is central to this thesis. To return to Feynman once again, the initial push for a quantum computer came from trying to understand the physical world just that little bit more and using nature's most fundamental mechanism to probe the world that little bit more. Quantum simulation is in my opinion a far more powerful tool in the quantum computing arsenal than many researchers realize or appreciate. The potential of this area of study opens avenues into understanding condensed matter physics[71, 43], chemistry[3, 37],high-energy particle physics[47, 44], and a range of other fields such as cosmology, and biology. This subtlety that we are moving into a new paradigm of computing is going to be beneficial across all of the sciences.

With all this theoretical work laid out the question now turns to how to implement these simulations. A very fashionable implementation of quantum computing is to use circuit quantum electrodynamics (cQED) and in particular superconducting qubits. They are attractive for several reasons. The first major reason is the top down perspective this implementation takes in terms of design. Rather than take an existing microscopic quantum system, such as a spin system in NMR, and force it to behave against the limitations imposed on it by Nature, the cQED approach is to take an engineered electrical circuit and force it into a situation where it behaves quantum mechanically. The second major reason is that these engineered systems are particularly scalable. In principle being able to design one circuit means being able to engineer hundreds (with some caveats). Variations due to fabrication procedures can be narrowed down to a few percent allowing for easy standardization of design. These two major features contribute immensely to the success of superconducting qubits over the last decade.

1.1 Thesis Overview

Often times we take for granted the tools we use in physics to achieve our research goals. This is even more apparent the more developed a field becomes. As more and more layers of knowledge are discovered we tend to glaze over previous results for the sake of brevity. I have found that this has a compounding effect on individuals trying to enter a new field. It is a difficult task to try and have a comprehensive understanding of why modern developments are well justified. In this thesis my aim is to qualify and justify each logical progression of the theory and experiment (in this I will surely fail, but nevertheless try).

I will begin this thesis by introducing our fundamental building blocks in our experimental architecture of circuit quantum electrodynamics beginning with superconductivity. I will show that superconductivity leads us to a description of a macroscopic wavefunction and argue that this description allows us to take the top down approach to engineering quantum systems rather than needing to revert to a microscopic perspective every time. From there I will introduce the key electrical elements of resonators, Josephson junctions and qubits which will form our quantum circuit.

Next I will outline the principles of lattice gauge theories and delve into the specific model we are trying to simulate experimentally; the Schwinger model. To do this I will outline how to define a mapping between the Schwinger model and our superconducting implementation that gives us an analog quantum simulator.

In the next chapter I will discuss the design of the qubits. I will explore the physical constraints that need to be designed to have a properly engineered Hamiltonian that exhibits the gauge invariant dynamics. I will also describe some of the methods used to engineer junctions and the capactiances of our circuits.

In my final chapter I will focus on the implementation of the design and show simulations of the dynamics we wish to observe in a physical experiment. I will propose an experimental setup as well as a protocol for initial state preparation that faithfully reproduces the sought after dynamics.

Chapter 2

Circuit Quantum Electrodynamics (cQED)

2.1 Superconductivity

Superconductivity was originally discovered trying to demonstrate the complete opposite effect in 1911 by Heike Kamerlingh Onnes. After becoming the first individual to successfully liquefy helium he began investigating how different materials behaved when they were cooled to extremely low temperatures. It was thought at the time that metals would not be able to support an electric current as the electrons would essentially be frozen in place at these temperatures and the resistance would become infinitely large. In fact he demonstrated the exact opposite of what he set out to prove. He showed for the first time in mercury that below a certain critical temperature ($T_c = 4.2K$ for mercury) the resistance dropped in his own words to "practically zero". He also at the same time as this experiment was performed demonstrated another transition in the superfluid transition of helium.[51] Fourteen years later the first mathematical treatments began to explain the transition into superconductivity and its properties from a classical electrodynamic depiction[40]. It was only during the middle of the 20th century that a fully microscopic description appeared first phenomenologically with Ginzburg-Landau theory[26] in 1950 then from a fully quantum mechanical derivation with BCS theory in 1957[5].

To truly understand the implications superconductivity has on macroscopic quantum computing implementations such as in cQED it is illustrative to show a derivation of the theory. The following derivation is adapted from Tinkham's "Introduction to Superconductivity"[64].

To begin consider a filled non-interacting Fermi sphere at $T = 0$. You can think of the

Fermi sphere intuitively as a sphere made up of lego blocks where each block represents an energy eigenstate of the space. In this analogy the lego blocks are spatially localized and two blocks cannot occupy more than one space as electrons are fermions and due to the Pauli exclusion principle two fermions cannot occupy the same state due to their anti-symmetry. Only a single fermion can occupy each energy eigenstate as opposed to a bosonic system where multiple bosons can occupy an eigenstate.

Now consider two interacting electrons added on top of this Fermi sea. The lowest energy eigenstate for this two particle problem must have zero total momentum. A particular ansatz to the Schrödinger equation has the form,

$$\psi(\vec{\mathbf{r}}_1, \vec{\mathbf{r}}_2) = \sum_{\vec{\mathbf{k}}} g(\vec{\mathbf{k}}) e^{i\vec{\mathbf{k}}\cdot\vec{\mathbf{r}}_1} e^{-i\vec{\mathbf{k}}\cdot\vec{\mathbf{r}}_2} \tag{2.1}$$

This expansion into plane waves implies $g(\vec{\mathbf{k}})$ is the probability amplitude of finding the two electrons with opposite momentum $\hbar\vec{\mathbf{k}}$ and $-\hbar\vec{\mathbf{k}}$. Since these electrons lie above the Fermi sea the probability of finding the electrons with a momentum, $\left|\vec{\mathbf{k}}\right|$ less than the Fermi momentum, $k_F = \sqrt{2m_e\hbar E_F}$, is zero. Using this wavefunction in the Schödinger equation (adding the energy cost of two electrons explicitly) gives,

$$-\frac{\hbar^2}{2m_e}\big(\nabla_1^2 + \nabla_2^2 + V(\vec{\mathbf{r}}_1, \vec{\mathbf{r}}_2)\big)\psi(\vec{\mathbf{r}}_1, \vec{\mathbf{r}}_2) = (E + 2E_F)\psi(\vec{\mathbf{r}}_1, \vec{\mathbf{r}}_2) \tag{2.2}$$

Substituting in the wavefunction gives in momentum space,

$$g(\vec{\mathbf{k}})(E + 2E_F - 2\epsilon_{\vec{\mathbf{k}}}) = \sum_{\vec{\mathbf{k}}'} g(\vec{\mathbf{k}}')V_{\vec{\mathbf{k}},\vec{\mathbf{k}}'} \tag{2.3}$$

where $\epsilon_{\vec{\mathbf{k}}} = \frac{\hbar^2 k^2}{2m_e}$ and $V_{\vec{\mathbf{k}},\vec{\mathbf{k}}'}$ is,

$$V_{\vec{\mathbf{k}},\vec{\mathbf{k}}'} = \Omega^{-1} \int V(\vec{\mathbf{r}}) e^{i(\vec{\mathbf{k}}' - \vec{\mathbf{k}})\cdot\vec{\mathbf{r}}} d\vec{\mathbf{r}} \tag{2.4}$$

with Ω as a normalization factor and $\vec{\mathbf{r}} = \vec{\mathbf{r}}_1 - \vec{\mathbf{r}}_2$ as the distance between the electrons. It now comes to analyze what the potential is. In Cooper's original work, motivated by the work of Bardeen, he made the approximation that the potential was $V_{\vec{\mathbf{k}},\vec{\mathbf{k}}'} = -V$ for the states $\vec{\mathbf{k}}$ and to some cutoff energy $\hbar\omega_c$. Equation 2.3 now reduces into the form,

$$g(\vec{\mathbf{k}})(E + 2E_F - 2\epsilon_{\vec{\mathbf{k}}}) = -V\sum_{\vec{\mathbf{k}}'} g(\vec{\mathbf{k}}') \text{ for } E_F \leq \epsilon_{\vec{\mathbf{k}}'} < E_F + \hbar\omega_c \tag{2.5}$$

Summing both side over $\vec{\mathbf{k}}$ now gives,

$$\frac{1}{V} = \sum_{k>k_F} (2\epsilon_{\vec{\mathbf{k}}} - E - E_F)^{-1} \tag{2.6}$$

Taking the momentum states to be a continuum changes this into an integral. Making the substitution $\eta = \epsilon - E_F$ and the substitution of the density of states for an isotropic spherical system, $N(\eta) = (k^2/2\pi^2)(d\eta/dk)^{-1}$, equation 2.6 can now be written,

$$\frac{1}{V} = \int_0^{\hbar\omega_c} d\eta \frac{N(\eta)}{2\eta - E} \tag{2.7}$$

Letting $N(\eta) = N(0)$ for the density of states at the surface of the Fermi sea the integration becomes,

$$\frac{1}{V} = \frac{N(0)}{2} \ln\left(\frac{E - 2\hbar\omega_c}{E}\right) \tag{2.8}$$

This gives the energy as,

$$E = -\frac{2\hbar\omega_c}{e^{-2/N(0)V} - 1} \tag{2.9}$$

In the weak limit of $N(0)V \ll 1$, this reduces down to a binding energy of $E \approx -2\hbar\omega_c e^{-2/N(0)V}$. So electrons have a non-zero binding energy in the presence of a finite attractive potential, but it remains to be seen what the origin of the attractive potential is and can this cutoff energy be quantified.

The interaction arises from the electron-lattice coupling. Electrons are repelled by the Coulomb force acting between them, but they are at the same time attracted to the positive nuclei that make up a metal's crystal lattice. The attraction between electrons and this lattice leads to deformations of the physical structure creating pockets of higher positive charge density. This higher positive charge density causes other electrons to group near the region and overcome the Coulomb repulsion to form Cooper pairs. The energy cutoff then has a characteristic value on the scale of the Debye frequency or the maximum frequency of vibrations that the lattice can respond to.

The above derivation showed that the Fermi sea is unstable against the formation of Cooper pairs. The Fermi sea continues to form Cooper pairs until the binding energy of forming another pair becomes zero (due to the shrinking N(0) of the system as pairs form). The many particle ground state wavefunction can be described by macroscopic quantities.

This can be shown by taking the BCS ansatz and finding a collective operator which acts as a degree of freedom over the whole superconducting state.

Consider two groundstates,

$$|\Psi_G\rangle = \prod_{\vec{\mathbf{k}}} \left(u_{\vec{\mathbf{k}}} + v_{\vec{\mathbf{k}}} c^\dagger_{\vec{\mathbf{k}}\uparrow} c^\dagger_{-\vec{\mathbf{k}}\downarrow} \right) |0\rangle \tag{2.10}$$

$$|\Psi^\varphi_G\rangle = \prod_{\vec{\mathbf{k}}} \left(\left|u_{\vec{\mathbf{k}}}\right| + \left|v_{\vec{\mathbf{k}}}\right| e^{i2\varphi} c^\dagger_{\vec{\mathbf{k}}\uparrow} c^\dagger_{-\vec{\mathbf{k}}\downarrow} \right) |0\rangle \tag{2.11}$$

Here $c_{\vec{\mathbf{k}}\sigma}$ and $c^\dagger_{\vec{\mathbf{k}}\sigma}$ represent the annihilation and creation operators for a fermionic system which satisfy anticommutation relations,

$$\{c_{\vec{\mathbf{k}}\sigma}, c^\dagger_{\vec{\mathbf{k}}'\sigma'}\} = \delta_{\vec{\mathbf{k}},\vec{\mathbf{k}}'}\delta_{\sigma,\sigma'} \tag{2.12}$$

$$\{c_{\vec{\mathbf{k}}\sigma}, c_{\vec{\mathbf{k}}'\sigma'}\} = \{c^\dagger_{\vec{\mathbf{k}}\sigma}, c^\dagger_{\vec{\mathbf{k}}'\sigma'}\} = 0 \tag{2.13}$$

and $\left|u_{\vec{\mathbf{k}}}\right|^2 + \left|v_{\vec{\mathbf{k}}}\right|^2 = 1$. In this context $\left|u_{\vec{\mathbf{k}}}\right|^2$ and $\left|v_{\vec{\mathbf{k}}}\right|^2$ represent the probability of finding an unoccupied or occupied Cooper pair with momentum $\hbar\vec{\mathbf{k}}$ respectively. By expanding out equation 2.11 the expressing can be rewritten as,

$$|\Psi^\varphi_G\rangle = \sum_{n=0} |\lambda_{2n}| e^{i2n\varphi} |\psi_{2n}\rangle \tag{2.14}$$

where the ground state is represented as a superposition of numbers states of Cooper pairs and $|\lambda_{2n}|$ is given by,

$$|\lambda_{2n}| = \prod_{\vec{\mathbf{k}}} \left|u_{\vec{\mathbf{k}}}\right| \prod_{\vec{\mathbf{k}}'} \left|v_{\vec{\mathbf{k}}'}\right| \tag{2.15}$$

with $\vec{\mathbf{k}}$ running over unoccupied pairs and $\vec{\mathbf{k}}'$ running over occupied pairs. Projecting out the state $|\psi_{2n}\rangle$ using,

$$2\pi\delta_{nm} = \int_0^{2\pi} d\varphi e^{i(n-m)\varphi} \tag{2.16}$$

the state becomes

$$|\psi_{2n}\rangle = \frac{1}{2\pi|\lambda_{2n}|} \int_0^{2\pi} d\varphi e^{-2in\varphi} |\Psi^\varphi_G\rangle \tag{2.17}$$

This should immediately bring to mind the idea of a coherent state in which it is well characterized by an amplitude and a phase over the entire material. The bulk superconductor can then be represented in terms of these macroscopic variables.

2.2 The Josephson Equations

Developed in 1962, and experimentally observed a year later[2], the Josephson equations[31] describe the flow of a superconducting current across a "weak link" between two independent superconductors known as a junction. The weak link can take many forms the most common is that of a superconductor-insulator-superconductor (SIS) junctions where a superconducting material sandwiches a thin insulating barrier of oxide. There are also superconductor-normal-superconductor (SNS) junctions where a normal metal is placed between the superconducting electrodes and constricted contact junctions (SsS) where the contact is physically weak between electrodes.

The effort of the previous section was to justify that the "wavefunction" of superconducting material can be written macroscopically. When the Cooper pairs condense the superconductor forms a coherent state whose wavefunction can be defined in terms of a charge density and a phase,

$$\Psi(\vec{\mathbf{r}}, t) = \sqrt{n(\vec{\mathbf{r}}, t)} e^{i\varphi(\vec{\mathbf{r}}, t)} \tag{2.18}$$

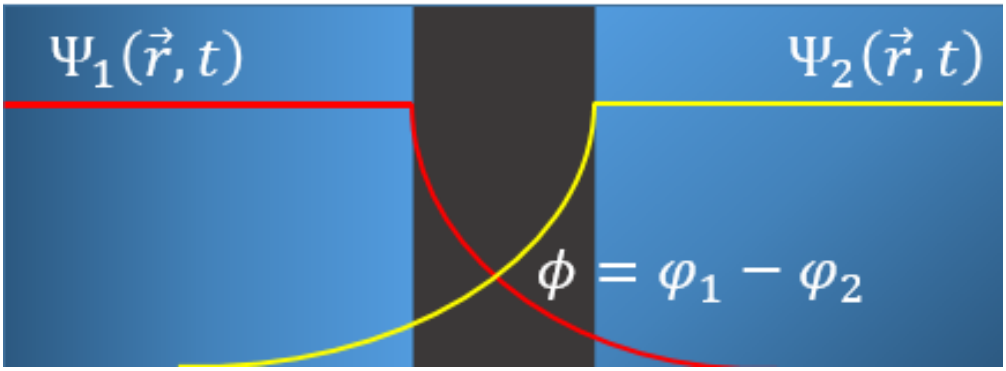

Figure 2.1: Depiction of a weak link between two superconductors. Josephson junctions can take many forms where the barrier is given by some insulating metal, a normal metal, or just a constriction of the metal. This forms a potential barrier between the two islands. Cooper pairs on either side of the island have a nonzero probability of tunnelling across the link. The current and voltage of this circuit element is given by the Josephson equations.

The derivation of the Josephson equations which govern the behaviour of the superconducting weak link follows from the Schrödinger equation by assuming that the insulator forms a constant barrier of height E_J.

Using the ansatz of equation 2.18 above the two sides are written as,

$$\Psi_L(\vec{\mathbf{r}},t) = \sqrt{n_L(\vec{\mathbf{r}},t)}e^{i\varphi_L(\vec{\mathbf{r}},t)} \tag{2.19}$$

$$\Psi_R(\vec{\mathbf{r}},t) = \sqrt{n_R(\vec{\mathbf{r}},t)}e^{i\varphi_R(\vec{\mathbf{r}},t)} \tag{2.20}$$

Applying a voltage V across the two superconductors and under the assumption of a weak potential barrier, the equations of motion become,

$$i\hbar\frac{\partial\Psi_L}{\partial t} = \left(\frac{qV}{2} - \frac{\hbar^2}{2m}\nabla^2\right)\Psi_L + E_J\Psi_R \tag{2.21}$$

$$i\hbar\frac{\partial\Psi_R}{\partial t} = \left(-\frac{qV}{2} - \frac{\hbar^2}{2m}\nabla^2\right)\Psi_R + E_J\Psi_L \tag{2.22}$$

Assuming that the wavefunction is uniformly distributed this can be simplified using $\boldsymbol{\nabla}\Psi = 0$. Using the ansatz on 2.21 gives,

$$i\hbar\left(\frac{1}{2\sqrt{n_L}}e^{i\varphi_L}\frac{\partial n_L}{\partial t} + i\sqrt{n_L}e^{i\varphi_L}\frac{\partial\varphi_L}{\partial t}\right) = \frac{qV}{2}\sqrt{n_L}e^{i\varphi_L} + E_J\sqrt{n_R}e^{i\varphi_R} \tag{2.23}$$

Defining the phase across the barrier as $\phi = \varphi_L - \varphi_R$ and separating the equation into real and imaginary parts gives,

$$\frac{\partial n_L}{\partial t} = \frac{2E_J}{\hbar}\sqrt{n_L n_R}\sin\phi \tag{2.24}$$

$$\frac{\partial\varphi_L}{\partial t} = -\frac{E_J}{\hbar}\sqrt{\frac{n_R}{n_L}}\cos\phi - \frac{qV}{2\hbar} \tag{2.25}$$

Applying the same to the right side of the barrier gives,

$$\frac{\partial n_R}{\partial t} = -\frac{2E_J}{\hbar}\sqrt{n_L n_R}\sin\phi \tag{2.26}$$

$$\frac{\partial\varphi_R}{\partial t} = -\frac{E_J}{\hbar}\sqrt{\frac{n_L}{n_R}}\cos\phi + \frac{qV}{2\hbar} \tag{2.27}$$

The flow of charge from one island to the other imposes the conservation equation $\frac{\partial n_L}{\partial t} =$

$-\frac{\partial n_R}{\partial t}$ which for a single Cooper pair tunnelling across the barrier gives,

$$I = I_C \sin\phi \tag{2.28}$$

$$\frac{\partial \phi}{\partial t} = \frac{qV}{\hbar} \tag{2.29}$$

Where $I_C = \frac{qE_J}{\hbar}$ is the critical current density and $q = 2e$, is the charge of a Cooper pair.

2.3 Circuit Quantization

Superconductivity and the Josephson equations give two important characteristics for designing interesting dynamics on quantum circuits, a low dissipation environment and non-linear dynamics. The first is evident from the low temperature nature of superconductivity. Temperatures below 50mK can be readily achieved in dilution refrigerators limiting the effects of thermal fluctuations and allowing near zero loss of power. The second characteristic of non-linearity of Josephson junctions will be shown to introduce an anharmonicity in quantum circuits allowing for qubit behaviour. This section presents the methods and techniques of circuit quantization with which to build and develop quantum circuits.

2.3.1 Transmon Qubits

Superconducting qubits have enjoyed much success as an implementation of quantum computing. This has been largely due to the the transmon qubit[32]. Superconducting devices are in theory easily scalable, simply controlled, and readily fabricated. The implementation has been able to make great use of the advances across a range of industries from microwave electronics to the silicon wars of modern computing. The transmon qubit is formed by capacitively shunting a Cooper-Pair Box (CPB). A CPB is an electronic circuit formed by taking a superconducting island and coupling it to the ground plane where there is an excess of Cooper pairs. Excess Cooper pairs on the island then form the basis (of charge states) of the implementation.

The shunting of the CPB acts to suppress the charge noise associated with the circuit.The Hamiltonian for the CPB can be derived from the equations of motion given by the Josephson equations 2.28-2.29 and corresponds to the circuit shown in 2.2.

$$H = 4Ec(n - n_g)^2 - E_J(\Phi_{ext})\cos(\varphi) \tag{2.30}$$

The charging energy $E_C = \frac{e^2}{2C_\Sigma}$, of the device can be solved for using the techniques outlined

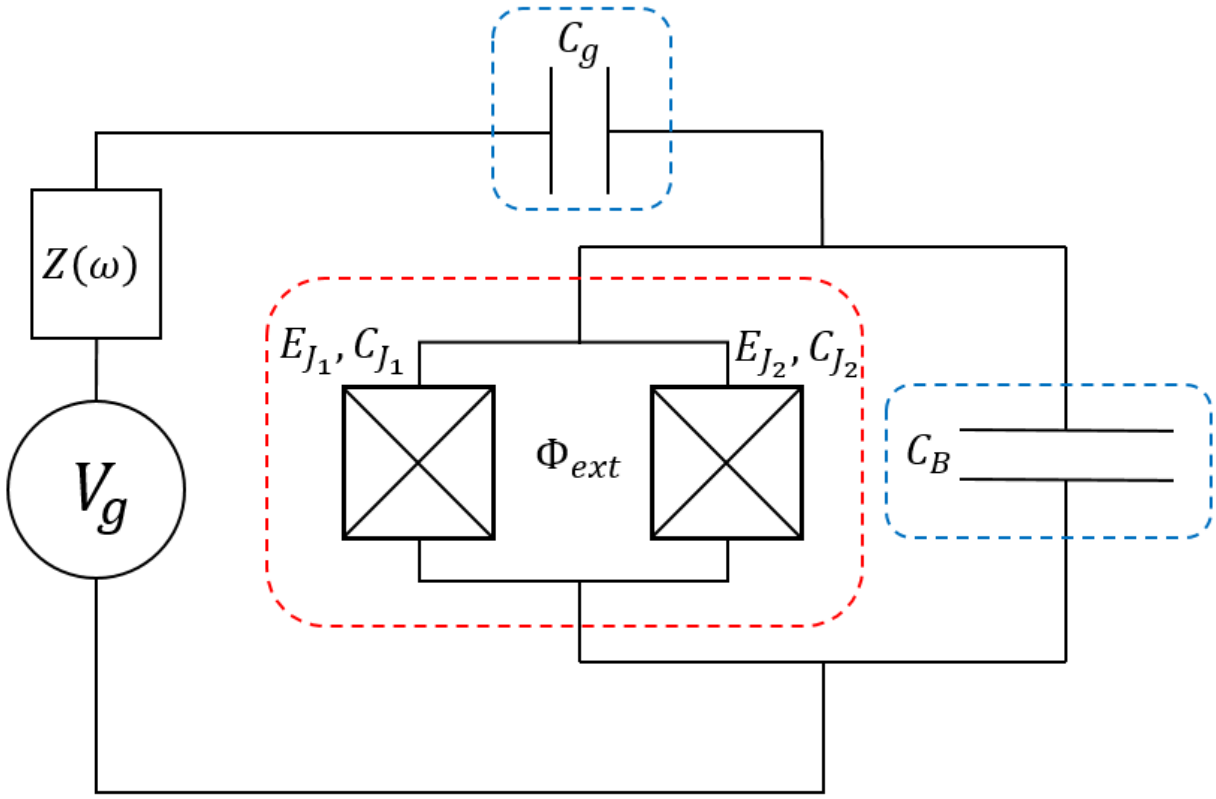

Figure 2.2: Circuit depiction of a transmon qubit. The Hamiltonian can be thought of as arising from interplay between the circuit elements to 'hold' a charge (electrostatic contributions in blue) on either side of the islands. and the ability for a charge to tunnel across the insulating barrier of the Josephson junction (SQUID in red).

in [32, 15] or numerically as outlined in chapter 4. When $E_J \gg E_C$ the operators n and φ can be approximated as harmonic oscillators,

$$\hat{n} = i\sqrt{\frac{1}{2\epsilon}}(\hat{a}^\dagger - \hat{a}) \tag{2.31}$$

$$\hat{\varphi} = \sqrt{\frac{\epsilon}{2}}(\hat{a}^\dagger + \hat{a}) \tag{2.32}$$

where $\epsilon = \sqrt{8E_C/E_J}$. The transmon regime is usually quoted as starting at $E_J/E_C \gtrsim 20$. The effects of the gate charge, n_g is greatly diminished in this regime as the charge dispersion decreases exponentially with the ratio E_J/E_C. The anharmonicity also decreases with the ratio but decreases geometrically. This still gives a well isolated single excitation manifold for defining qubit levels[32]. The spectrum of equation 2.30 is shown in figure 2.3 as a function

of the gate charge for various ratios.

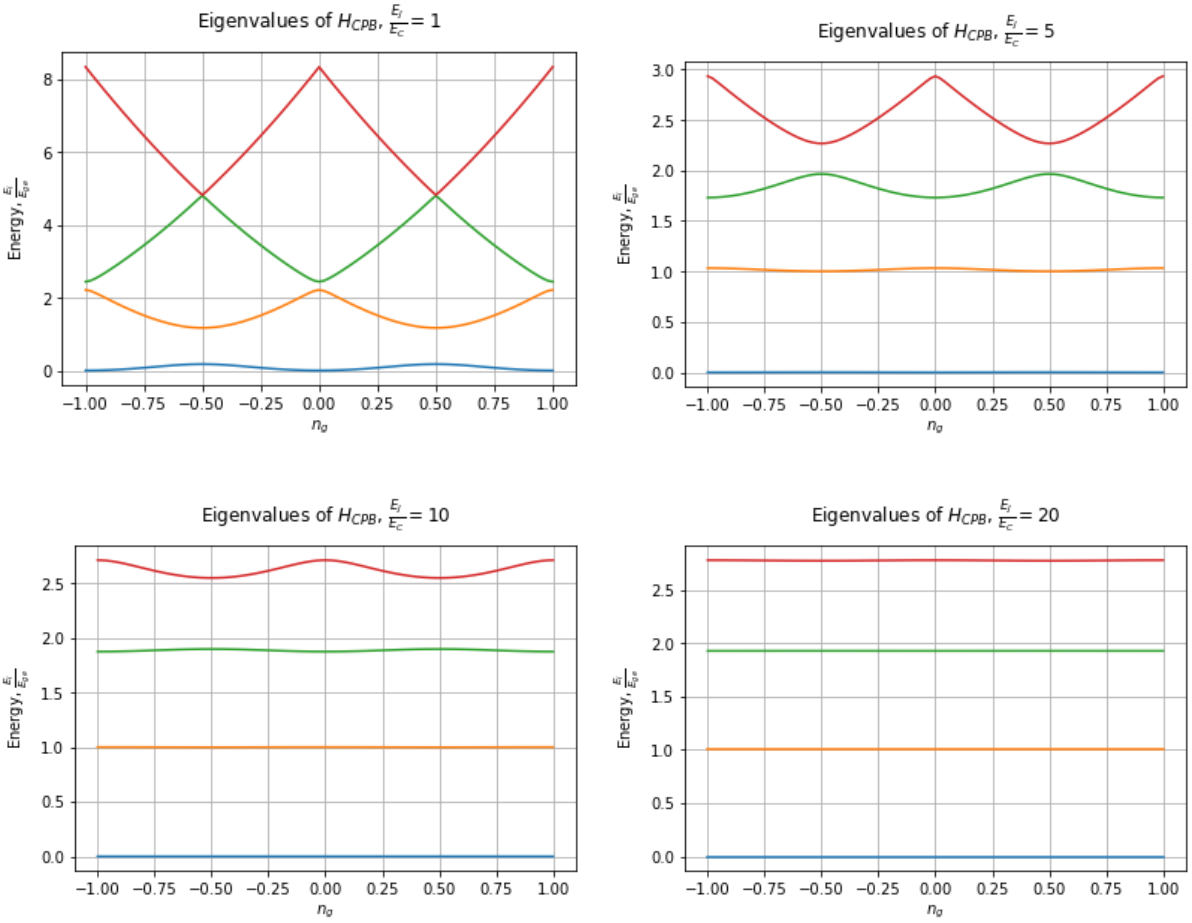

Figure 2.3: Energy spectrum of the Cooper-Pair Box Hamiltonian as a function of the gate charge n_g. As the ratio E_J/E_c increases the sensitivity of the energy levels to variations in n_g decreases exponentially. The charge dispersion is given by $\frac{\partial E_{ij}}{\partial n_g}$. If the device is biased at a point where the curvature changes rapidly any small fluctuation can cause dramatic changes in the energy structure. As E_J/E_C increases this sensitivity to variations smooths out and the levels become flat. In the transmon the well defined quantum observable is the phase rather than the charge.

Under this harmonic approximation the Hamiltonian, Taylor expanded to quartic order, now reads,

$$H = \sqrt{8E_J E_C}\left(\hat{a}^\dagger \hat{a} + \frac{1}{2}\right) - \frac{E_C}{12}\left(\hat{a}^\dagger + \hat{a}\right)^4 \tag{2.33}$$

The anharmonicity is given by $\alpha = E_{12} - E_{01} = -E_C$. Treating the case of a split junction

or SQUID separately[58]. The Hamiltonian for the two junctions is,

$$H_J = E_{J_1}\cos(\varphi_1) + E_{J_2}\cos(\varphi_2) \tag{2.34}$$

These variables can be redefined in terms of a total phase and the difference of phases across the nodes of the SQUID,

$$\varphi = \frac{\varphi_1 + \varphi_2}{2} \tag{2.35}$$

$$\theta = \varphi_1 - \varphi_2 \tag{2.36}$$

The phase difference can be written as the total external magnetic flux passing through the loop, $\theta = \frac{2\pi\Phi_{ext}}{\Phi_0}$, where Φ_0 is the magnetic flux quantum. The Hamiltonian after applying a trigonometric identity and factoring can then be written as,

$$H_J = (E_{J_1} + E_{J_2})\left|\cos\left(\frac{2\pi\Phi_{ext}}{\Phi_0}\right)\right|\sqrt{1 + d^2\tan^2\left(\frac{2\pi\Phi_{ext}}{\Phi_0}\right)}\cos(\varphi) \tag{2.37}$$

The parameter $d = (E_{J_1} - E_{J_2})/(E_{J_1}+E_{J_2})$ is related to the symmetry between the junctions. Variations in the junction symmetry are often small and thus $d \sim 0$. This gives,

$$H_J = E_J(\Phi_{ext})\cos(\varphi) = 2E_J\left|\cos\left(\frac{2\pi\Phi_{ext}}{\Phi_0}\right)\right|\cos(\varphi) \tag{2.38}$$

2.3.2 Transmission Lines and Harmonic Oscillators

Another fundamental element of the superconducting circuit implementation is the transmission line. These elements guide propagating electromagnetic waves from their source allowing various dynamics of our qubits to be probed as well as to protect the qubit against decoherence when formed into a cavity.

Consider a transmission line as in figure 2.4. The line can be broken up into differential elements of lengths dz and represented in terms of lumped elements. The line then has inductance and capacitance per unit length ℓ_0 and c_0. From Kirchhoff's voltage and circuit laws the voltage and current drop across each differential element is,

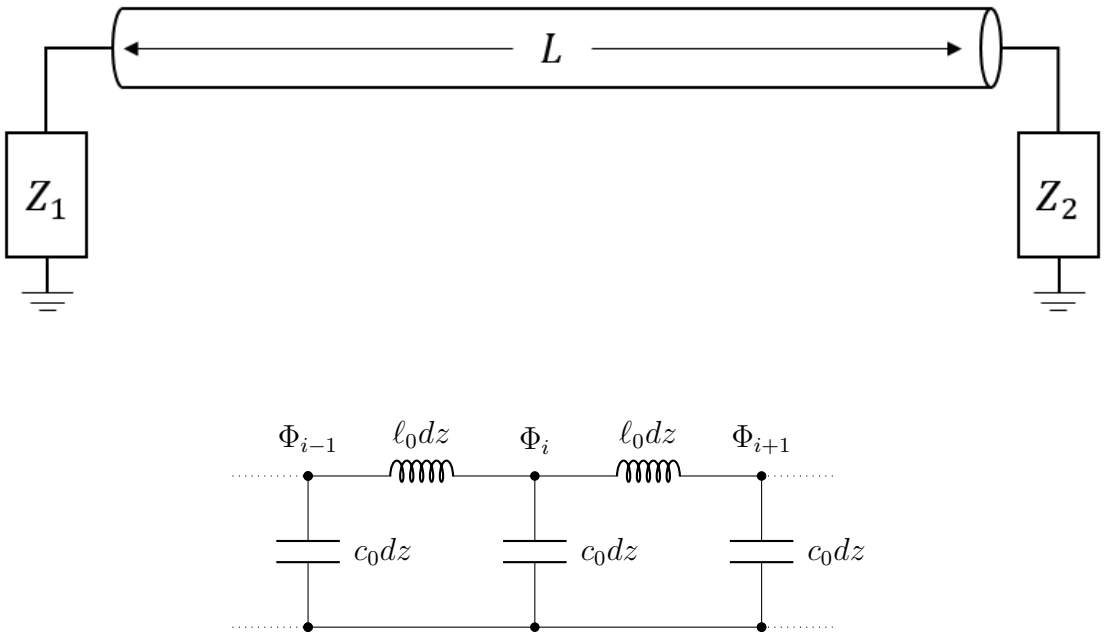

Figure 2.4: Model of a distributed transmission line resonator and broken up into lumped elements. By defining an endpoint to the infinite transmission line and imposing boundary conditions, Z_1, Z_2 at either end, the transmission line supports a standing wave and becomes a resonator or a cavity. A capacitor, or an open, and a short both reflect incoming radiation. A capacitor acts as a mirror forming an anti-node of the electric field where as a short to ground can be thought of as an anchoring point to a rope and forms a node as a boundary condition.

$$V(z + \mathrm{d}z\,, t) = V(z,t) - (\ell_0\,\mathrm{d}z)\frac{\mathrm{d}I(z,t)}{\mathrm{d}t} \tag{2.39}$$

$$I(z + \mathrm{d}z\,, t) = I(z,t) - (c_0\,\mathrm{d}z)\frac{\mathrm{d}V(z,t)}{\mathrm{d}t} \tag{2.40}$$

In this continuum limit ($\mathrm{d}z \to 0$) this becomes,

$$\frac{\partial V}{\partial z} = -\ell_0 \frac{\partial I}{\partial t} \tag{2.41}$$

$$\frac{\partial I}{\partial z} = -c_0 \frac{\partial V}{\partial t} \tag{2.42}$$

This can be solved by taking a separable solution with angular frequency, ω,

$$V(z,t) = \tilde{V}_\omega(z) e^{-i\omega t} \tag{2.43}$$

$$I(z,t) = \tilde{I}_\omega(z) e^{-i\omega t} \tag{2.44}$$

Equations 2.41 and 2.42 then can be decoupled and take the familiar form of the equation of motion for a harmonic oscillator.

$$\frac{\partial^2 \tilde{V}_\omega}{\partial z^2} + \omega^2 l_0 c_0 \tilde{V}_\omega = 0 \tag{2.45}$$

$$\frac{\partial^2 \tilde{I}_\omega}{\partial z^2} + \omega^2 l_0 c_0 \tilde{I}_\omega = 0 \tag{2.46}$$

The solutions to these can be combined with their time dependent component to form two solutions for left and right propagating waves.

$$V(z,t) = \sum_{\omega, s=\pm 1} \tilde{V}^s_\omega(z) e^{i(k_s(\omega)z - \omega t)} + c.c \tag{2.47}$$

$$I(z,t) = \sum_{\omega, s=\pm 1} \frac{\tilde{V}^s_\omega(z)}{sgn(s) Z_0} e^{i(k_s(\omega)z - \omega t)} + c.c \tag{2.48}$$

AC voltages and currents can be written as the sum of these forward and backward propagating waves as well as a superposition of frequency. Here, s, ranges over forward and backward moving waves (+ and -), $k_\pm(\omega) = \pm\omega\sqrt{l_0 c_0}$ is the wavenumber and has dispersion relationship $v = \omega/k(\omega) = 1/\sqrt{l_0 c_0}$ which is the effective speed of light in the transmission line, and $Z_0 = \sqrt{l_0/c_0}$ is the characteristic impedance. Given boundary conditions imposed by Z_1 and Z_2, the voltage forms a standing wave in the transmission line and $k_n(\omega) = (2\pi n/L)\beta$, where β is a factor imposed by the boundary conditions, for a typical half-wave or quarter-wave resonator β is equal to $1/2$ and $1/4$ respectively. Here, $n \in \mathbb{Z}$, runs over negative and positive integers and will take the place in the notation for s.

The energy contained within the field is,

$$E = \int_{\frac{L}{2}}^{\frac{L}{2}} dz \frac{1}{2} c_0 V(z)^2 + \frac{1}{2} l_0 I(z)^2 \tag{2.49}$$

where the time dependence can be pulled out via the time averaging theorem[72]. Expanding this and integrating gives,

$$E = 2c_0 L \sum_n V_n {V_n}^* \tag{2.50}$$

This can be rewritten more familiarly as,

$$H = \sum_n \left(\frac{1}{2} p_n^2 + \frac{1}{2} \omega_n^2 q_n^2 \right) \tag{2.51}$$

by defining the dynamical quantities,

$$q_n = \frac{4c_0 L}{\omega_n^2} (V_n + {V_n}^*) \tag{2.52}$$

$$p_n = (-i\omega_n) \left(\frac{4c_0 L}{\omega_n^2} \right) (V_n - {V_n}^*) \tag{2.53}$$

By promoting these dynamical quantities to operators and imposing the canonical commutation relationship $[\hat{q}_n, \hat{p}_n] = i\hbar$ the usual canonical quantization follow.

$$\hat{a}_n = \frac{1}{2} (\omega_n \hat{q}_n + i\hat{p}_n) \tag{2.54}$$

$$\hat{a}_n^\dagger = \frac{1}{2} (\omega_n \hat{q}_n - i\hat{p}_n) \tag{2.55}$$

This allows us to write the Hamiltonian as that of a harmonic oscillator of discrete modes of frequency, $f_n = vn\beta/L$.

$$H = \sum_n \hbar\omega_n \left(\hat{a}_n^\dagger \hat{a}_n + \frac{1}{2} \right) \tag{2.56}$$

2.3.3 Jaynes-Cummings Model

The discussion of mirrors in the previous section was no coincidence. When combining the circuit elements together the transmon and the transmission line resonator act as an atom inside of a cavity. The field of cavity QED has been well studied[29, 14, 67] and describes the interaction of a light field and the electric dipole of an atom. In circuit QED strong couplings are granted relatively for free as the electric field of the cavity has very high mode confinement in the case of planar cavities or because electrical elements can be made "large" in the case of 3D cavities. The regime of ultra-strong coupling has also recently been achieved allowing for new atomic dynamics to be studied within the context of circuit QED[22].

To see how these electrical devices couple it is useful to refer back to the original Hamiltonian of the CPB (eq 2.30). The electrical circuit of the coupled system is shown in figure 2.5. The qubit couples to all modes of the cavity individually, but the model of the cavity

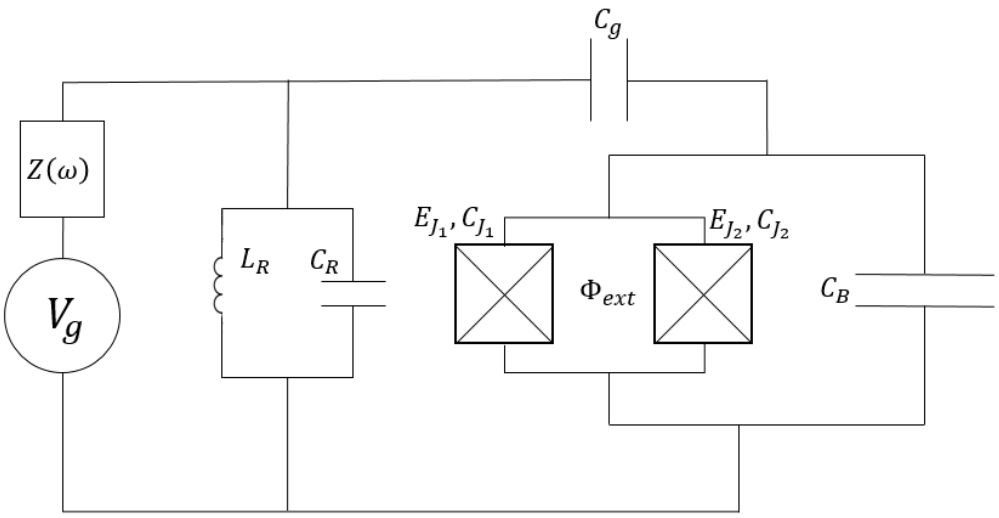

Figure 2.5: Circuit depiction of a resonant cavity and a transmon qubit.

can be reduced to that of a single LC-oscillator as it is often the case that we are working with the fundamental mode. In the CPB Hamiltonian the gate charge, n_g, can be written as $V_g C_g/e$ which is the number of charges corresponding to an applied voltage from the source. V_g can then be written as,

$$V_g = V_{DC} + V_{AC} \tag{2.57}$$

V_g is then the sum of some classical DC voltage and some AC voltage. This AC voltage can be quantized in terms of the cavity modes,

$$V_{AC} = \sum_n \sqrt{\frac{\hbar\omega_n}{c_0 L}}(a_n^\dagger + a_n) \tag{2.58}$$

For just the fundamental mode of the cavity this reduces to a single voltage. Expanding the first term of the CPB Hamiltonian now gives,

$$H = 4E_C(n - n_g)^2 - \frac{4E_C C_g}{e} V n + H_{offset} \tag{2.59}$$

Using this the coupling can now be rewritten as,

$$g(z) = 2\frac{C_g}{C_\Sigma} eV(z) = 2\frac{C_g}{C_\Sigma} eV_0 \cos\left(k(\omega_r)z\right) \tag{2.60}$$

where $V_0 = \sqrt{\frac{\hbar\omega_r}{c_0 L}}$, and $k(\omega_0)$ is defined in the previous subsection. The interaction is then,

$$H_{cav-qb} = g\sigma_x\big(a^\dagger + a\big) \tag{2.61}$$

In the regime where $g/\omega_r \ll 1$ the rotating wave approximation can be applied due to the fast counter-rotating terms averaging out. This results in the Jaynes-Cummings model of the dipole of an atom coupled to the electric field.

$$H = \omega_r a^\dagger a + \omega_q \sigma^+\sigma^- + g\big(\sigma^+ a + \sigma^- a^\dagger\big) \tag{2.62}$$

It useful now to move into the interacting frame to approximately diagonalize the Hamiltonian via the unitary transformation,

$$U = e^{\frac{g}{\Delta}\left(\sigma^+ a - \sigma^- a^\dagger\right)} \tag{2.63}$$

and truncating at $\mathcal{O}\Big(\big(\frac{g}{\Delta}\big)^2\Big)$ where $\Delta = |\omega_r - \omega_q| > g$ is the detuning of the qubit and the cavity. The Hamiltonian in this dispersive frame is,

$$H_{disp} = \omega_q\sigma^+\sigma^- + \left(\omega_r + \frac{g^2}{\Delta}\sigma^+\sigma^-\right)a^\dagger a \tag{2.64}$$

Here the state of the qubit introduces a shift into the frequency of the cavity which can be use to non-destructively infer the state of the qubit[10].

Chapter 3

Quantum Simulation of Gauge Theories

As stated in the epigraph of the introduction a long standing goal of quantum computing has been to simulate and emulate the physics of other quantum systems. Lattice gauge theories (LGTs) in particular pose issues for classical computation. The "sign problem" of Monte-Carlo algorithms for fermions is known to be a thorn in the side of many computational physicists[66]. When trying to calculate the expectation of some observable classically you need to calculate the partition function. However to do so you need to sum over the probabilities of all configurations of the system. For a bosonic system this is fine, but as soon as you introduce the antisymmetry of fermions this involves sampling over negative probabilities (or more accurately negative weights). To solve this one could consider diagonalizing the Hamiltonian, but finding a decomposition is an exponentially hard problem. Often times one has to restrict their models to "sign-problem free" systems, quasi one dimensional systems, or use various approximation methods such as mean field theory which limit their regime of applicability. One solution to this is to accept defeat and deal with the exponential growth of simulating quantum physics by build ever larger supercomputers that are up to the computational task, or in lieu of that find a completely different method of which quantum computers seem to be up to the task.

3.1 Quantum Simulation

There are two major types of quantum simulation that researchers tend to work with. These are digital and analog simulators. Digital simulations try to break down and decom-

pose the time evolution of a Hamiltonian to be simulated into a universal set of gates that can be implemented on any universal quantum computer. There has been some success[46, 50] with these implementations as of late, but a fully fault tolerant system would need to embed error correction into the simulation algorithm to reduce the problems introduced by noisy gates. Analog simulation however acts as an intermediate step toward a fully universal system. The idea is to map directly from the Hamiltonian to be simulated onto the system which simulates, which in turn also has its own issues, but provides some interesting insight into physical problems which are achievable on a few qubit system. This section gives a brief overview of the two paradigms and their advantages/disadvantages.

3.1.1 Digital Quantum Simulation (DQS)

Suppose we have some Hamiltonian we want to study given by H_{sys} and some state $|\phi(0)\rangle$ which evolves in time under the action of this Hamiltonian,

$$|\phi(t)\rangle = U(t)\,|\phi(0)\rangle = e^{-i\hbar H_{sys}t}\,|\phi(0)\rangle \tag{3.1}$$

In principle implementing the physical Hamiltonian may not be readily achievable on our particular hardware. The goal then is to decompose this unitary into a set of universal gates and time step the problem by successive applications of these gates. By using a universal set of gates it stands to reason that digital quantum simulation is also universal and thus can simulate any Hamiltonian[39]. Universality is not the same though as efficiency. Not all unitary operators have an efficient decomposition into a universal gate set[24]. The following gives an outline of the ideas behind DQS.

Suppose the system Hamiltonian can be broken down into the sum of local terms,

$$H_{sys} = \sum_i H_i \tag{3.2}$$

In general it is not the case that $[H_i, H_{i'}] = 0$. Due to this the unitary $U(t)$ cannot be broken down simply as $U(t) = \prod_i e^{i\hbar H_i t}$. Instead this unitary is broken up into time steps of size Δt,

$$U(t) = \left(\exp\left(-i\hbar H\Delta t\right)\right)^{t/\Delta t} = \left(\exp\left(-i\hbar \sum_i H_i \Delta t\right)\right)^{t/\Delta t} = U(\Delta t)^{t/\Delta t} \tag{3.3}$$

By using the Baker-Campbell-Hausdorff expansion this $U(\Delta t)$ gives,

$$U(\Delta t) \approx \prod_i \exp\left(-i\hbar H_i \Delta t\right) + \mathcal{O}\left(\Delta t^2\right) \tag{3.4}$$

This expression can then be decomposed into local gates such as in the Trotter-Suzuki expansion[63]. While this method is perhaps not the most efficient and has several other issues[13] there exist higher order methods than this first order Trotter formula which are more efficient and precise. Also since the digital quantum simulation process uses universal gate sets this implementation can be embedded within quantum error correction schemes to better preserve the evolution of the system at each iteration. Figure 3.1 illustrates the DQS process.

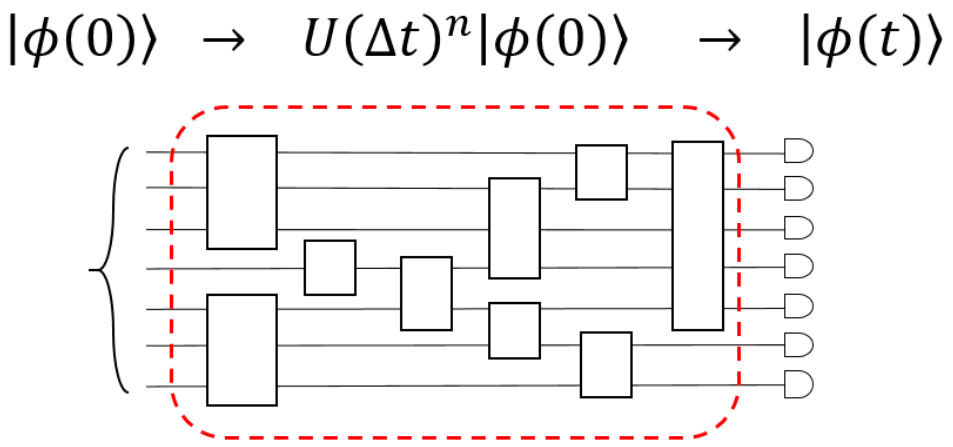

Figure 3.1: Digital quantum simulation involves three steps. The first is initialization. A state $|\phi(0)\rangle$ that represents the initial state of a physical system under study needs to be prepared or initialized with high fidelity. The Trotterized unitary is then applied iteratively to evolve the initial state to a final state $|\phi(t)\rangle$. This final state is then read out and an observable of interest can be computed from this information.

3.1.2 Analog Quantum Simulation

In analog quantum simulation (AQS) one looks for a physical system for which the Hamiltonian can be designed or engineered to behave as a Hamiltonian of interest. The process can be summarized as looking for an operator f such that a state in the system to be emulated, $|\psi\rangle$, maps to a state that can be controllably implemented, $|\phi\rangle$, via a

transformation $\mathcal{U}|\psi\rangle = |\phi\rangle$ and maps the Hamiltonian of the system of interest via $H_{sim} = \mathcal{U}H_{sys}\mathcal{U}$[62]. Physics tends to often be counter-intuitively simple in that many problems of interest tend to be local. This means that many microscopic properties result in larger scale emergent phenomena and parameters become compressed[57, 42, 65]. One may be interested in studying phenomenological effects such as phase transitions[25, 17], dynamical behaviour[11], or like the name sake a direct analogy between the system to be emulated and the emulator[35]. Also, because the emulator and the emulated are assumed to be similar, to a certain degree state preparation is given for free as the natural evolution of an initially prepared state will tend toward the equilibrium of the problem as time evolves the system.

There are drawbacks for analog quantum simulation that should be noted. Chiefly among these is that these simulations are not universal meaning that care and attention needs to be made in designing these systems. Variations in physical parameters need to be accounted for when translating from model to reality. However as techniques in fabrication improve and reduce the variability of designs AQS offers a near term solution to achieving the long standing goals of quantum computing especially when fully fault-tolerant architectures that can implement this physics is a long term goal.

3.2 Lattice Gauge Theories

Gauge theories underpin almost all of modern physics. The standard model is built upon the $SU(3) \times SU(2) \times U(1)$ non-abelian symmetry group and unifies the electromagnetic, weak, and strong force[53]. The abstractness of gauge theories are difficult to manage, but can be somewhat encapsulated by making the statement that physics shouldn not change depending on whether it is looked at from the right or the left. A gauge then fixes the direction we are looking and any local change that occurs in the system leaves the overall structure unchanged.

These symmetries can be broken down into two categories, global and local symmetries. A global symmetry is something that applies to the system as a whole and does not depend on the space-time position of the system. A local symmetry depends explicitly on where the system is within space-time.

The easiest example of a local symmetry is to think about the flow of a general flux. In the absence of charge accumulation a flux that enters any point must exit that point.

As an example consider traffic in New York on a day with no accidents. Any traffic that enters an intersection must leave that intersection (a sort of Gauss' law). A local

transformation then corresponds to the lights of the intersection changing. The direction of traffic may change, but the flow of traffic through the intersection does not accumulate. In this case the traffic acts as our current that flows with each car being a charge and the mediating gauge field is the traffic light (the stoplight-ion is our gauge boson). This is Noether's theorem in action where any continuous symmetry implies a conserved current and the generator of the symmetry is the conserved charge. Quantum electrodynamics is the more notable example of this which is a manifestation of a U(1) symmetry.

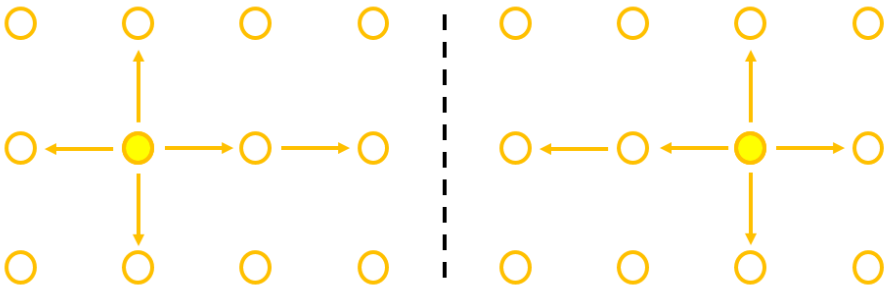

Figure 3.2: We are trying to capture a discretized version of Gauss' law in our quantum simulator. This version in one dimension is given by, $\hat{E}_{i,i+1} - \hat{E}_{i-1,i} = \psi_i^\dagger \psi_i$. $\hat{E}_{i,i+1}$ corresponds to the electric field between lattice sites i and $i+1$. On each lattice site exists a fermionic field operator ψ_i. If an excitation wants to hop through the lattice then the electric field must reciprocate that change so as to enforce Gauss' law.

The successes of perturbative approaches *à* la Feynmann are useful and give a full description of high energy QED, but break down when applied to other problems. Consider the coupling constant of quantum chromodynamics. The constant is inversely proportional to the square of the momentum of the system. Then at high energies a perturbative approach works fine and explains asymptotic freedom for which the Nobel Prize was award to David Gross, Frank Wilczek, and David Politzer in 2004[27, 54]. However at low energies the coupling becomes greater than unity and the usual perturbative approaches break down.

Lattice gauge theories (LGTs) were originally developed in the mid seventies by Kenneth Wilson to deal with just this issue[70]. The method involves performing a Wick rotation to translate from a Minkowski space to a Euclidean space then discretizing the spatial components into a discrete lattice. The work set off a chain of developments not only in the realms of QCD, but across many areas of physics where a non-perturbative approach is valid. One such example with wide ranging applications is the modelling of phase transitions in high temperature superconducting cuprates[52].

3.2.1 A Short Primer on LGTs

Following from the Kogut-Susskind formulation of lattice gauge theories[33] consider a lattice where the degrees of freedom occupy the links and massive particles occupy the vertices. A simple example of a Hamiltonian where one particle hops from one site to another site on a 1D lattice is given by,

$$H = \sum_i \psi_i^\dagger \psi_i - \sum_i \left(\psi_i^\dagger \psi_{i+1} + h.c \right) \tag{3.5}$$

A global symmetry is given via the transformation $\psi_i \to \psi_i^{'} = V(\phi)^\dagger \psi_i V(\phi)$ where,

$$V(\phi) = e^{-i\phi \sum_j \psi_j^\dagger \psi_j} \tag{3.6}$$

Here the action of the U(1) global symmetry, $V(\phi)$, introduces a global phase on any local site, $\psi_i^{'} = e^{-i\phi}\psi_i$, which is independent of the position. The generator of this symmetry, $G = \sum_i G_i = \sum_i \psi_i^\dagger \psi_i$, commutes with the Hamiltonian, $[H, G] = 0$, and so the underlying dynamics are left unchanged by the transformation.

This global transformation, $V(\phi)$, is then promoted to a local invariance, $V(\phi_i)$, via a transformation of the form,

$$\psi_i \to \psi_i^{'} = e^{i \sum_j \phi_j G_j} \psi_i e^{-i \sum_j \phi_j G_j} = e^{-i\phi_i} \psi_i \tag{3.7}$$

The Hamiltonian under this transformation is no longer invariant as the hopping term acquires a phase, $e^{i(\phi_i - \phi_{i+1})}$. A link variable needs to be introduced such that the Hamiltonian remains invariant under a local transformation. That is a variable, $U_{i,i+1}$ needs to be introduced between adjacent sites that transforms as,

$$U_{i,i+1} \to U_{i,i+1}^{'} = e^{i \sum_j \phi_j G_j} U_{i,i+1} e^{-i \sum_j \phi_j G_j} = e^{-i\phi_i} U_{i,i+1} e^{i\phi_{i+1}} \tag{3.8}$$

The new locally invariant Hamiltonian is then,

$$\tilde{H} = \sum_i \psi_i^\dagger \psi_i + \sum_i \left(\psi_i^\dagger U_{i,i+1} \psi_{i+1} + h.c \right) \tag{3.9}$$

As well there is a locally conserved quantity, $[H, G_i] = 0$. There are two major types of gauge fields static and dynamical. The differences are summarized below in figure 3.3.

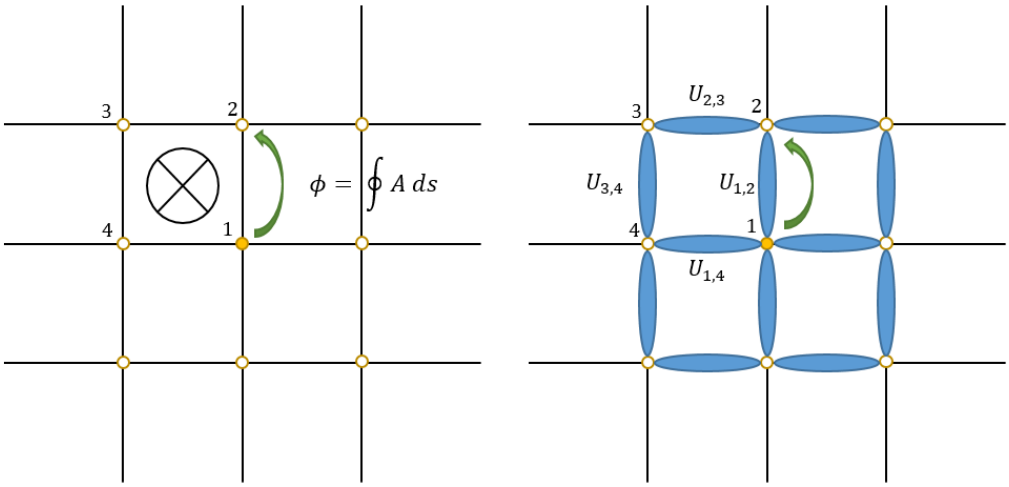

Figure 3.3: (Left) A static gauge field acts like a Aharonov-Bohm phase. There is no physical field that has it's own dynamics associated with the accumulation of the phase as it moves through the lattice. (Right) A dynamical gauge field is one where there is a physical field moderating the exchange between vertices of the lattice. These fields give rise to exchange particles and contain their own energy and dynamics. There is a reciprocal effect acting on the field as a particle moves from lattice site to lattice site.

3.2.2 The Schwinger Model

The Schwinger model[59] was originally developed to explain that gauge invariant fields can indeed give rise to massive particles. The model describes a U(1) symmetry in 1+1 dimensions (one spatial, one time). The model can be drawn upon to understand concepts such as QED, which itself is a U(1) gauge theory. Although a toy model it is one of the simplest descriptions of lattice gauge theories that exhibit non-trivial phenomena such as spontaneous symmetry breaking and confinement of particles (i.e. the fermions cannot exist independently). This makes the Schwinger model a useful benchmark of a quantum simulator.

Following the Hamiltonian formulation the massive Schwinger Hamiltonian takes the form[4],

$$H = m\sum_k (-1)^k \psi_k^\dagger \psi_k + \sum_k \left(\tilde{E}_{k,k+1}\right)^2 + \lambda \sum_k \left(\psi_k^\dagger e^{i\tilde{A}_k}\psi_{k+1} + \text{h.c}\right) \tag{3.10}$$

The electric field and the corresponding vector potential, A, commute as, $[\tilde{E}_{k,k+1}, \tilde{A}_j] = \frac{i}{a}\delta_{k,j}$ where a is the lattice spacing.

Here there are massive fermionic matter sites, an electric field, and the hopping term

between adjacent sites. The electric field and vector potential form a continuum of states, but this can be simplified by mapping the electric field to a discrete space of angular momentum states, $S^z_{k,k+1}$, and the vector field to a phase denoted θ_k. The commutator is then given by $[S^z_{k,k+1}, \theta_j] = i\delta_{k,j}$. $S^\dagger_{k,k+1} = S^x_{k,k+1} + iS^y_{k,k+1} = e^{i\theta_k}$ then acts as a ladder operator on the basis given by $S^z_{k,k+1}$. The Hamiltonian is now,

$$H = m\sum_k (-1)^k \psi^\dagger_k \psi_k + g\sum_k \left(S^z_{k,k+1}\right)^2 - J\sum_k \left(\psi^\dagger_k S^\dagger_{k,k+1}\psi_{k+1} + \text{h.c}\right) \tag{3.11}$$

This forms a quantum link representation of a lattice gauge theory[69]. This discretized spin structure still encapsulates the U(1) gauge symmetry of QED via the transformation,

$$V = \prod_k e^{i\alpha_k G_k} \tag{3.12}$$

where G_k is given by, $G_k = S^z_{k-1,k} - S^z_{k,k+1} + \psi^\dagger_k\psi_k + \frac{1}{2}\left[(-1)^k - 1\right]$. G_k is a conservered quantity $[G_k, H] = 0$ and so eigenstates of the Hamiltonian, $|\psi\rangle$ are also eigenstates of G_i and those that additionally satisfy $G_k|\psi\rangle = 0$ represent physical states that obey Gauss' law. This is summarized in figure 3.4.

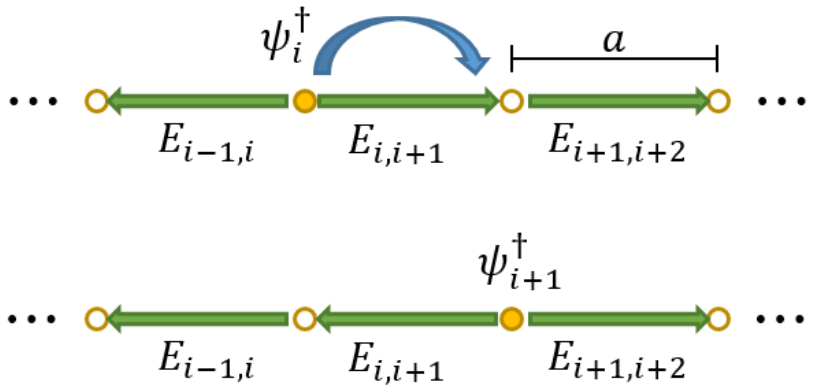

Figure 3.4: A hopping of a fermion in the Schwinger model causes the field to reciprocate this change and flip its direction. This gauge invariant behaviour captures the physics of Gauss's law, $\boldsymbol{\nabla} \cdot E - \rho = 0$ (in the limit of the lattice spacing, $a \to 0$), where the flux leaving a lattice site is propotional to the charge contained within it.

The QLM formalism is powerful in that with it abelian and non-abelian gauge theories can be represented[69] and more complicated models can be studied in the context of quantum simulation.

The quantum link formulation is increadibly useful, but a bit hard to implement phys-

ically. Thankfully this can be achieved via two other transformations which preserve the gauge-invariant behaviour. These are the Schwinger representation[56] and the Jordan-Wigner transformation[30] (for one dimensional systems).

The Schwinger representation is given by,

$$S^{\dagger} = ab^{\dagger} \tag{3.13}$$

$$S^{z} = \frac{1}{2}\left(b^{\dagger}b - a^{\dagger}a\right) \tag{3.14}$$

This transformation encodes the spin state into two harmonic oscillators with total spin $S = \frac{1}{2}(a^{\dagger}a + b^{\dagger}b)$ and existing in the $N = 2S$ energy manifold.

The Schwinger representation can be used to implement a mapping of both bosons and fermions, however it requires two oscillators for every component of the lattice. This resource allocation can be alleviated slightly with the Jordan-Wigner transformation,

$$\psi_i = e^{-i\pi \sum_{j<i} \left(\sigma_j^z + 1\right)/2} \sigma_i^- \tag{3.15}$$

For a lattice of k fermionic matter sites and $k-1$ fields the mapping requires $k + 2(k-1)$ elements. This mapping also takes advantage of the natural anti-commutation of the Pauli operators as $\{\sigma_i^-, \sigma_j^+\} = \delta_{ij}$. The fermionic matter sites now are mapped onto a two-level system,

$$\psi_i^{\dagger}\psi_i = \frac{1}{2}(\sigma_i^z + 1) \tag{3.16}$$

The final form of the Schwinger Hamiltonian to be emulated by the superconducting system is then,

$$H_{sch} = \frac{m}{2}\sum_i (-1)^i \sigma_i^z + \frac{g}{4}\sum_i \left(b_{i+1}^{\dagger}b_{i+1} - a_i^{\dagger}a_i\right)^2 - J\sum_i \left(\sigma_i^+ a_i b_{i+1}^{\dagger}\sigma_{i+1}^- + \text{h.c}\right) \tag{3.17}$$

3.3 Superconducting Implementation

A full superconducting implementation has been outlined by our theory collaborators and the calculations here are reproduced from their work for the sake of completeness[44]. A unit cell of the Schwinger circuit consists of two matter qubits and two linking anharmonic

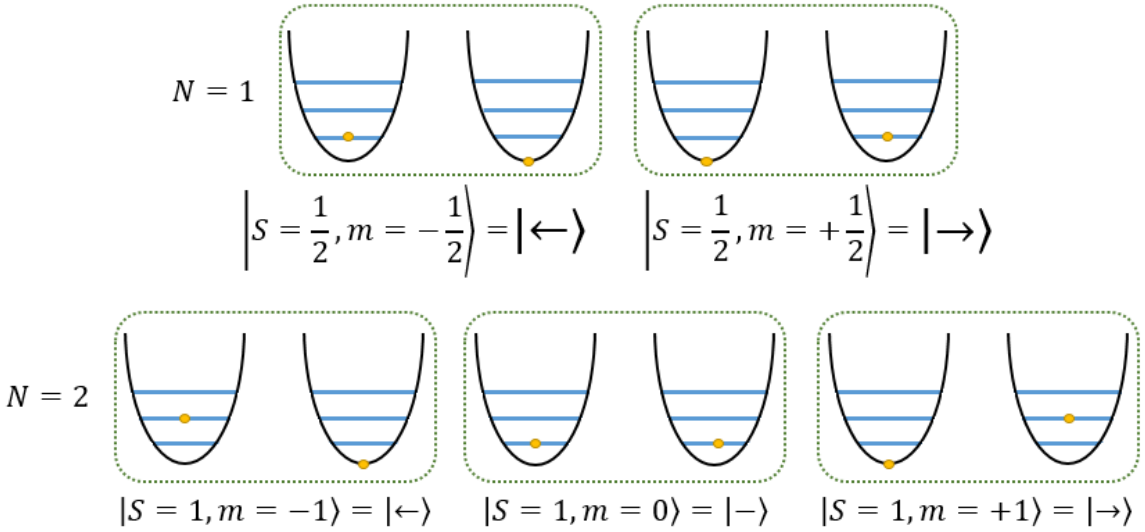

Figure 3.5: Effects of the Schwinger representation mapping a continuous field onto the discrete angular momentum states of the quantum link model. Each excitation manifold in this mapping corresponds to a different total angular momentum and spin moments allowing for the dynamics of different spins to be studied. For the single excitation manifold the field can only point toward or away from each lattice vertex. This gives an approximation to QED when a fermion on the lattice site hops and the field has to reciprocate. The spin-1 manifold allows from interesting dynamics of confinement to be observed due to the presence of a "vacuum" field state. This corresponds to no interaction of the link on the matter sites and studying the phase transition from string to vacuum gives an indication of spontaneous symmetry breaking in a large lattice chain.

oscillators coupled through a junction. These can be formed by capacitively shunting a junction in different regimes. For qubits the transmon regime consists of shunting a junction with a capacitance such that the ratios of junction energy to charging energy are $E_J/E_C \sim 20 - 60$. For the anharmonic oscillators this requires shunting the junction with a larger capacitance than a qubit to take advantage of the transmon's higher levels. The circuit for the implementation of shown below in figure 3.6.

The Hamiltonian for this circuit is explored in more detail in Chapter 4, but is stated here. The matter sites form transmon qubits with Hamiltonian,

$$H_{qb} = \omega_1 \sigma_1^z + \omega_2 \sigma_2^z \tag{3.18}$$

where $\omega_i = \sqrt{8E_{C_i}E_J(\Phi^i_{ext})} - E_{C_i}$.

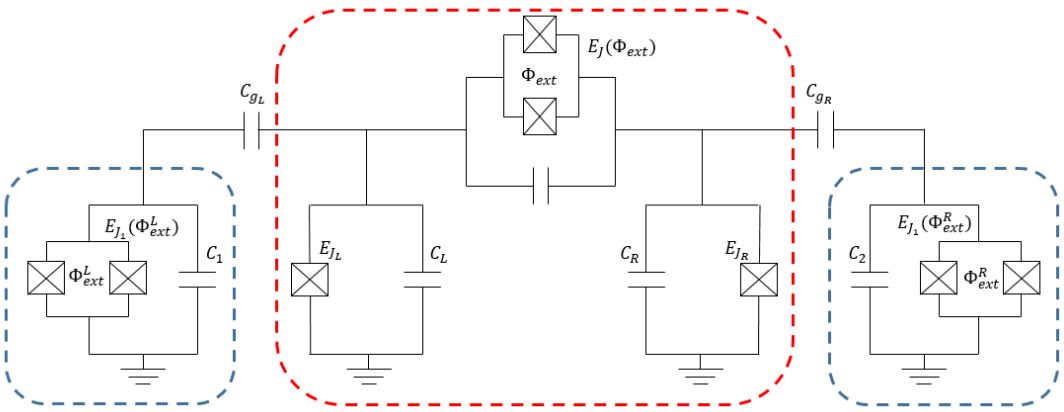

Figure 3.6: Single iterate of the superconducting circuit implementation of the Schwinger model. The red box corresponds to the non-linear link or the fields of a gauge theory whereas the blue boxes correspond to the massive fermionic matter sites. The 1D model can be extended by adding on more of these blocks to the circuit. Moving to the correct parameter space can be achieved by setting a static background field with a coil and tuning the qubits locally with an on-chip DC line. Readout can be achieved by coupling dispersively to cavity resonators (not pictured).

The non-linear link that forms the spin states of the field gives contribution,

$$\begin{aligned} H_{link} = &\frac{1}{2}\mathbf{Q}\mathcal{C}^{-1}\mathbf{Q}^{\mathbf{T}} + \frac{1}{2}\mathbf{\Phi}\mathbb{L}\mathbf{\Phi}^{\mathbf{T}} - E_{J_L}\cos\left(\frac{\phi_L}{\phi_0}\right) - \frac{E_{J_L}}{2}\left(\frac{\phi_L}{\phi_0}\right)^2 \\ &- E_{J_R}\cos\left(\frac{\phi_R}{\phi_0}\right) - \frac{E_{J_R}}{2}\left(\frac{\phi_R}{\phi_0}\right)^2 - E_J(\Phi_{ext})\cos\left(\frac{\phi_R - \phi_L}{\phi_0}\right) \\ &- \frac{E_J(\Phi_{ext})}{2}\left(\frac{\phi_R - \phi_L}{\phi_0}\right)^2 \end{aligned} \tag{3.19}$$

The first two terms in the Hamiltonian corresponds to all the cross capacitances and inductances in the circuit where $\mathbf{Q} = (Q_L, Q_R)$, $\mathbf{\Phi} = \left(\frac{\phi_L}{\phi_0}, \frac{\phi_R}{\phi_0}\right)$ and the capacitance and inductance matrices, $\mathcal{C}, \mathbb{L}$, are given by,

$$\mathcal{C} = \begin{bmatrix} C_L + C_J & -C_J \\ -C_J & C_R + C_J \end{bmatrix} \qquad \mathbb{L} = \begin{bmatrix} E_{J_L} + E_J & -E_J \\ -E_J & E_{J_R} + E_J \end{bmatrix}$$

The operators ϕ_i/ϕ_0 and Q_i can be approximated as harmonic oscillators as per the first chapter. Engineering this parameter space is explored in the next chapter.

The last component of the Hamiltonian gives the coupling between the matter sites and

their adjacent links,

$$H_{qb-link} = \lambda\big(\sigma_1^+ a_L + \sigma_2^+ a_R + \text{h.c}\big) \tag{3.20}$$

Moving to a rotating frame with respect to,

$$H_{rot} = (\omega_1 + \Delta)\Big(\sigma_1^+\sigma_1^- + a_L^\dagger a_L\Big) + (\omega_2 - \Delta)\Big(\sigma_2^+\sigma_2^- + a_R^\dagger a_R\Big) \tag{3.21}$$

where Δ is the detuning from the adjacent link site, moves to a frame where the overall frequency scale of the qubits is removed. The corresponding Hamiltonian is then,

$$\tilde{H} = \frac{\Delta}{2}\sum_i (-1)^i \sigma_i^z + \frac{g}{4}\sum_i \Big(a_i^\dagger a_i - b_{i+1}^\dagger b_{i+1}\Big)^2 + \delta\sum_i \Big(a_i^\dagger a_i + b_{i+1}^\dagger b_{i+1}\Big) \tag{3.22}$$

$$- W\sum_i \Big(a_i^\dagger a_i + b_{i+1}^\dagger b_{i+1}\Big)^2 + \lambda\sum_i \sigma_i^+(a_i + b_i) + \text{h.c} \tag{3.23}$$

Up to second order perturbation with respect to λ then gives the effective Hamiltonian for an entire network matching that of equation 3.17 (identifying the detuning Δ as equivalent to the mass) with some correction terms that need to be energetically supressed by enforcing a hierarchy of energy scales.

Chapter 4

Circuit Design

4.1 Circuit Parameter Space

The parameter space of the design needs to be carefully engineered to exhibit a few key properties. Namely the non-linearities of the link need to be engineered such that first order cross-coupling which leads to gauge variant dynamics is suppressed. This decoupling of the modes also allows for simple excitation of elements within the circuit network. The first thing to show is that the terms in the Hamiltonian obey the hierarchy of energy scales to implement the gauge invariant dynamics.

Starting from the link Hamiltonian of equation 3.19 it is useful to break the Hamiltonian down into left and right modes[55]. Defining the variables,

$$\frac{Q_i}{2e} = \frac{i}{\sqrt{2\epsilon_i}}\left(a_i^\dagger - a_i\right) \tag{4.1}$$

$$\frac{\phi_i}{\phi_0} = \sqrt{\frac{\epsilon_i}{2}}\left(a_i^\dagger + a_i\right) \tag{4.2}$$

$$\epsilon_i = (2e)\sqrt{\frac{C_J + C_{\neg i}}{(\det(\mathcal{C}))(E_J + E_{J_{\neg i}})}} \tag{4.3}$$

and using these the local harmonic components for each side of the link become,

$$H_i = \frac{1}{2}\frac{C_J + C_{\neg i}}{\det(\mathcal{C})}Q_i^2 + \frac{1}{2}(E_J + E_{J_i})\left(\frac{\phi_i}{\phi_0}\right)^2 = (E_J + E_{J_i})\epsilon_i a_i^\dagger a_i \tag{4.4}$$

The mixing of the harmonic Hamiltonian modes (off-diagonal elements of the capacitance

and inductance matrices) is given by,

$$H_{LR} = \frac{C_J}{\det(\mathcal{C})} Q_L Q_R - E_J \frac{\phi_L \phi_R}{\phi_0^2} \tag{4.5}$$

$$= \frac{C_J}{2\sqrt{\epsilon_L \epsilon_R}\,\det(\mathcal{C})} \left(a_L^\dagger a_R - a_L^\dagger a_R^\dagger + h.c. \right) - \frac{E_J \sqrt{\epsilon_L \epsilon_R}}{2} \left(a_L^\dagger a_R + a_L^\dagger a_R^\dagger + h.c. \right) \tag{4.6}$$

To minimize mixing of the modes and localize to the Hamiltonian into these "left" and "right" modes there are two conditions to be satisfied. First is that the harmonic oscillators of H_L and H_R need to be detuned from one another so that the modes can be discriminated between. This gives the condition,

$$(E_J + E_{J_L})\epsilon_L - (E_J + E_{J_R})\epsilon_R \neq 0 \tag{4.7}$$

It is also required that the first order hopping terms of H_{LR} cancel so that the the modes are constrained to higher order processes. This gives the second condition,

$$E_J \epsilon_L \epsilon_R = \frac{C_J (2e)^2}{\det(\mathcal{C})} \tag{4.8}$$

or equivalently,

$$\left(\frac{E_{J_L}}{E_J} + 1 \right) \left(\frac{E_{J_R}}{E_J} + 1 \right) - \left(\frac{C_L}{C_J} + 1 \right) \left(\frac{C_R}{C_J} + 1 \right) = 0 \tag{4.9}$$

I have taken these conditions and plotted them below in figure 4.1 to map out the space in which the link must be designed to satisfy the mode decoupling constraints.

The terms corresponding to processes $a_L^\dagger a_R^\dagger$ correspond to processes which do not contribute to the dynamics at second order perturbation. The remaining components of the linking Hamiltonian,

$$\begin{aligned} H_1 = &- E_J \cos\left(\frac{\phi_R - \phi_L}{\phi_0} \right) - \frac{E_J}{2} \left(\frac{\phi_R - \phi_L}{\phi_0} \right)^2 - E_{J_L} \cos\left(\frac{\phi_L}{\phi_0} \right) - \frac{E_{J_L}}{2} \left(\frac{\phi_L}{\phi_0} \right)^2 \\ &- E_{J_R} \cos\left(\frac{\phi_R}{\phi_0} \right) - E_{J_R} \left(\frac{\phi_R}{\phi_0} \right)^2 \end{aligned} \tag{4.10}$$

can be treated as usual for the transmon qubit. The cosines are expanded as,

$$\cos\left(\frac{\phi_i}{\phi_0} \right) = \cos\left(\sqrt{\frac{\epsilon_i}{2}} \left(a_i^\dagger + a_i \right) \right) = e^{-\epsilon_i/4} \sum_{n,m;n+m=even}^{\infty} \frac{\left(-\frac{\epsilon_i}{2} \right)^{\frac{n+m}{2}}}{n!m!} \left(a_i^\dagger \right)^n a_i^m \tag{4.11}$$

Keeping only number conserving terms and no counter-rotating terms (as they will not contribute to the dynamics at second order perturbation) the interaction Hamiltonian to the lowest non-trivial order becomes,

$$\begin{aligned} H_{int} \approx & -\frac{e^{-\epsilon_L/4}E_{J_L}\epsilon_L^2}{16}\left(a_L^\dagger\right)^2 a_L^2 - \frac{e^{-\epsilon_R}E_{J_R}\epsilon_R^2}{16}\left(a_R^\dagger\right)^2 a_R^2 \\ & - \frac{e^{-\sqrt{\epsilon_L\epsilon_R}/4}E_J}{16}\left(\epsilon_L^2\left(a_L^\dagger\right)^2 a_L^2 + \epsilon_R^2\left(a_R^\dagger\right)^2 a_R^2 + 4\epsilon_L\epsilon_R a_L^\dagger a_L a_R^\dagger a_R\right) \end{aligned} \tag{4.12}$$

The eigenenergies for the total link Hamiltonian as a function of the external flux is given in figure 4.2 below. The total link Hamiltonian can then be written as,

$$H_{link} = \omega_L a^\dagger a + \omega_R b^\dagger b - \Omega_L\left(a^\dagger a\right)^2 - \Omega_R\left(b^\dagger b\right)^2 - \Omega_{LR} a^\dagger a b^\dagger b + H_{gv} \tag{4.13}$$

where a_L, a_R are redefined as a, b respectively to match the definitions of the previous chapter. H_{gv} correspond to gauge variant terms which preserve total excitation number, but take the dynamics out of the fixed excitation manifold, $\frac{\zeta_i}{2}a_i^\dagger\left(a_L^\dagger a_R + a_L a_R^\dagger\right)a_i$. Moving into the Schwinger representation,

$$|n_1, n_2\rangle = |N = n_1 + n_2, m = (n_1 - n_2)/2\rangle \tag{4.14}$$

The total Hamiltonian including the matter sites is,

$$\sum_{i=1,2}\omega_i^q \sigma_i^+\sigma_i^- + \sum_N \left(\omega_N + \omega_N^z S^z\right)\otimes|N\rangle\langle N| + g(S^z)^2 + H_\lambda + H_{gv} \tag{4.15}$$

The following parameters have been defined as per the supplementary material of [44],

$$W = \frac{1}{4}(\Omega_L + \Omega_R + \Omega_{LR}) \tag{4.16}$$

$$2g = \Omega_{LR} - \Omega_L - \Omega_R \tag{4.17}$$

$$\omega_N = \left(\frac{\omega_L + \omega_R}{2}\right)N - WN^2 \tag{4.18}$$

$$\omega_N^z = \omega_L - \omega_R - (\Omega_L - \Omega_R)N \tag{4.19}$$

The non-excitation preserving components of the expansion of equation 4.10 at second order perturbation lead to a redefinition of the nonlinearity of g[44]. However from the

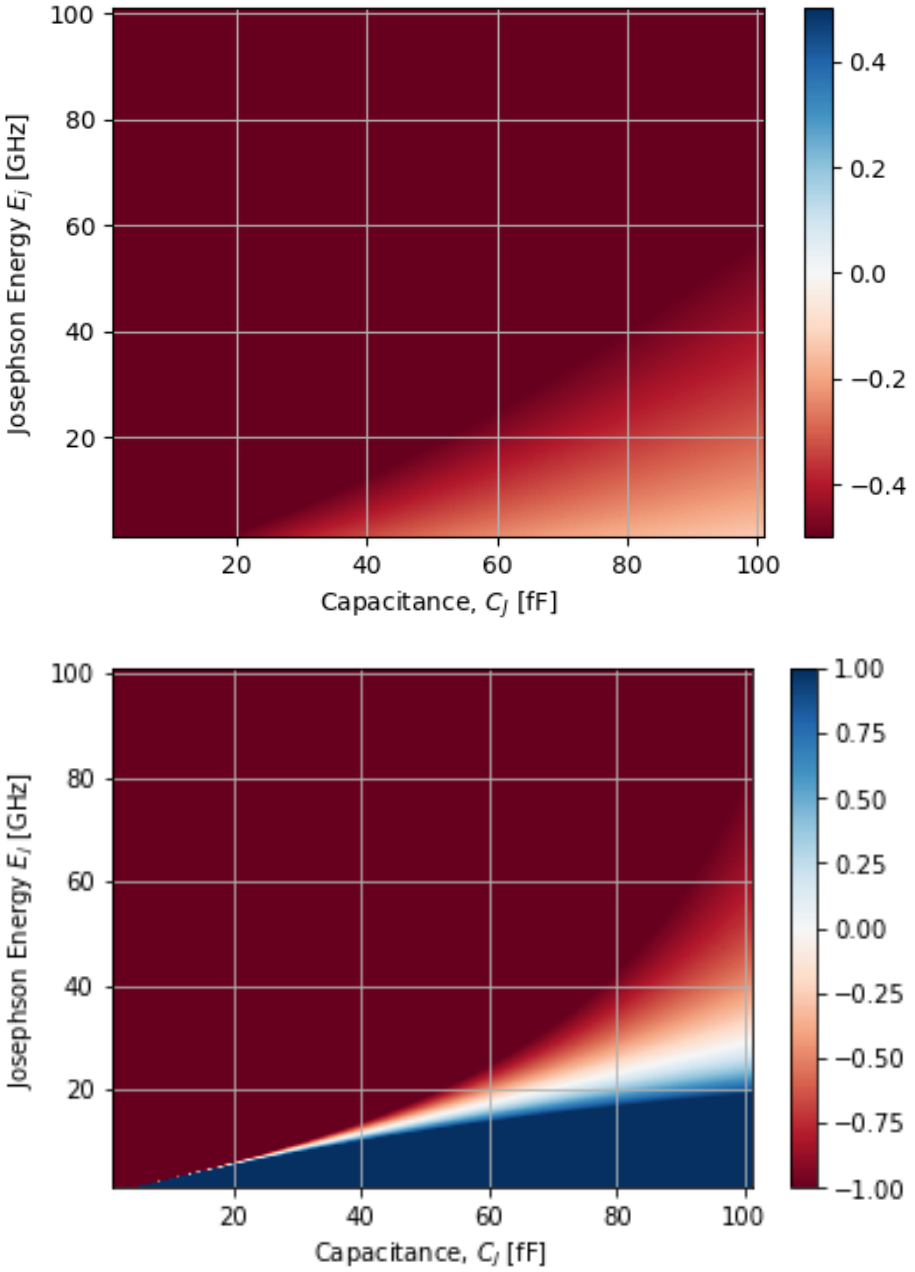

Figure 4.1: (Top) The off-resonance condition has places where the condition is satisfied and outside of typical linewidths to avoid concerns of accidental excitation. The more limiting condition is the second where there is a narrow band of validity (white band in second image). In principle this constraint can be designed around.(Bottom) By setting the coupling capacitance to, for example, 40 fF and fabricating a coupling SQUID of $\sim$ 20 GHz, the device can be tuned via an external biasing field to satisfy the second condition. Variations in the coupling junction were swept to find places where both conditions were met. The parameters for these images were $E_{J_L} = 17$ GHz, $E_{J_R} = 16$ GHz, $C_L = 65$ fF ($E_{C_L} \approx 0.3$ GHz) and $C_R = 48.8$ fF ($E_{C_R} \approx 0.4$ GHz).

defined parameters there is an imposed scale,

$$\omega_N > |\omega_N^z| \gg |\omega_N - \omega_{N\pm1}| \tag{4.20}$$

This makes it energetically unfavourable for a direct flip of the spin on the link. ω_N is the energy corresponding to the fixed energy manifold, ω_N^z is then the energy between spin states within the manifold.

The model breaks down when the energy of transitions within the fixed manifold becomes less energetically favourable than to move to a higher or lower total excitation manifold. I have shown the breakdown of the separation of the higher modes in figure 4.2.

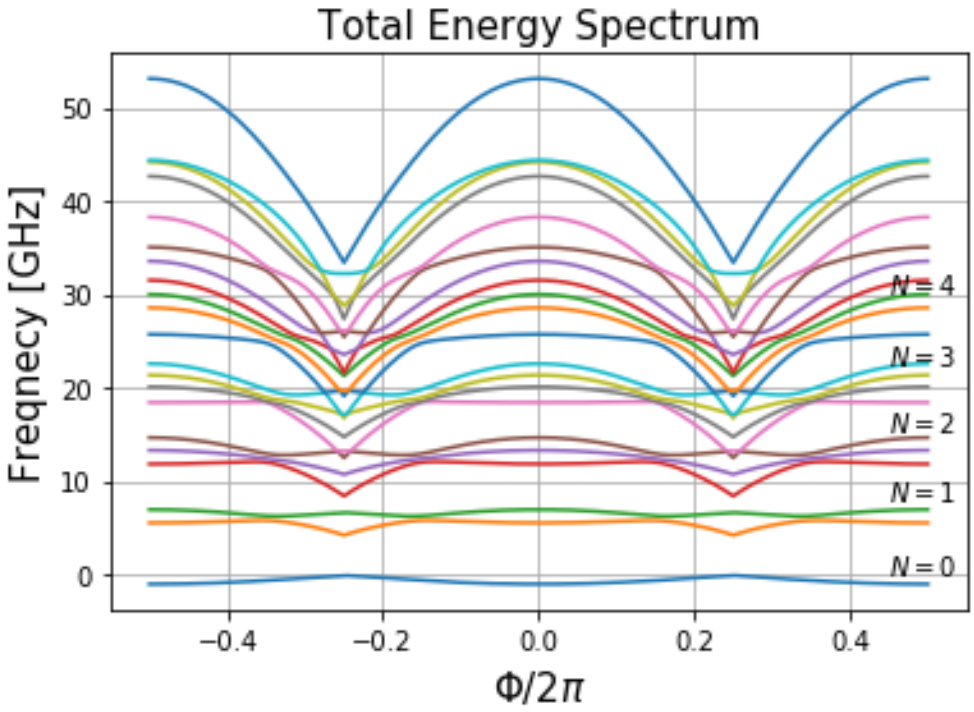

Figure 4.2: The total energy spectrum of the linking Hamiltonian as a function of the external flux Φ_{ext} through a coupling SQUID. The $N = 0, 1, 2, 3, 4$ manifolds are all well separated in energy at positions $\Phi/2\pi \sim -0.151, -0.35$ and their positive counter parts. These correspond to the positions where the inter-modal coupling is minimized as we will see in the next section. The model begins breaking down as N moves upwards to the fifth manifold and the fifth begins to separate at the decoupling position and is no longer well bunched. Using the same parameters as for the above coupling conditions the energy scales in GHz are, $\omega_L = 7.14$, $\omega_R = 7.63$ $\Omega_L \sim 0.10$, $\Omega_R \sim 0.12$, $\Omega_{LR} \sim 0.19$, $W \sim 0.1$, $g = 0.04$ at the decoupling point.

4.1.1 Mode Decoupling

Using the same parameters of the above design the inter-modal coupling of the left and right qubits will change as a function of the external flux. By numerically diagonalizing the Hamiltonian in equation 3.19 the eigenstates can be found and the positions where the states become nearly decoupled can be extracted. Shown below in figure 4.3 are the occupation probabilities of the various levels written in terms of the bare excitation levels. In all eigenstates of the Hamiltonian there are positions in flux where the left and right modes decouple from one another and the eigenbasis becomes the number states of two harmonic oscillators. This decoupling occurs when,

$$2\cos(\Phi_{ext}) = \frac{E_{J_L} + E_{J_R}}{E_J}\frac{C_J^2}{\det(\mathcal{C})} \pm \sqrt{\left(\frac{E_{J_L} + E_{J_R}}{E_J}\right)^2\left(\frac{C_J^2}{\det(\mathcal{C})}\right)^2 - 4\frac{E_{J_L}E_{J_R}}{E_J^2}\frac{C_J^2}{\det(\mathcal{C})}} \quad (4.21)$$

At these points the first order hopping between modes of the two oscillators is suppressed which plays a larger role in the correlated dynamics of the four qubit system. This serves a secondary purpose of helping the addressability of the qubits. The decoupled states are far more easily driven into excitations than the coupled states when applying a driving field.

4.2 Cavity Resonators

Resonant cavities are a critical component in cQED. Cavities act as both the way of measuring with quantum devices through dispersive readout and a way of protecting the device from noise and dissipation.

In this section the co-planar waveguide (CPW) resonator will be introduced. The geometry has two significant features that make it attractive. The first feature is that the architecture has a simple fabrication process which can be defined using optical lithography. The second is that the CPW confines the electromagnetic field along a single direction which allows for strong coupling to qubits.

4.2.1 Resonator Design

For a CPW transmission line to be effective the line needs to be impedance matched to the external environment. Microwave components are typically matched to 50Ω. The characteristic impedance of the line can be solved analytically using a series of conformal

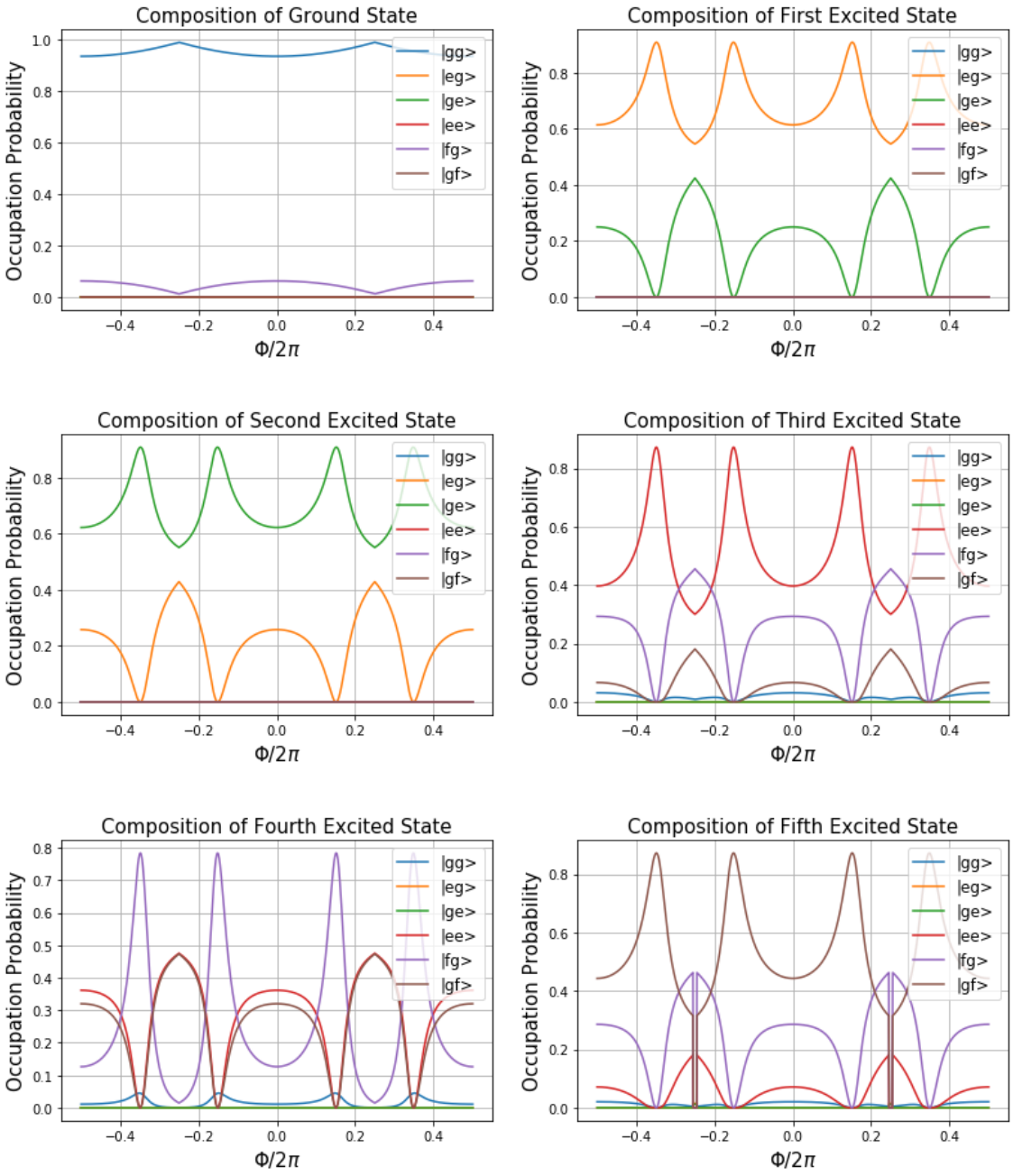

Figure 4.3: Compositions of the zero, one, and two total excitation manifold of the link and their corresponding eigenstates. States are labelled according to ground, first, and second individual excitation levels (g,e,f) for the left and right link elements. The decoupling occurs at positions $\Phi/2\pi \sim -0.15$ and ~ -0.35 as well as their positive counterparts. At this decoupling point the mixing of modes is well suppressed. This allows for single addressability of the transitions from $0 \rightarrow 1$ when driving the circuit element. These calculations were performed by directly diagonalizing and projecting out the components of each eigenstate while sweeping the external bias field on the coupling link.

transformations [61]. This gives,

$$Z_0 = \frac{30\pi}{\sqrt{\epsilon_{eff}}} \frac{K(k_0')}{K(k_0)} \tag{4.22}$$

where $\epsilon_{eff} = (\epsilon_1 + \epsilon_2)/2$ is the effective dielectric constant, $k_0 = S/(S + 2W)$ is the ratio of the center trace width to the total width (see figure 4.4) of the CPW, and $k_0^{'} = \sqrt{1 - k_1^2}$ is given by,

$$k_1 = \frac{\sinh(\pi S/4h)}{\sinh(\pi(S + 2W)/4h)} \tag{4.23}$$

For a CPW with only one substrate $\epsilon_1 = \epsilon_{vac} = 1$. The geometry of the problem is shown in Figure (picture of CPW). With a geometry that matches the external environment the resonance frequency can now be designed for. From the wavenumber of a cavity in the second chapter the fundamental frequency of a CPW can be calculated from,

$$f_0 = \frac{v\beta}{L} = \frac{c\beta}{L\sqrt{\epsilon_{eff}}} \tag{4.24}$$

where again β is either 1/2 or 1/4 depending on whether the CPW is a half-wave or quarter-wave resontator.

The final important factor for the cavity is the quality factor or Q-factor. The Q-factor is defined as the ratio of the energy stored in the cavity compared to the energy lost, and is broken up into two components the internal and external quality factor.

$$\frac{1}{Q_{tot}} = \frac{1}{Q_{int}} + \frac{1}{Q_{ext}} \tag{4.25}$$

The external Q corresponds to the design of the coupling capacitance whereas the internal Q is related to intrinsic losses due to factors such as fabrication process, material dependencies, and defects. The Q-factor is essentially a measure of how well a cavity can hold onto photons and how easily it can preserve a quantum state. It is the case that internal losses should dominate over external losses ($Q_{int} > Q_{ext}$) so that the resonator is over-coupled. This means that the loss of a photon is into an environment that we can readout (the transmission line) and not lost to defects in the device which cannot be accounted for.

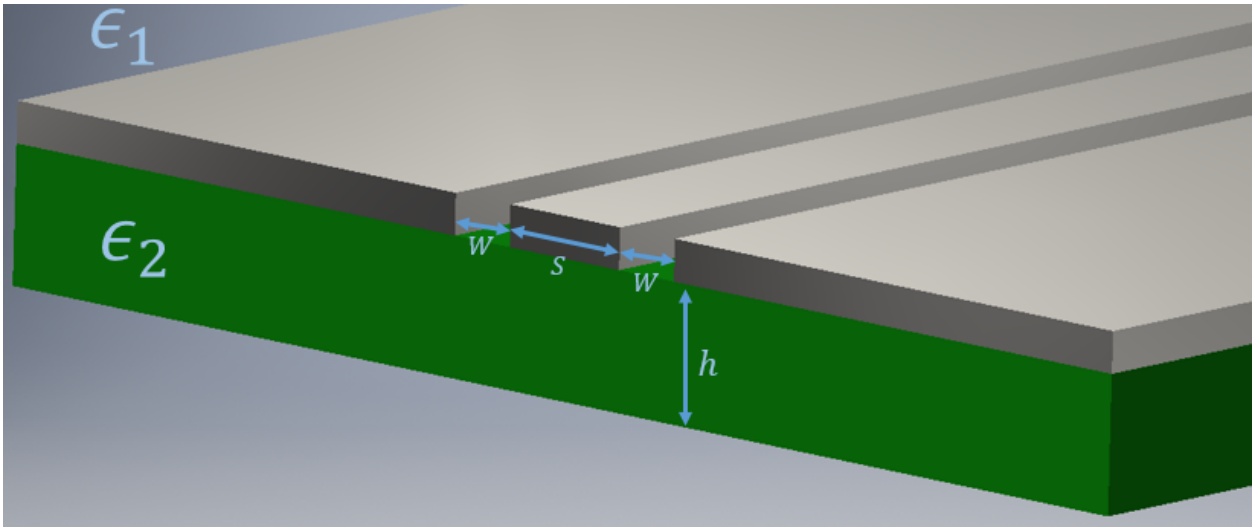

Figure 4.4: Geometry of a coplanar waveguide. A metalized layer is deposited ontop of a substrate. The two ground planes on either side of the center conductor confine the propagating electric field into a very small mode volume so as to maximize coupling between other microwave elements.

4.3 Qubit Design

4.3.1 Junction Parameters

The critical current for a Josephson junction can be derived from BCS theory and are described by the Ambegaokar-Baratoff relation[1],

$$I_c R_n = \frac{2\pi\Delta(0)}{4e} \tag{4.26}$$

Here I_c is the critical current, R_n is the normal state resistance, $\Delta(0)$ is the superconducting gap for the material at absolute zero. For qubit design it is important to keep in mind film thickness to better account for variations across multiple devices. For thin films the superconducting gap can vary between $150 - 200\mu V$[20] and can dramatically affect the consistency of the fabrication process.

Extracting the R_n allows a calculation of the critical current and more importantly the critical current density which can be used to make more consistent future designs. Using double angle shadow evaporation[19] the junction overlap is given by the geometry of figure 4.5 and the overlapping junction area is,

$$A = W([r - t\cos(\theta_1)][\tan(\theta_1) + \tan(\theta_2)] - b + t) \tag{4.27}$$

Here W is the width of the overlap of the smaller metallic trace. The Josephson Energy

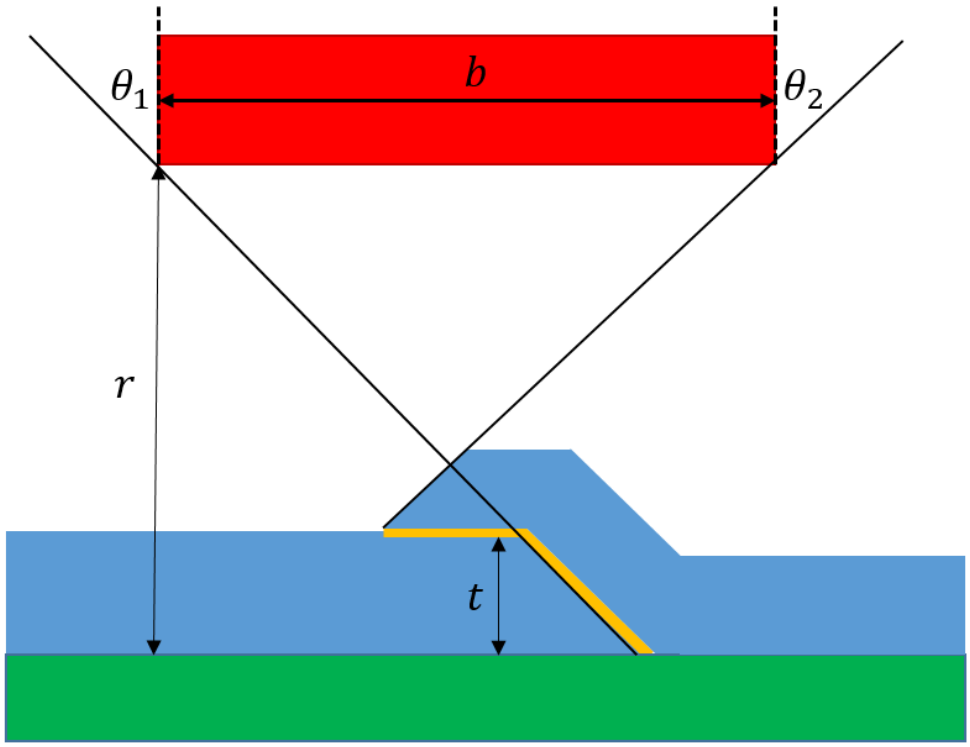

Figure 4.5: r is the thickness of the first layer of photoresist when using a bi-layer process, t is the thickness of the first deposited trace, θ_1 and θ_2 are the two deposition angles, and b is the width of the photoresist bridge.

of the junction can then be calculated from the relation in Section 2.2 and is given by, $E_J = R_Q\Delta/2R_n$ where $R_Q = h/4e^2$ is the resistance quantum.

4.3.2 Qubit Capacitances

The reduced circuit of figure 2.2 does not accurately encapsulate the entire capacitance network. There are more geometric effects which contribute to the effective charging energy of the device. The effective charging energy is given by,

$$C_\Sigma = C_g + C_S \tag{4.28}$$

The variables C_g and C_S are the gate capacitances and the shunt capacitances respectively. To find these capacitances we use *ANSYS Q3D Extractor* to solve for the capacitance matrix

via a finite element solver. The gate capacitance is extracted via a transient simulation of the RC circuit shown in 4.6. The RC constant that is extracted from the simulation gives a good estimate of C_g. The shunt capacitance is then $C_S = C_{AB} + C_J$, where C_{AB} is the inter-digitated capacitance shown below. Typical junction capacitances are on the order of $1 - 10$ fF.

Comparing this against a measured device shows this is a consistent method of estimating the total charging energy. In [23] we found an effective capacitance of 136 fF for the device. Using this method of extracting capacitances gave $C_{23} \sim 100$ fF for our device and $C_g \sim 15$ fF. This would give an estimated effective capacitance of ~ 125 fF which is within 10% of the measured value of $C_\Sigma = 136$ fF.

4.4 First Generation Devices

The first generation devices were fabricated using the recipe outline in Appendix B. First the high resistivity silicon ($\rho \sim 10k\Omega$cm) was first cleaned using a Piranha etch to remove any organic residues from the surface of the wafer. The Piranha cleaning oxidizes the surface of the silicon which is removed by dip cleaning the wafer with hydrogen flouride (HF). Optical lithography is then used in combination with a vapour deposition process to pattern large features on the device (features $> 2\mu$m). Optical alignment markers are first patterned in palladium then large scale aluminum structures such as the webbed ground plane and the cavities are patterned on the chip. Small scale structures such as the interdigitated qubit capacitors and junctions are patterned using electron-beam lithography. Finally these structures are generated using a double angle shadow evaporation technique outlined above to create the Josephson junctions.

The junctions were fabricated assuming a critical current density of $\sim 0.8 - 0.9\mu A/\mu m^2$. This value was estimated across several devices fabricated previously at Syracuse University under the same deposition conditions. The Josephson junctions of the link were were designed for an E_J of approximately 12-14 GHz ($I_c \sim 25 - 30$nA), but the measured normal resistance of the test junctions corresponded to approximately 11GHz. The original design did not include a tunable SQUID coupling between link sites. The link sites themselves formed using SQUIDs which increases the difficulty of finding a correct decoupling point.

The matter sites were coupled to a $\lambda/4$ cavity via a capacitive coupling where as the link sites were coupled with a short island. The characteristic length of the island is designed to be far smaller than the wavelength of the cavity so that it can be approximated as a

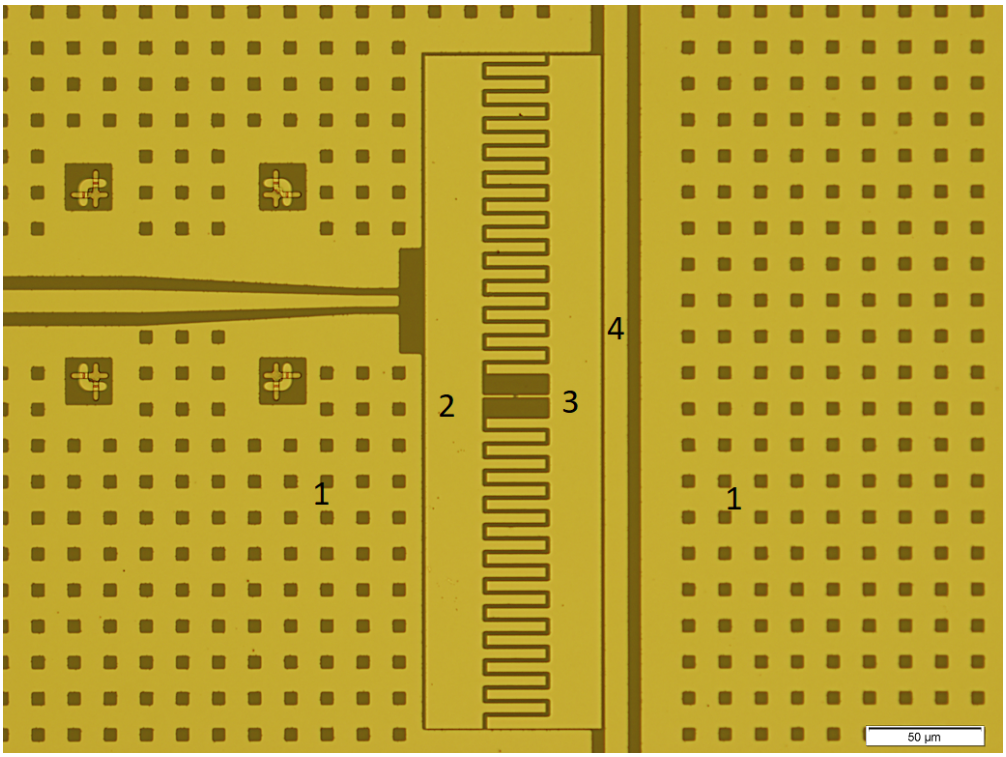

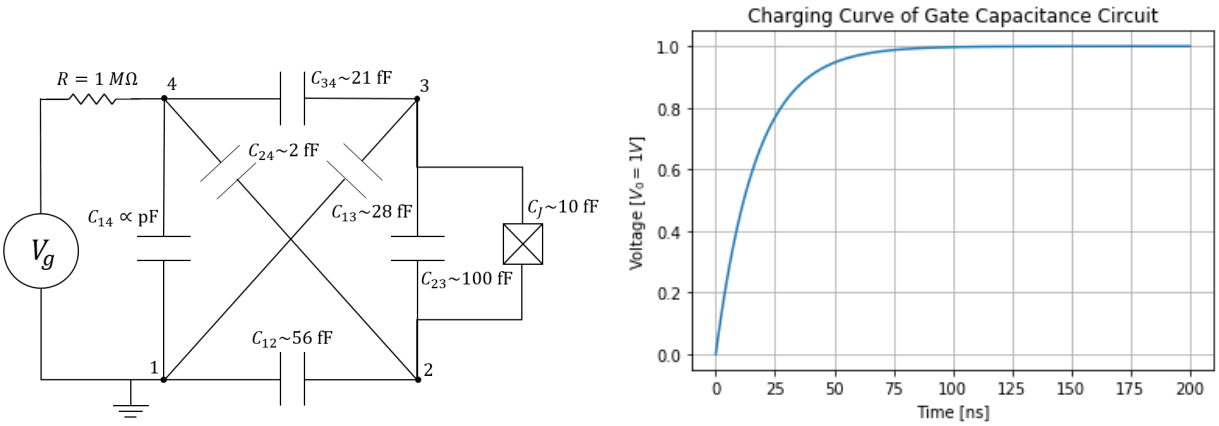

Figure 4.6: (Top) The physical device that was simulated in *Q3D Extractor*. The circuit design was imported in the software and the capactiance network was simulated. A transient simulation is then performed using *QUCS* (Quite Universal Circuit Simulator) by applying 1V to the circuit from completely discharged capacitor state to extract the RC constant. (Left) The capacitance network for the simulated device with an artificial resistor. To extract C_g the capacitances C_{14}, C_{23}, and C_J are dropped from the network. (Right) From the transient simulation the RC constant can be extracted by fitting $V = V_0\left(1 - e^{-t/RC_g}\right)$.

lumped capacitor in the model. This adds an extra term to the gate capacitance of the qubit. Two pulse lines were staggered, one on a matter site and one on the non-adjacent link site to create a direct route for state initialization rather than driving excitations through the cavity. The circuit is shown below in figure 4.7.

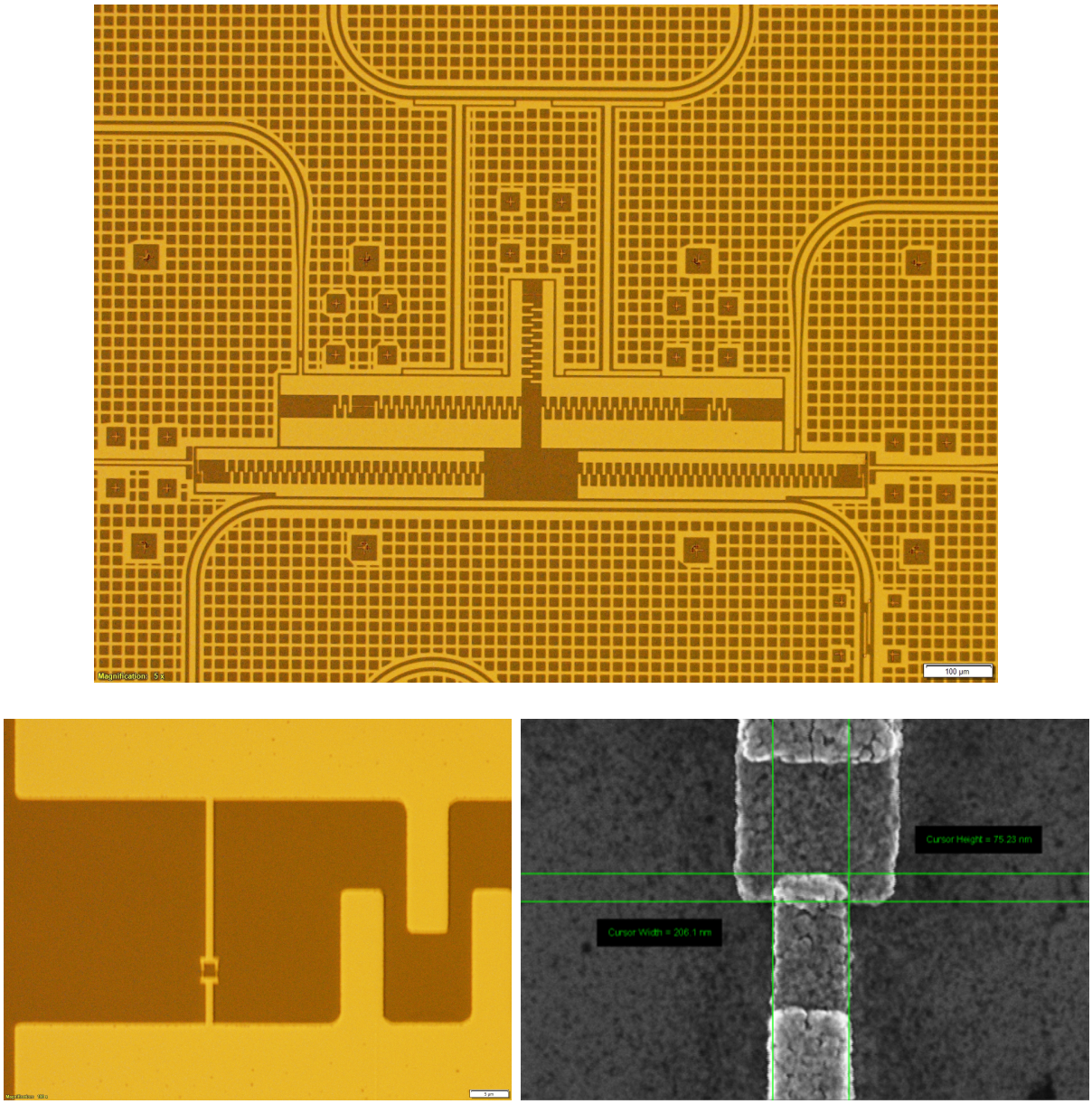

Figure 4.7: (Top) Full four qubit circuit of the first iteration of the quantum simulator. Two transmission lines connect the matter qubits and the link qubits. The link qubits are connected to the transmission line with a small capacitance due to constraints of the layout. Each matter site has a SQUID to tune the qubits into resonance with the link. Two excitation lines are staggered to initialize into the state $|\downarrow 10 \uparrow\rangle$. (Left) SQUID of a separate device for looking at the spectrum of just the link. (Right) SEM of on of the Josephson junctions of the four qubit device. The overlap of the junction corresponded to about half of the estimated overlap during the design phase. This could have been due to error in the design, a fabrication issue during the development of the photoresist, or a miscalculation of the evaporation angle.

Chapter 5

Results and Discussion

5.1 Single Transition Spectrum

To perform the analog simulation of the Schwinger model correctly we are interested in engineering a Hamiltonian that naturally enforces Gauss' law. That is to say that we want to only see transitions in the links if and only if there is a simultaneous transition in the matter sites that reciprocates the change. This processes is mediated by the link sites. The eigenstates at the decoupling point for a fixed manifold cannot have a single photon transition element linking them otherwise the incoherent process of a Jaynes-Cummings like interaction will dominate. The coherent process that obeys Gauss' law is a virtual process which is mediated by the hopping of a matter site to its adjacent link. Plotted in figure 5.1 are the single photon transitions between various levels of the circuit when applying an excitation to the left or right link sites. The large matrix elements are those that can be driven or are virtual processes within the device and the small transition elements will be washed out due to decoherence. From figure 5.1 we can visualize the process in terms of the eigenstates of the link Hamiltonian, $|\psi_i\rangle$. At the decoupled point these eigenstates represent the bare eigenbasis of the two oscillators. In the single excitation manifold, say initializing the link in the states $|\psi_1\rangle$, the virtual process which obeys Gauss' law will keep us in the same manifold. There are two processes which correspond to this. The processes $|\psi_1\rangle \rightarrow |\psi_4\rangle \rightarrow |\psi_2\rangle$ and $|\psi_1\rangle \rightarrow |\psi_g\rangle \rightarrow |\psi_2\rangle$ keep the initial state in the manifold. The a non-zero interference between these two paths allows the gauge invariant dynamics to occur. This transition corresponds to the single excitation hopping from site to site. Figure 5.2 depicts the allowed transitions between energy levels.

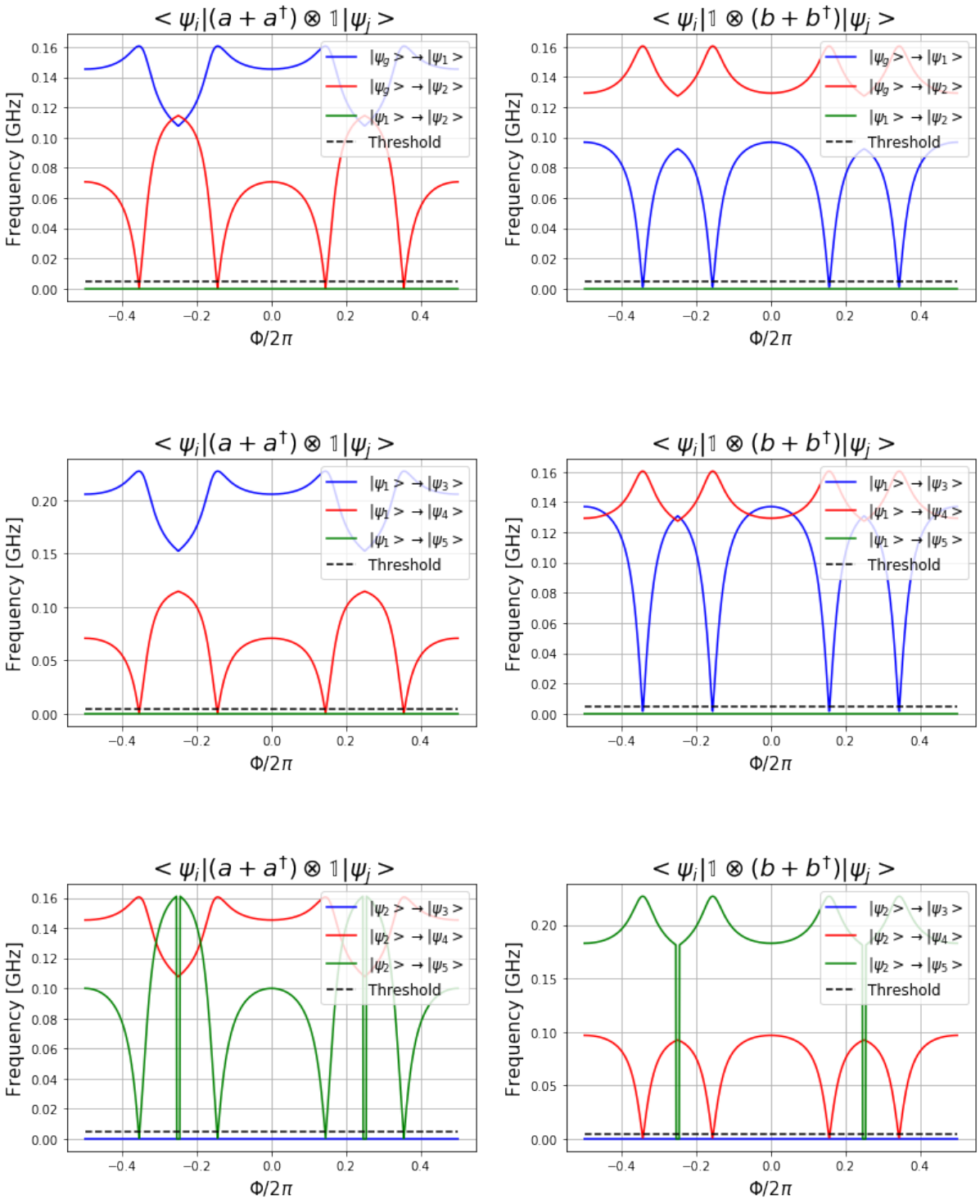

Figure 5.1: Coupling matrix elements for single photon transitions between eigenstates of the Hamiltonian, $|\psi_i\rangle$, as a function of the external flux. In the experimental setup both qubits would be driven simultaneously, but at the decoupling points the left and right qubits are isolated from one another. At the decoupling points the states $|\psi_i\rangle$ correspond to the bare eigenstates of the bosonic annihilation/creation operators. Large elements are the levels that would be seen while performing spectroscopy on the device. A threshold of 5 MHz is used to isolate the couplings from those observable in spectroscopy.

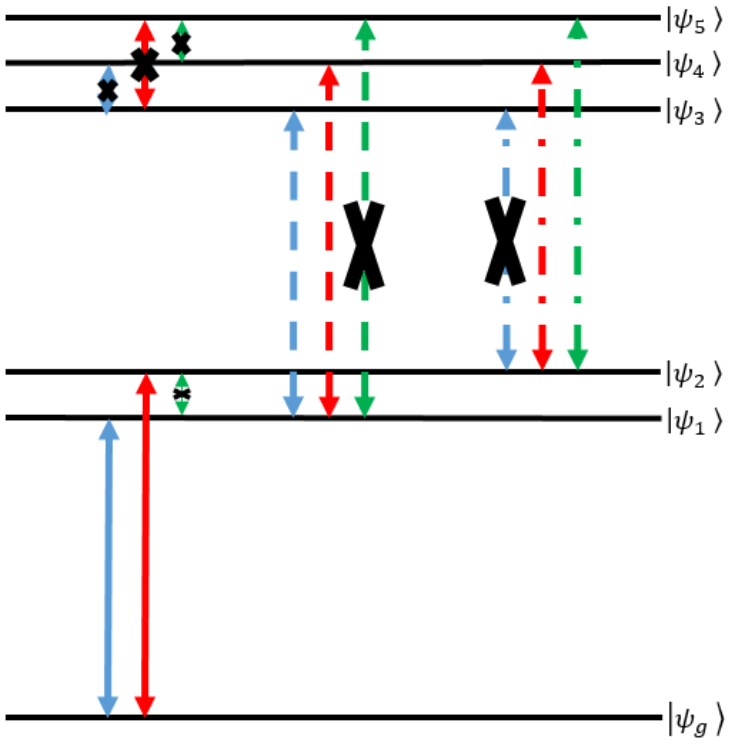

Figure 5.2: Allowed energy transitions between eigenstates corresponding to large matrix elements within the Hamiltonian 3.19. The intra-manifold transitions are suppressed by engineering the Hamiltonian in such a way as to cancel the first order hopping as described in the previous chapter. The gauge invariant processes correspond to those that leave a fixed manifold and have a path to return to that manifold. Processes such as the blue dashed line or green dotted line contribute to the noise processes discussed in later sections. These are gauge invariant, but affect the dynamics and correspond to the fast oscillations in the time dynamics.

5.2 Gauge Invariant Hopping

To achieve the gauge invariant dynamics the device needs to be fabricated with a hierarchy of energy scales in mind. The energy corresponding to the matter fermions (qubits) needs to be on resonance with the frequency of the anharmonic oscillators that are adjacent to the lattice vertex. This amounts to the condition, $\omega_i^q = \omega_i$. By taking the matter sites to be transmons with a split junction these can be tuned into resonance locally with an on chip DC line against the presence of a fixed background field from an external coil which sets the mode decoupling condition of equation 4.21.

From here the next consideration is that the self and cross-Kerr non-linearities of the link suppress gauge variant photon interactions. The are defined according to 4.12 as,

$$\Omega_i = -\frac{\epsilon_i^2}{16}\left(E_{J_i}e^{-\epsilon_i/4} + E_J(\Phi_{ext})e^{-\sqrt{\epsilon_L\epsilon_R}/4}\right) \tag{5.1}$$

$$\Omega_{LR} = -\frac{\epsilon_L\epsilon_R}{4}E_J(\Phi_{ext})e^{-\sqrt{\epsilon_L\epsilon_R}/4} \tag{5.2}$$

The non-linear components of the Hamiltonian are then rewritten as,

$$H_{NL} = \Omega_L a^\dagger a^\dagger a a + \Omega_R\Omega_L b^\dagger b^\dagger b b + \Omega_{LR} a^\dagger a b^\dagger b \tag{5.3}$$

These can then be separated into the definitions of the total link excitation and spin on the link,

$$H_{NL} = W\left(a^\dagger a + b^\dagger b\right)^2 + \frac{g}{2}\left(b^\dagger b - a^\dagger a\right)^2 \tag{5.4}$$

where W and g are defined in equation 4.16. The second term maps onto the notion of energy stored within an electric field of this lattice model. This imposes the restriction that $W > g$ in order to ensure that it is energetically unfavourable to store energy in the link and thus leave the excitation manifold.

The final energy scale is that the Jaynes-Cummings coupling between matter sites and field sites satisfies that $\lambda_i^2/W \sim g$. If this condition is satisfied then applying perturbation theory to second order on the fermion/field coupling recovers the gauge invariant hopping.

5.2.1 Time Domain Simulations

Too see that this Hamiltonian and these parameters faithfully reproduce the dynamics we are hoping to emulate we simulate the time evolution of the quantum circuit using The

Lindblad master equation[38, 12]. The equation is then,

$$\dot{\rho}(t) = -i[H, \rho(t)] + \frac{1}{2}\sum_i \left[2C_i\rho(t)C_i^\dagger - \{C_i^\dagger C_i, \rho(t)\}\right] \tag{5.5}$$

Here $C_i = \sqrt{\Gamma_i}a_i$ where a_i is the lowering operator corresponding to each component of the Hamiltonian and Γ_i is the decay rate for that element. This equation models the effects of a system in an open environment where non-unitary processes affect the outcome.

Starting with the spin-1/2 model we initialize the state as $|\uparrow, m = +1/2, \downarrow\rangle = |\uparrow 01 \downarrow\rangle$. This state corresponds to a system where there is an electron sitting on a lattice site and the field points away from it. As the electron hops from lattice site to lattice site the field must reciprocate this change by changing the direction of the electric field. The state hops between the initial state and the state $|\downarrow, m = -1/2, \uparrow\rangle = |\downarrow 10 \uparrow\rangle$. In the single excitation manifold (spin-1/2 manifold) the matter sites always exhibit confinement. That is the system always has a field polarization linking it to its adjacent neighbour site. This will change when we consider the two excitation manifold (spin-1) manifold where the field now admits a "vacuum" field or more accurately a zero amplitude electric field. In figure 5.3, I have plotted the evolution of the state initialized as above. The bottom left figure tracks the gauge invariant behaviour as the fermions and fields swap positions. There are two major sources of decay. There are the processes corresponding to an excitation being lost completely due to decoherence and loss out of the computational space of the gauge invariant dynamics (see figure 5.4). The system was modelled assuming a decohering system in the absence of pure dephasing so that T_2=2T_1 with each qubit having $T_1 = 50\mu$s. This is well within typical lifespans of cavity-qubit systems.

Initializing the state for the spin-1 dynamics involves creating the state, $|\uparrow, m = 0, \downarrow\rangle = |\uparrow 11 \downarrow\rangle$. This corresponds to a lone unconfined "quark" (or anti-quark) which is located on the left most lattice site. The link of this state corresponds to a vacuum field (not to be confused with the vacuum state of the whole system) or "null" field, $m = 0$. The state then coherently evolves from this unconfined state to one where it is confined as a meson and a linking field polarized between the two lattice sites. The state then hops from $|\uparrow, S = 1, m = 0, \downarrow\rangle$ and $|\downarrow, S = 1, m = -1\rangle$. In a longer chain one can think about this process as starting in a filled Fermi sea. The ground state corresponds to a state with staggered fermions on the links and this "null" field between matter sites. An excitation hopping then forms an electron-hole pair which is joined by the field changing its state to join the pairs.

Both of these situations obey the gauge invariant dynamics we are trying to emulate.

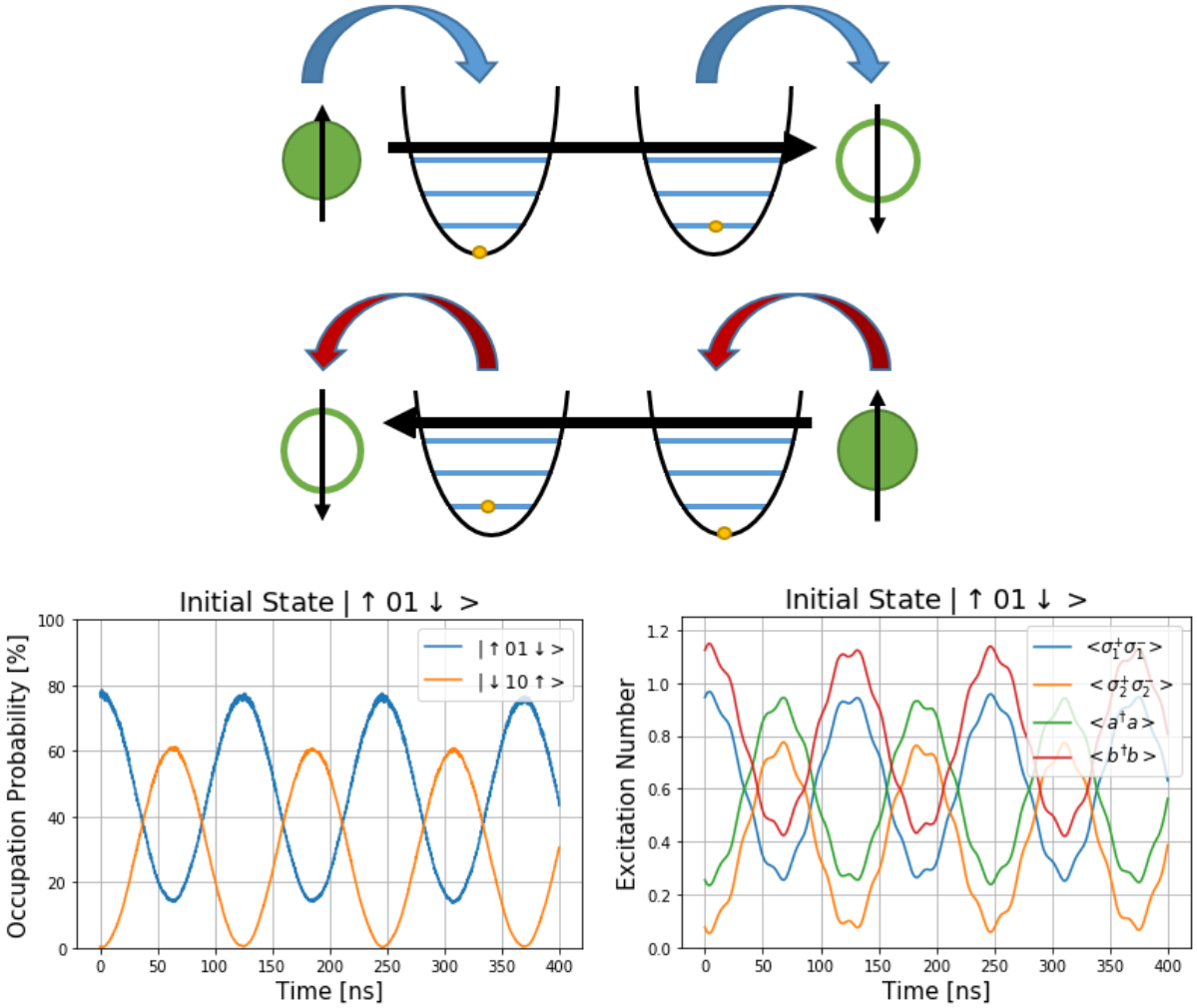

Figure 5.3: (Top) Gauge invariance is captured by seeing the coherent dynamics of the staggered circuit elements exchanging their excitations without a Jaynes-Cummings like hopping. (Bottom) Fast internal oscillations are filtered out using a boxcar window. The fast internal oscillations arise due to correction terms from the second order perturbation. These take the form $S^z\sigma_i^z$ and $\sigma_1^+S^-S^z\sigma_2^-$. They terms preserve the gauge invariant dynamics, but contribute to not seeing a full saturation of the link. A maximum of 80% for the initial state is achieved and only a maximum of 60% is achieved in the saturation of of the corresponding gauge invariant state. These numerical simulations are filtered similarly to how we would handle the filtering on the experimental level. This simulation was performed assuming a T_1 of 50μs. On the left is the evolution of the state. The initial state is prepared as $|\uparrow 01 \downarrow\rangle$ and allowed to evolve. The π phase difference in the oscillations show that the gauge invariant dynamics is being preserved as the state leaks out of the manifold. Left is the number of excitations of each element in the circuit. We can see the oscillations are π out of phase as well and match the expected number of excitations in each element corresponding to the state to the left. Importantly we are not leaving the single excitation manifold other than through decay processes. The odd shape of the total excitation number on the right is due to the intra-manifold leakage as explained below in figure 5.4.

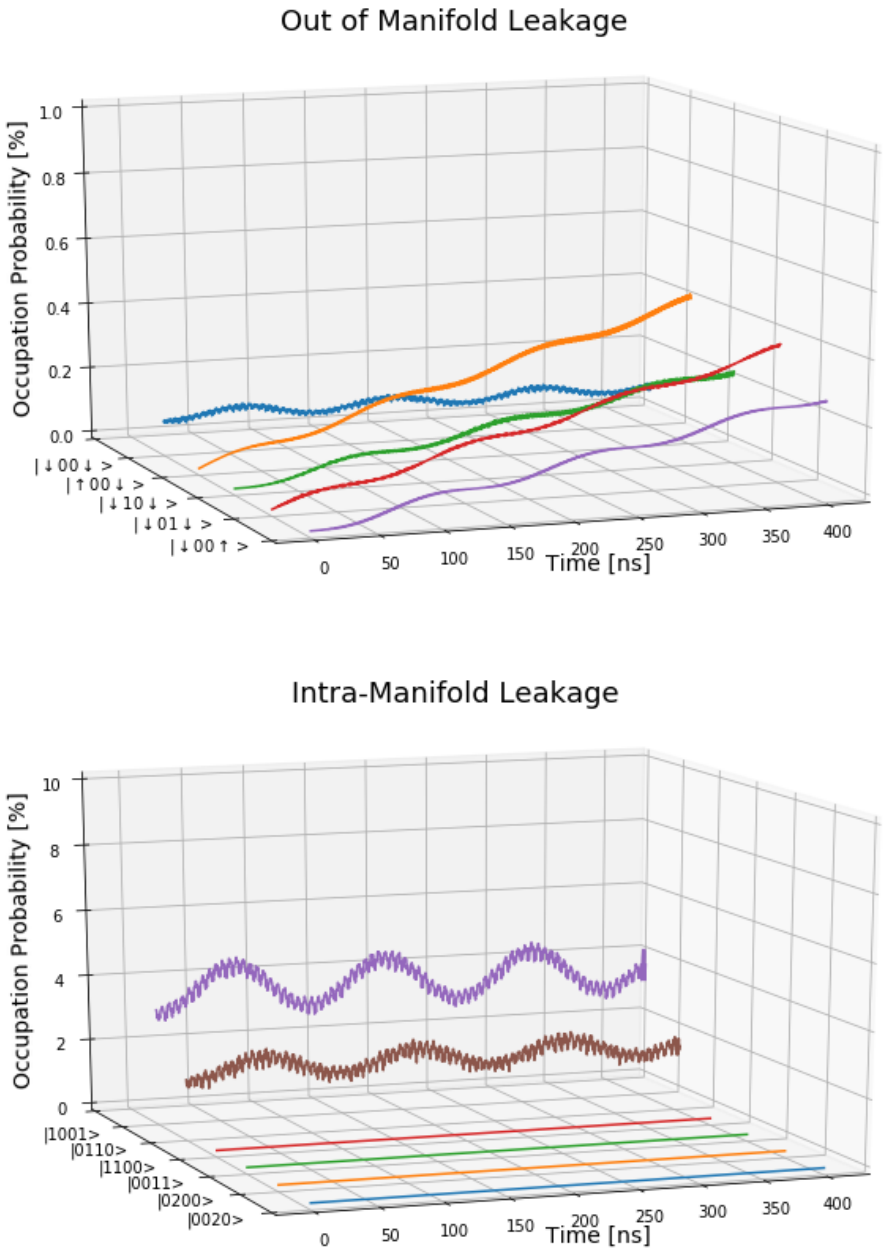

Figure 5.4: The system is initialized the same as in figure 5.3 and averaged using a boxcar to remove the fast oscillations. (Top) As the system evolves in time relaxation causes leakage into the lower lying states. These then decay into the ground state through a cascaded process. (Bottom) Leakage out of the gauge invariant subspace but still within the same excitation manifold. The fast oscillating terms of the dynamics are mainly contributed to by the Jaynes-Cummings hopping from matter site to adjacent link without obeying the gauge invariant dynamics of the model. That is an excitation hops from a matter site without the link reciprocating the change. In both instances leakage out of the initial state affects the visibility of the gauge invariant behaviour. The occupation probability out of the gauge invariant subspace remains small (<5%) well beyond a measurable timescale allowing us to observe the gauge invariant dynamics on realistic timescales.

The states are initialized as eigenstates of the underlying U(1) symmetry given by G_i of equation 3.12 and oscillate between the allowable physical states imposed by the constraint $G_i |\psi\rangle = 0$. If the spin wants to hop to a different position in the lattice the field must reciprocate this by changing it's corresponding direction (see figure 3.4).

While it is important that these dynamics are occurring it is more important from an experimental perspective that these dynamics can occur over a range of the flux passing through the linking circuit rather than the optimal decoupling point. It is difficult to precisely achieve the optimal decoupling of the link so a window around this point should produce the same or similar gauge invariant dynamics. This is shown to be the case in 5.5

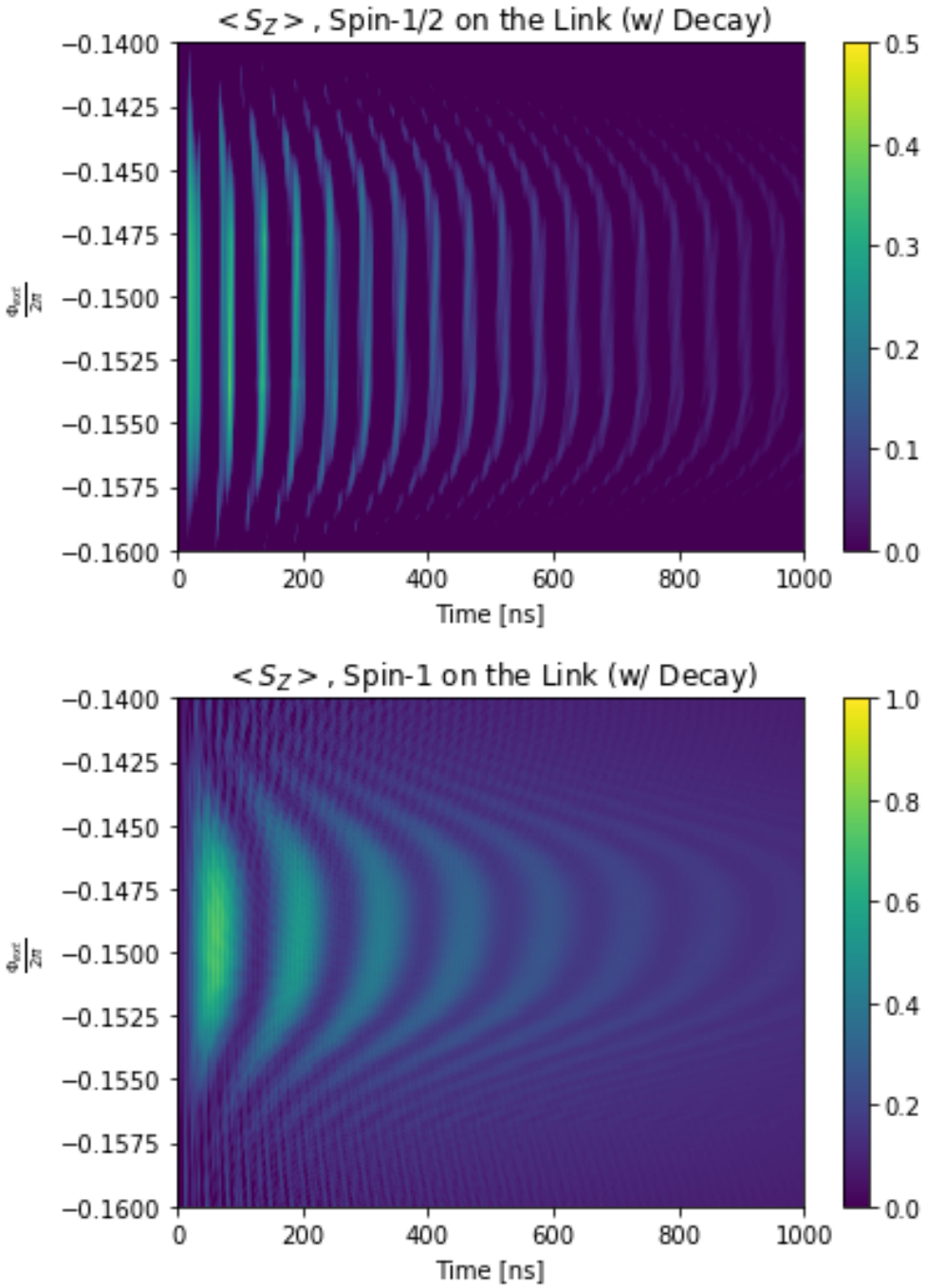

Figure 5.5: Spin excitation remains visible even away from the optimal decoupling point (see eq. 4.21) of $\Phi_{ext}/2\pi = -0.151$. This as well as the decoherence over μs lifetimes lends to the idea that simulating the gauge invariant dynamics is physically realizable. The model is robust enough that variations in design parameters will still allow for the dynamics to be observed provided that the hierarchy of parameters is obeyed. The plot of figure 5.3 corresponds to a horizontal trace at the optimal decoupling point.

5.3 State Preparation & Readout

State preparation is an integral component of developing analog quantum simulators. The initial state for simulating the Schwinger dynamics of the above sections is dependent on being able to accurately prepare states in the eigenbasis of the generator of the gauge invariance (see equation 3.12).

To properly prepare the initial states to observe the gauge dynamics a calibrated π-pulse for each circuit element needs to be characterized. The theory behind single-qubit gates is well studied[16, 41]. An optimal π-pulse to drive a transition using a Gaussian wavepacket requires that the area underneath the Gaussian is equal to π. The two parameters of interest are the amplitude and the half width half max (HWHM) of the Gaussian. By fixing one of the two the other can be solved for from,

$$\sigma = \frac{HWHM}{\sqrt{2\ln(2)}} \tag{5.6}$$

$$A = \frac{\sqrt{\pi\ln(2)}}{HWHM} \tag{5.7}$$

The driving Hamiltonian is then,

$$H_{dr} = A(t)\left(a + a^\dagger\right) = Ae^{-(t-t_0)^2/2\sigma^2}\cos\left(\omega_d t\right)\left(a + a^\dagger\right) \tag{5.8}$$

Here a and $a^\dagger$ are the bosonic creation and annihilation operators. The driving term represents driving a system with a coherent field. in the case of a two level system direct qubit driving takes the form $\sigma^+ + \sigma^-$. However, since we are simulating the transmon qubits as anharmonic oscillators and including the higher levels we directly drive the system with the bosonic creation and annihilation operators at the frequency of the $0 \to 1$ transition. In the presence of limitations due to instrumentation (either bandwidth or maximum amplitudes) a flat time can be introduced to offset the two parameters as long as the area underneath the pulse is kept to π. In coupled systems or systems with decoherence optimal pulse shaping can be performed to prepare states with high fidelity using techniques such as DRAG[49].

Driving a qubit into its excited state will shift a coupled cavity's frequency due to the dispersive shift. By listening to the output of the cavity at one of the dispersed resonator we can infers the state of the qubit. The peak (or trough) of the outgoing signal maps directly onto the excitation state.

High fidelity single shot readout can be readily achieved using a Josephson Paramet-

ric Amplifier (JPA)[34]. State discrimination has reached upwards of 98% over nanoscale timescales[68].

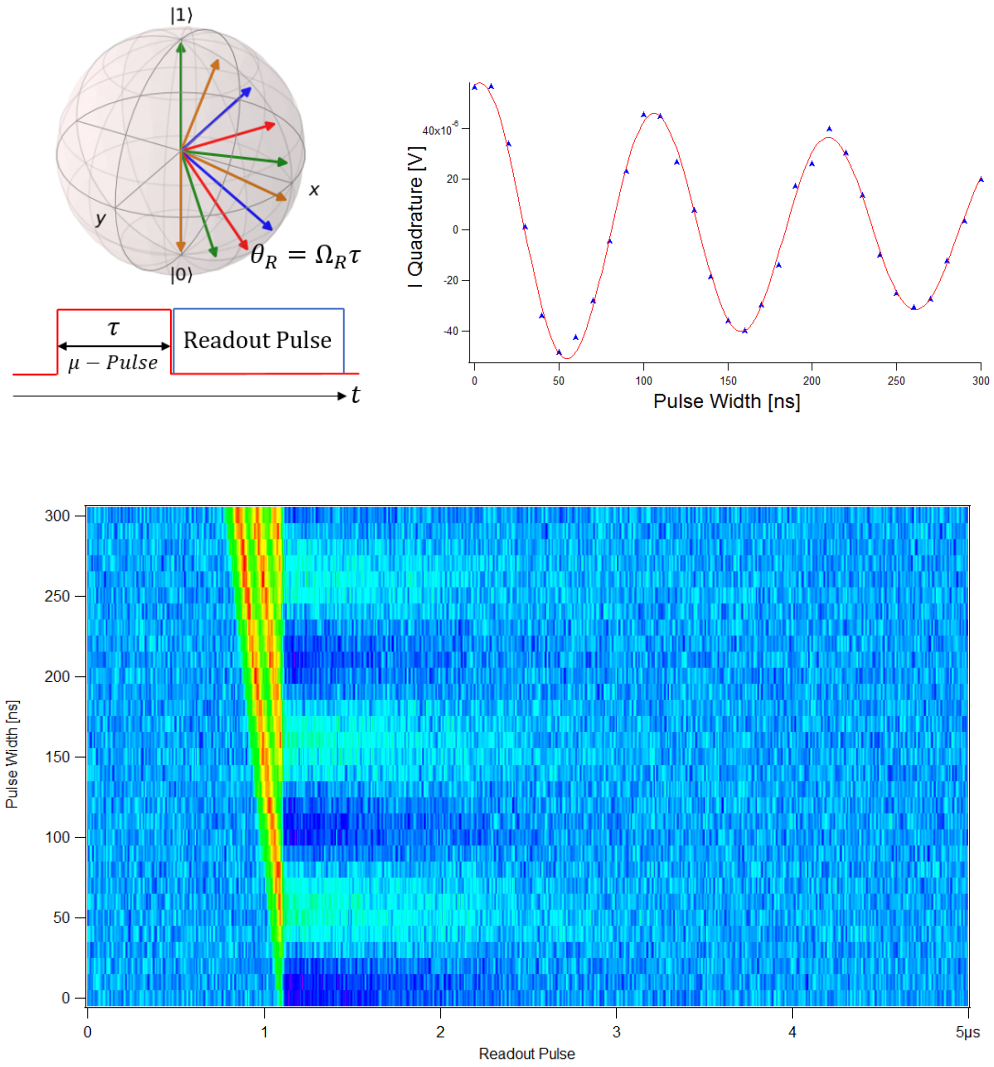

Figure 5.6: (Top Left) The state of the qubit rotates according to the length (or amplitude) of the driving pulse at the qubit frequency. (Top Right) The integrated decay of the Rabi oscillations (Bottom) of the I quadrature. In our recent work[23] the qubit emits directly into an open environment by coupling to the vacuum oscillations of an open transmission line. The single photon emitted from the qubit when it is in the state $|1\rangle$ is a pure Fock state and has no coherence. The coherent signal associated with the I and Q quadratures is thus zero. The I and Q quadratures signal is maximized when the qubit lies on the equator of the Bloch sphere as it is fully coherent. These positions can be used as reference to calibrate for the optimal π and $\pi/2$ times for a given driving amplitude. (Bottom) 2D sweep of the Rabi Oscillations as a function of the pulse width. As the pulse width increases we drive from the ground state and over the excited state. This can be seen in the bands within the Rabi pulse (green and orange) where the internal dynamics of the dephasing are observed.

5.3.1 Pulsing Protocol and Measurements

To observe the spin-1/2 dynamics, control over two qubits needs to be fully characterized. To initialize the state we first bias the link to its decoupled position as found in equation 4.21. The qubits are locally detuned from their adjacent link site. This detuning prevents the qubit-link system from coupling and forming a dressed basis that will affect the driving of the qubit to the excited state. π-pulses excite the circuit into the state $|1010\rangle$. The states have been prepared with a fidelity, $F(\rho_{ideal}, \rho_{prep}) \sim 0.87$. Perfect fidelity is not achieved due to the stray coupling between elements as simulating the state initialization without decoherence achieves similar fidelity. This can be improved by applying pulse optimization techniques such as the DRAG protocol[49]. Tuning the qubit matter sites into resonance with their adjacent link are then left to evolve under the gauge invariant dynamics and read out.

As the qubits coherently swap from $|1010\rangle \rightarrow |0101\rangle$ the cavities are listened to. Oscillations in the cavity population directly correspond to the qubit states using dispersive readout. We can then use this to infer the gauge invariant dynamics by seeing oscillations in the form of figure 5.3 and cross correlating the output.

5.4 Experimental Proposal

The time domain measurements we want to observe necessitate the use of accurate and synchronized microwave pulses. To accomplish this we use a *Signatec PXDAC4800* arbitary waveform generator. The AWG can output wave to four channels allowing full control over the individual qubits within the proposed device. The AWG also allows extremely short pulsing down to nanosecond time scales. This resolution allows for extremely accurate pulse shaping and pulse optimization. Microwave tones are produced via the *SGS100A* by *Rhode & Schwarz*, and *QuickSyn FSW-0020* frequency synthesizer by *National Instruments*. Both offer low phase noise solutions to signal synthesis. The two signals are mixed together to produce the required pulsed output for driving the qubits into their excited states.

Internal to the cryogenic setup are attenuators and filters on the cabling down the the physical samples. The power necessary to drive qubit or resonator excitations for large coupling is given by

$$P \sim n\hbar\omega\Gamma \tag{5.9}$$

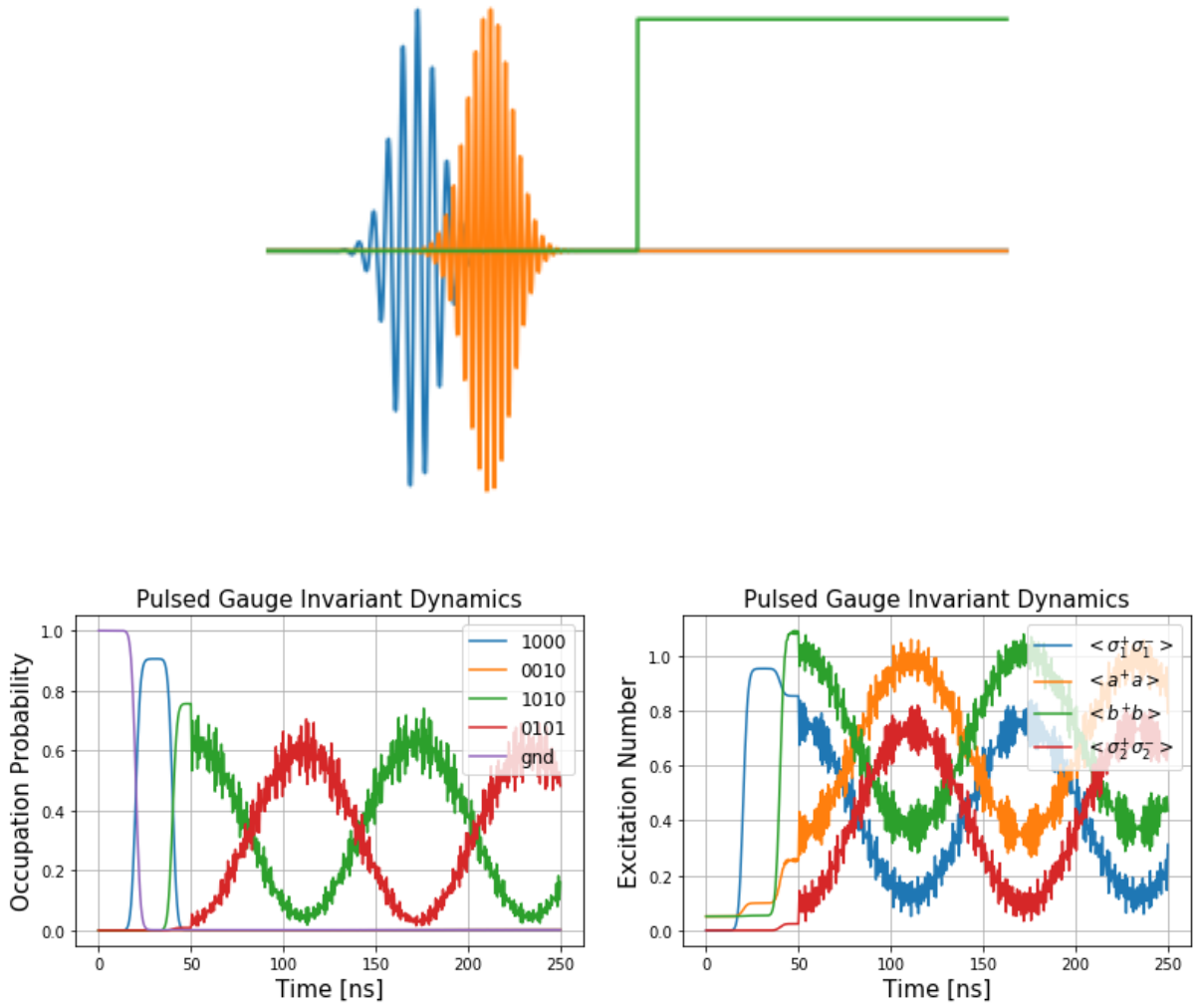

Figure 5.7: (Top) Sketch of the pulse sequence for the spin-1/2 dynamics. The initial state is prepared with the application of two pi pulses (HWHM of 5ns). The two matter qubits are then brought into resonance with the link by tuning the qubits with on-chip DC lines (green pulse). (Bottom) Occupation probability and individual excitations of the pulsed system. The system initially starts in the ground state then is excited to the state $|1000\rangle$. After this the second π-pulse is applied and drives the qubit to the state $|1010\rangle$. The DC pulse (at $t = 50$ns) bring the qubits into resonance and when this occurs the gauge invariant dynamics proceed. The decoherence times for these simulations was 50μs, which is comparable to the decay times for developments in the field. The limiting constraint on the state preparation is intrinsic to the stray couplings of the Hamiltonian and not due to decoherence on the system. This can be be improved through optimized pulsing.

where ω and Γ are the angular frequencies and decay rates of the qubit or resonator and n is the number of photons. For qubits with frequencies on the order of GHz and decay rates on the order of 100 kHz- 1 MHz this corresponds to approximately powers on the order of $\sim 10^{-18}$W or approximately -140dBm and upwards of -80dBm to drive nanosecond Rabi oscillations.

Frequency multiplexing has been readily achieved in several architectures and allows for the addressability of multiple qubits with reduced line overhead. The readout can be performed on a single or few transmission lines coupled to individual cavity resonators and qubits. The scheme lifts some of the constraints of individual readout lines and at the same time allows a clear path forward in terms of scalability[6].

The Analog-Digital-Converter (ADC) takes the signal from the fridge and digitizes it in a way that can be understood and processed. For this we have a *GaGe RazorMax 16* PXIe card. The digitizer can work down to a 2ns resolution well within the times scales of predicted dynamics of the device.

Shown below in figure 5.8 is a sample setup of the experiment.

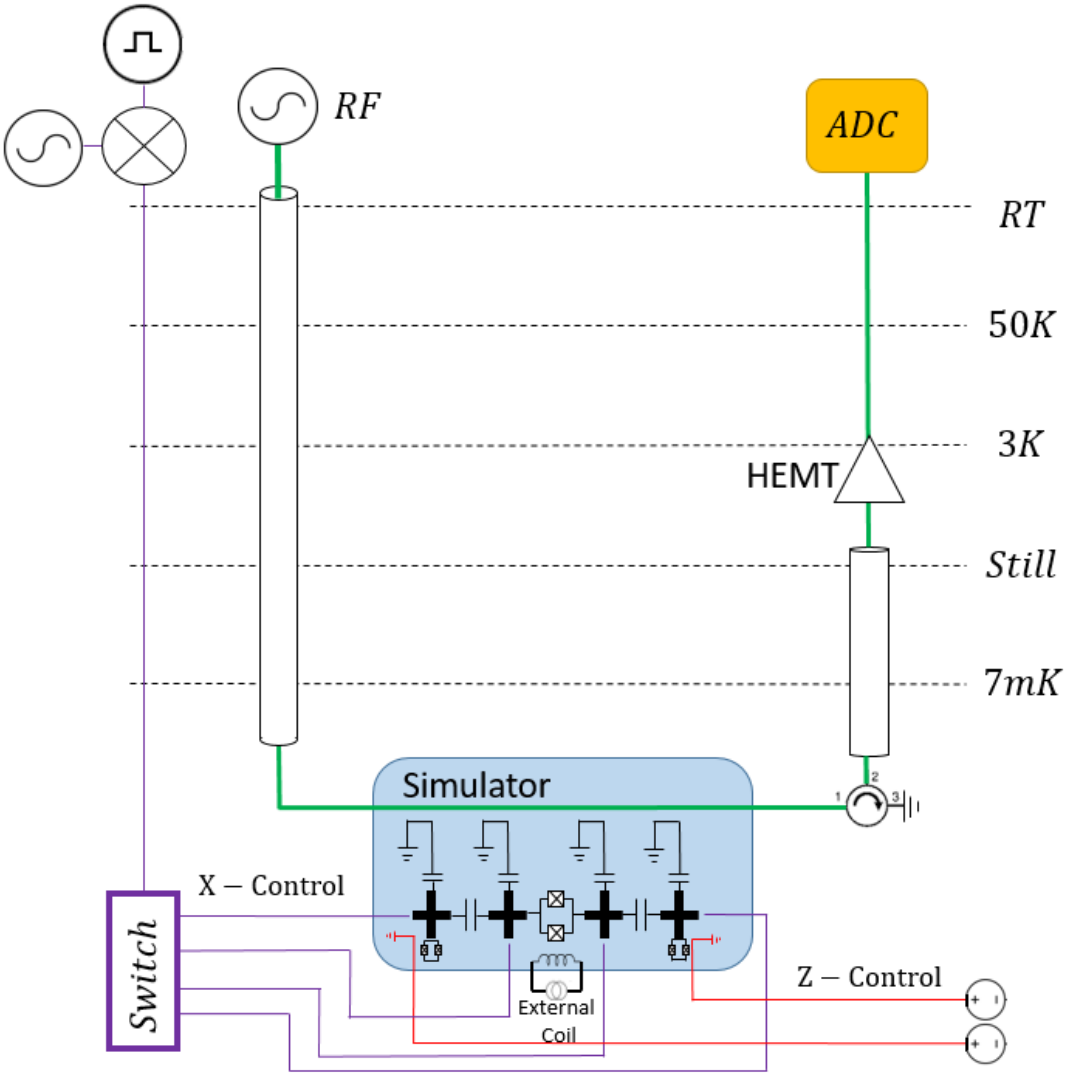

Figure 5.8: Simplified setup of the proposed experiment. Starting at room temperature the π-pulses (Purple) can be generated by mixing RF signals with a DC pulse generated from a AWG to create shaped outputs. These can then be routed to the individual qubits to prepare the initial state. Readout pulses are generated with another RF source (Green). The readout of the qubits is multiplexed removing the need to have individual readout lines for each individual qubit. The output from the device can then be amplified using a combination of a JPA (not depicted), a HEMT, and room temperature amplifiers to be digitized and processed in the analog-digital converter. The coil can be tuned to create a static background field for setting the decoupling of the two link qubits and local on-chip DC fast flux lines can be used to tune the matter site qubits individually (Red) and apply Z pulses.

Chapter 6

Conclusions & Future Direction

This thesis has aimed to present the feasibility of physically implementing an analog quantum simulator.

In chapter 2 we outlined the theory of superconducting quantum circuits and presented the building blocks necessary to create large scale quantum circuits.

The focus of chapter 3 was to present the theory and models of lattice gauge theories and why they are an interesting field of study. Here we also sought to bridge the gap between the language of LGTs and superconducting qubits. We found that by using transmons to implement LGTs was extremely useful. By selectively taking advantage of the transmon's multilevel structure we can get away with expressing both fermionic and bosonic degrees of freedom as transmons make good qubits, but bad two-level systems due to the presence of higher modes.

In chapter 4 we worked towards demonstrating that a physical design was indeed achievable using realistic parameters from a fabrication perspective and was faithful towards the hierarchy of energy scales necessary to implement the gauge invariant dynamics. As well we explored design aspects of developing superconducting qubits and presented a methodology of engineering and simulating the the parameter space compared against experimentally observed values.

In chapter 5 we outlined the experimental observations we would need to observe to demonstrate a faithful implementation of the Schwinger model. To achieve the Schwinger model we need to demonstrate that there is mode decoupling between the link qubits so as to suppress an incoherent Jaynes-Cummings like hopping from site to site and instead produce a coherent hopping that mimics the gauge invariant dynamics which preserve Gauss's Law.

We also demonstrated that the model can be designed in such a robust way that the dynamics can be observed in a region around the optimal decoupling point for both the spin-1/2 and spin-1 manifolds. We also presented a simple protocol to initialize the system so as to observe the gauge invariant dynamics.

The steps outlined here are the beginnings of moving towards large scale quantum simulation. These simple demonstrations show what the true power of what quantum computers will show in the near future. It has only been a few years since the superconducting architecture arose and has seen startling progress over such a short period. Small scale error correction has been implemented, new regimes of physics in the ultra-strong coupling range, and the first cloud quantum computers. These small but impressive feats have spurred commercial interests in the field and continue to accelerate it forward. In keeping with the culture of constantly pushing the boundaries that is so common in the field I present some considerations on improving and extending the work of this thesis.

6.1 Scaling 1D Simulations

The proposed implementation consists of just a single building block for larger scale quantum simulation. Combing these blocks into larger chains the toy model presented of confinement becomes less superficial. In a longer lattice where the initial state is given by a confined pair of adjacent lattice sites, $|...\rangle \otimes |2010\rangle \otimes |...\rangle$ the gauge invariant dynamics are observed when adding a flux to adjacent links. This forces the matter site to hop to the next lattice position to preserve the gauge invariant dynamics and obey Gauss' law. As we continue to force the separation of the matter sites the tension on the "string" increases and it becomes energetically favourable to break the confined structure and spontaneously create two confined pairs. A small simulation of $L = 4$ lattice sites would in principle be able to demonstrate this as there would be no "unphysical" disconnected mesons as there is in the case for the $L = 2$ lattice.

6.2 Moving Into 2D Architectures

The next natural extension of a one dimension lattice gauge simulator is to begin moving into two dimensional architectures. Recent work[45] has shown that implementations of a 2D architecture on superconducting devices is readily achievable. These models have far reaching applications into moving towards both more realistic simulations of QCD as well as the

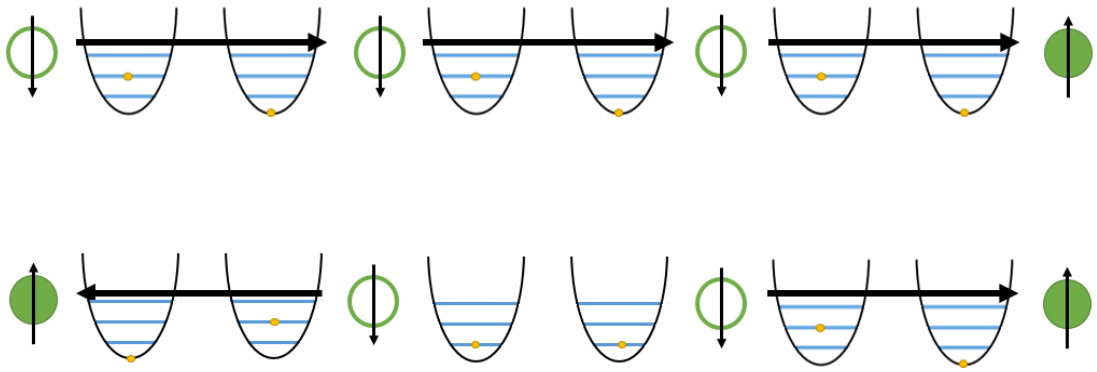

Figure 6.1: String breaking of a $L = 4$ chain. Two spatially separated lattice sites are confined by a linking field. By increasing the "mass" (detuning of the matter site qubits in the model) of the lattice sites it becomes more energetically favourable to spontaneously break the string and form two disconnected pairs.

beginnings of building towards applications in condensed matter. In particular the quantum dimer model (see [48] for a good overview) which was originally developed to understand the origins of high temperature superconductivity, but has applications in understanding the lattice structure of hydrogen bonds in ice. A superconducting implementation would go a long way towards demonstrating the true power of quantum simulation.

6.3 Digital-Analog Hybrids

Combining the two paradigms of digital and analog quantum simulation would give great insight into how to move the field forwards towards a fully universal architecture. Recent proposals[36] have shown that there are efficient techniques to combine the knowledge that already exists for two levels systems and qubits digitally with the analog bosonic degrees of freedom we get for free from transmission lines and these multilevel systems. In principle this would allow us to explore previously untouched regimes of physics.

Bibliography

[1] Ambegaokar, V., and Baratoff, A. Tunneling Between Superconductors. *Physical Review Letters 11*, 2 (jul 1963), 104–104.

[2] Anderson, P. W., and Rowell, J. M. Probable Observation of the Josephson Superconducting Tunneling Effect. *Physical Review Letters 10*, 6 (mar 1963), 230–232.

[3] Babbush, R., Berry, D. W., Kivlichan, I. D., Wei, A. Y., Love, P. J., and Aspuru-Guzik, A. Exponentially more precise quantum simulation of fermions in second quantization. *New Journal of Physics 18* (2016).

[4] Banks, T., Susskind, L., and Kogut, J. Strong-coupling calculations of lattice gauge theories: (1 + 1)-dimensional exercises. *Physical Review D 13*, 4 (feb 1976), 1043–1053.

[5] Bardeen, J., Cooper, L., and Schrieffer, J. Microscopic theory of superconductivity. *Physical Review 106* (1957), 162–164.

[6] Barends, R., Kelly, J., Megrant, A., Veitia, A., Sank, D., Jeffrey, E., White, T. C., Mutus, J., Fowler, A. G., Campbell, B., Chen, Y., Chen, Z., Chiaro, B., Dunsworth, A., Neill, C., O'Malley, P., Roushan, P., Vainsencher, A., Wenner, J., Korotkov, A. N., Cleland, A. N., and Martinis, J. M. Superconducting quantum circuits at the surface code threshold for fault tolerance. *Nature 508*, 7497 (apr 2014), 500–503.

[7] Benioff, P. The computer as a physical system: A microscopic quantum mechanical Hamiltonian model of computers as represented by Turing machines. *Journal of Statistical Physics 22* (1980), 563–591.

[8] Benioff, P. Quantum mechanical hamiltonian models of turing machines. *Journal of Statistical Physics 29* (1982), 515–546.

[9] Benioff, P. A. Quantum mechanical Hamiltonian models of discrete processes that erase their own histories: Application to Turing machines. *International Journal of Theoretical Physics 21* (1982), 177–201.

[10] Blais, A., Huang, R.-S., Wallraff, A., Girvin, S. M., and Schoelkopf, R. J. Cavity quantum electrodynamics for superconducting electrical circuits: An architecture for quantum computation. *Physical Review A 69*, 6 (jun 2004), 062320.

[11] Brennen, G., Pupillo, G., Rico, E., Stace, T., and Vodola, D. Loops and Strings in a Superconducting Lattice Gauge Simulator. *Physical Review Letters 117*, 24 (dec 2016), 240504.

[12] Breuer, H.-P., and Petruccione, F. Concepts and methods in the theory of open quantum systems.

[13] Brown, K. R., Clark, R. J., and Chuang, I. L. Limitations of Quantum Simulation Examined by Simulating a Pairing Hamiltonian Using Nuclear Magnetic Resonance. *Physical Review Letters 97*, 5 (aug 2006), 050504.

[14] Brune, M., Schmidt-Kaler, F., Maali, A., Dreyer, J., Hagley, E., Raimond, J. M., and Haroche, S. Quantum Rabi Oscillation: A Direct Test of Field Quantization in a Cavity. *Physical Review Letters 76*, 11 (mar 1996), 1800–1803.

[15] Burkard, G., Koch, R. H., and DiVincenzo, D. P. Multilevel quantum description of decoherence in superconducting qubits. *Phys. Rev. B 69* (2004), 64503.

[16] Chow, J. M., DiCarlo, L., Gambetta, J. M., Motzoi, F., Frunzio, L., Girvin, S. M., and Schoelkopf, R. J. Optimized driving of superconducting artificial atoms for improved single-qubit gates. *Physical Review A 82*, 4 (oct 2010), 040305.

[17] Cui, J.-M., Huang, Y.-F., Wang, Z., Cao, D.-Y., Wang, J., Lv, W.-M., Luo, L., del Campo, A., Han, Y.-J., Li, C.-F., and Guo, G.-C. Experimental Trapped-ion Quantum Simulation of the Kibble-Zurek dynamics in momentum space. *Scientific Reports 6*, 1 (dec 2016), 33381.

[18] Deutsch, D., and Jozsa, R. Rapid Solution of Problems by Quantum Computation. *Proceedings of the Royal Society A: Mathematical, Physical and Engineering Sciences 439* (1992), 553–558.

[19] Dolan, G. J. Offset masks for liftoff photoprocessing. *Applied Physics Letters 31*, 5 (sep 1977), 337–339.

[20] Douglass, D. H., and Meservey, R. Energy Gap Measurements by Tunneling Between Superconducting Films. I. Temperature Dependence. *Physical Review 135*, 1A (jul 1964), A19–A23.

[21] Feynman, R. P. Simulating physics with computers. *International Journal of Theoretical Physics 21* (1982), 467–488.

[22] Forn-Diaz, P., Garcia-Ripoll, J., Peropadre, B., Orgiazzi, J.-L., Yurtalan, M., Belyansky, R., Wilson, C., and Lupascu, A. Ultrastrong coupling of a single artificial atom to an electromagnetic continuum in the nonperturbative regime. *Nature Physics 13*, 1 (2017), 39–43.

[23] Forn-Díaz, P., Warren, C. W., Chang, C. W. S., Vadiraj, A. M., and Wilson, C. M. Shaped, on-demand microwave single-photon generator.

[24] Fowler, A. G., Mariantoni, M., Martinis, J. M., and Cleland, A. N. Surface codes: Towards practical large-scale quantum computation. *Physical Review A 86*, 3 (sep 2012), 032324.

[25] Ghosh, J., and Sanders, B. C. Quantum simulation of macro and micro quantum phase transition from paramagnetism to frustrated magnetism with a superconducting circuit. *New Journal of Physics 18*, 3 (mar 2016), 033015.

[26] Ginzburg V.L., Landau, L. On the theory of superconductivity. *Zhumal Eksperimental'noi i Teoreticheskoi Fiziki 20*, 1064 (1950).

[27] Gross, D. J., and Wilczek, F. Ultraviolet Behavior of Non-Abelian Gauge Theories. *Physical Review Letters 30*, 26 (jun 1973), 1343–1346.

[28] Grover, L. K. A fast quantum mechanical algorithm for database search. *Proceedings of the twenty-eighth annual ACM symposium on Theory of computing - STOC '96* (1996), 212–219.

[29] Jaynes, E., and Cummings, F. Comparison of quantum and semiclassical radiation theories with application to the beam maser. *Proceedings of the IEEE 51*, 1 (1963), 89–109.

[30] Jordan, P., and Wigner, E. P. About the Pauli exclusion principle. *Z. Phys. 47* (1928), 631–651.

[31] Josephson, B. Possible new effects in superconductive tunnelling. *Physics Letters 1*, 7 (jul 1962), 251–253.

[32] Koch, J., Yu, T. M., Gambetta, J., Houck, a. a., Schuster, D. I., Majer, J., Blais, A., Devoret, M. H., Girvin, S. M., and Schoelkopf, R. J. Charge-insensitive qubit design derived from the Cooper pair box. *Physical Review A - Atomic, Molecular, and Optical Physics 76* (2007), 1–19.

[33] Kogut, J., and Susskind, L. Hamiltonian formulation of Wilson's lattice gauge theories. *Physical Review D 11*, 2 (jan 1975), 395–408.

[34] Krantz, P., Bengtsson, A., Simoen, M., Gustavsson, S., Shumeiko, V., Oliver, W. D., Wilson, C. M., Delsing, P., and Bylander, J. Single-shot read-out of a superconducting qubit using a Josephson parametric oscillator. *Nature Communications 7* (may 2016), 11417.

[35] Lahav, O., Itah, A., Blumkin, A., Gordon, C., Rinott, S., Zayats, A., and Steinhauer, J. Realization of a Sonic Black Hole Analog in a Bose-Einstein Condensate. *Physical Review Letters 105*, 24 (dec 2010), 240401.

[36] Lamata, L. Digital-analog quantum simulation of generalized Dicke models with superconducting circuits. *Scientific Reports 7* (mar 2017), 43768.

[37] Lanyon, B. P., Whitfield, J. D., Gillett, G. G., Goggin, M. E., Almeida, M. P., Kassal, I., Biamonte, J. D., Mohseni, M., Powell, B. J., Barbieri, M., Aspuru-Guzik, A., and White, A. G. Towards quantum chemistry on a quantum computer. *Nature Chemistry 2* (2010), 106–111.

[38] Lindblad, G. On the generators of quantum dynamical semigroups. *Communications in Mathematical Physics 48*, 2 (jun 1976), 119–130.

[39] Lloyd, S. Universal Quantum Simulators. *Science 273*, 5278 (aug 1996), 1073–1078.

[40] London, F., and London, H. The Electromagnetic Equations of the Supraconductor. *Proceedings of the Royal Society A: Mathematical, Physical and Engineering Sciences 149* (1935), 71–88.

[41] Lucero, E., Kelly, J., Bialczak, R. C., Lenander, M., Mariantoni, M., Neeley, M., O'Connell, A. D., Sank, D., Wang, H., Weides, M., Wenner, J., Yamamoto, T., Cleland, A. N., and Martinis, J. M. Reduced phase error through optimized control of a superconducting qubit. *Physical Review A 82*, 4 (oct 2010), 042339.

[42] Machta, B. B., Chachra, R., Transtrum, M. K., and Sethna, J. P. Parameter Space Compression Underlies Emergent Theories and Predictive Models. *Science 342*, 6158 (nov 2013), 604–607.

[43] Manousakis, E. A quantum-dot array as model for copper-oxide superconductors: A dedicated quantum simulator for the many-fermion problem. *Journal of Low Temperature Physics 126* (2002), 1501–1514.

[44] Marcos, D., Rabl, P., Rico, E., and Zoller, P. Superconducting circuits for quantum simulation of dynamical gauge fields. *Physical Review Letters 111* (2013).

[45] Marcos, D., Widmer, P., Rico, E., Hafezi, M., Rabl, P., Wiese, U.-J., and Zoller, P. Two-dimensional lattice gauge theories with superconducting quantum circuits. *Annals of Physics 351* (dec 2014), 634–654.

[46] Martinez, E. A., Muschik, C. A., Schindler, P., Nigg, D., Erhard, A., Heyl, M., Hauke, P., Dalmonte, M., Monz, T., Zoller, P., and Blatt, R. Real-time dynamics of lattice gauge theories with a few-qubit quantum computer. *Nature 534*, 7608 (jun 2016), 516–519.

[47] Mezzacapo, A., Rico, E., Sab??n, C., Egusquiza, I. L., Lamata, L., and Solano, E. Non-Abelian SU(2) Lattice Gauge Theories in Superconducting Circuits. *Physical Review Letters 115* (2015).

[48] Moessner, R., and Raman, K. S. Quantum dimer models.

[49] Motzoi, F., Gambetta, J. M., Rebentrost, P., and Wilhelm, F. K. Simple Pulses for Elimination of Leakage in Weakly Nonlinear Qubits. *Physical Review Letters 103*, 11 (sep 2009), 110501.

[50] O'Malley, P., Babbush, R., Kivlichan, I., Romero, J., McClean, J., Barends, R., Kelly, J., Roushan, P., Tranter, A., Ding, N., Campbell, B., Chen, Y., Chen, Z., Chiaro, B., Dunsworth, A., Fowler, A., Jeffrey, E., Lucero, E., Megrant, A., Mutus, J., Neeley, M., Neill, C., Quintana, C., Sank, D., Vainsencher, A., Wenner, J., White, T., Coveney, P., Love, P., Neven, H., Aspuru-Guzik, A., and Martinis, J. Scalable Quantum Simulation of Molecular Energies. *Physical Review X 6*, 3 (jul 2016), 031007.

[51] Onnes, H. The resistance of pure mercury at helium temperatures. *Commun.Phys. Lab. Univ. Leiden 12* (1911), 120.

[52] Ono, T., Moribe, Y., Takashima, S., Ichinose, I., Matsui, T., and Sakakibara, K. Phase structure of a U(1) lattice gauge theory with dual gauge fields. *Nuclear Physics B 764*, 3 (mar 2007), 168–182.

[53] Peskin, M., and Schroeder, D. *An Introduction To Quantum Field Theory*. Frontiers in Physics. Avalon Publishing, 1995.

[54] Politzer, H. D. Reliable Perturbative Results for Strong Interactions? *Physical Review Letters 30*, 26 (jun 1973), 1346–1349.

[55] Rico, E. Private Correspondence, 2016.

[56] Sakurai, J., and Napolitano, J. *Modern Quantum Mechanics*, second ed. Addison-Wesley, San Francisco, 2011.

[57] Sarovar, M., Zhang, J., and Zeng, L. Reliability of analog quantum simulation. *EPJ Quantum Technology 4*, 1 (dec 2017), 1.

[58] Schuster, D. *Circuit Quantum Electrodynamics*. PhD thesis, Yale University, 2007.

[59] Schwinger, J. Gauge Invariance and Mass. II. *Physical Review 128*, 5 (dec 1962), 2425–2429.

[60] Shor, P. Algorithms for quantum computation: discrete logarithms and factoring, 1994.

[61] Simons, R. *Coplanar Waveguide Circuits, Components, and Systems*. John Wiley & Sons, New York, 2001.

[62] Somaroo, S., Tseng, C. H., Havel, T. F., Laflamme, R., and Cory, D. G. Quantum Simulations on a Quantum Computer. *Physical Review Letters 82*, 26 (jun 1999), 5381–5384.

[63] Suzuki, M. Generalized Trotter's formula and systematic approximants of exponential operators and inner derivations with applications to many-body problems. *Communications in Mathematical Physics 51*, 2 (jun 1976), 183–190.

[64] Tinkham, M. *Introduction to Superconductivity*. McGraw-Hill Inc., New York, 1996.

[65] Transtrum, M. K., Machta, B. B., Brown, K. S., Daniels, B. C., Myers, C. R., and Sethna, J. P. Perspective: Sloppiness and emergent theories in physics, biology, and beyond. *The Journal of Chemical Physics 143*, 1 (jul 2015), 010901.

[66] Troyer, M., and Wiese, U.-J. Computational Complexity and Fundamental Limitations to Fermionic Quantum Monte Carlo Simulations. *Physical Review Letters 94*, 17 (may 2005), 170201.

[67] Wallraff, A., Schuster, D. I., Blais, A., Frunzio, L., Huang, R.-S., Majer, J., Kumar, S., Girvin, S. M., and Schoelkopf, R. J. Strong coupling of a single photon to a superconducting qubit using circuit quantum electrodynamics. *Nature 431*, 7005 (sep 2004), 162–167.

[68] Walter, T., Kurpiers, P., Gasparinetti, S., Magnard, P., Potočnik, A., Salathé, Y., Pechal, M., Mondal, M., Oppliger, M., Eichler, C., and Wallraff, A. Rapid High-Fidelity Single-Shot Dispersive Readout of Superconducting Qubits. *Physical Review Applied 7*, 5 (may 2017), 054020.

[69] Wiese, U.-J. Ultracold quantum gases and lattice systems: quantum simulation of lattice gauge theories. *Annalen der Physik 525*, 10-11 (nov 2013), 777–796.

[70] Wilson, K. G. Confinement of quarks. *Physical Review D 10*, 8 (oct 1974), 2445–2459.

[71] Zagoskin, A. M., Rakhmanov, A. L., Savel'ev, S., and Nori, F. Quantum metamaterials: Electromagnetic waves in Josephson qubit lines. *Physica Status Solidi (B) Basic Research 246* (2009), 955–960.

[72] Zangwill, A. *Modern Electrodynamics*. Cambridge University Press, Cambridge, 2013.

Appendix A

Simulation Code

A.1 Parameter Space Conditions

```
"""
@author: Chris Warren
@Institute: Institute for Quantum Computing, University of Waterloo

Calculations of the conditions as per equations 4.7,4.9

Off_Resonsnace_Cond(args): calculates the difference between the two link qubit
                           resonances

Parameter_Cancellation_Cond(args): calculates the cancellation between the
                                   first order hopping terms

See figure 3.5
EjL: Left link's junction energy
EJ:  Linking junction energy
EjR: Right link's junction energy
CL:  Left capacitance
Cj:  Junction capacitance
CR:  Right capacitance
"""
fname = 'ParameterConditions'
import numpy as np
import matplotlib.pyplot as plt
import datetime as dt

def Off_Resonance_Cond(EjL,EJ,EjR,CL,Cj,CR):
    e_charge = 1.602e-19                    #electron charge
    h = 6.626e-34                           #planck's constant
    C_to_GHz = (e_charge**2)/(h*1e9)        #e^2/(hC)  gives frequency in GHz

    C_det = 1.0/(Cj*CL + Cj*CR + CL*CR)     #Determinant of cap matrix
    eps_L = 2*np.sqrt((Cj+CR)*C_det*C_to_GHz/(EJ+EjL))
    eps_R = 2*np.sqrt((Cj+CL)*C_det*C_to_GHz/(EJ+EjR))
```

```
    return (EJ+EjL)*eps_L - (EJ+EjR)*eps_R    #[GHz]

def Parameter_Cancellation_Cond(EjL,EJ,EjR,CL,Cj,CR):
    return (EjL/EJ + 1)*(EjR/EJ + 1) - (CL/Cj + 1)*(CR/Cj + 1)

#Setup Sweep parameters
Ej = np.linspace(1,101,1000)
Cj = np.linspace(1e-15,101e-15,1000)
#Generate storage matrices
A = np.zeros((len(Ej),len(Cj)))
B = np.zeros((len(Ej),len(Cj)))
#Sweep the conditions and store the results
for i,E in enumerate(Ej):
    A[i,:] = Off_Resonance_Cond(17.0,E,16,65e-15,Cj,48.8e-15)
    B[i,:] = Parameter_Cancellation_Cond(17.0,E,16,65e-15,Cj,48.8e-15)
##Uncomment to save data
#today = dt.datetime.now()
#outname = fname + '_{}_{}{}{}.txt'.format('FirstCondition',
#                                          today.year,
#                                          today.month,
#                                          today.day)
##np.savetxt(outname,A,fmt='%f',delimiter=',')
#outname = fname + '_{}_{}{}{}.txt'.format('SecondCondition',
#                                          today.year,
#                                          today.month,
#                                          today.day)
#np.savetxt(outname,B,fmt='%f',delimiter=',')

#2D plotting first condition
plt.pcolor(Cj*1e15,Ej,A,cmap='RdBu',vmin=-1, vmax=1)
plt.xlabel(r'Capacitance, $C_J$ [fF]')
plt.ylabel(r'Josephson Energy $E_j$ [GHz]')
plt.colorbar()
plt.grid()
plt.show()
#2D plotting second condition
plt.pcolor(Cj*1e15,Ej,B,cmap='RdBu',vmin=-0.5,vmax=0.5)
plt.xlabel(r'Capacitance, $C_J$ [fF]')
plt.ylabel(r'Josephson Energy $E_j$ [GHz]')
plt.colorbar()
plt.grid()
plt.show()
```

A.2 Static Hamiltonian Calculations

```
"""
@author: Chris Warren
@Institute: Institute for Quantum Computing, University of Waterloo

Calculations of the nonlinear spectrum of the link and plots the eigenenergies
    ,
transition energies, transition matrix elements, and state composition of the
eigenstates
```

```
8
9  Link_Hamiltonian(args): returns the Hamiltonian of the link as a function of
10 flux
11 """
12 import qutip as qt
13 import numpy as np
14 import matplotlib.pyplot as plt
15
16 n = 5              #number of oscillator states
17
18 def Link_Hamiltonian(EjL,EjR,CL,CR,Ej,Cj,phi=0):
19     e_charge = 1.602e-19                    #electron charge
20     h = 6.626e-34                           #planck's constant
21     EJ = Ej*np.abs(np.cos(phi*2*np.pi))  #Link energy
22     C_to_GHz = (e_charge**2)/(h*1e9)      #e^2/(hC) gives frequency in GHz
23     C_det = 1.0/(Cj*CL + Cj*CR + CL*CR)  #Capacitance matrix determinant
24     # Left and Right anharmonicity factor
25     eps_L = 2*np.sqrt((Cj+CR)*C_det*C_to_GHz/(EJ+EjL))
26     eps_R = 2*np.sqrt((Cj+CL)*C_det*C_to_GHz/(EJ+EjR))
27     # Create qubit operators
28     a = qt.tensor(qt.destroy(n),qt.qeye(n))
29     b = qt.tensor(qt.qeye(n),qt.destroy(n))
30     # Harmonic energy scales
31     omega_L = ((EJ+EjL)*eps_L * (2*np.pi))
32     omega_R = ((EJ+EjR)*eps_R * (2*np.pi))
33     H_L = omega_L*a.dag()*a
34     H_R = omega_R*b.dag()*b
35     # Mixing Coefficients (capacitive & inductive)
36     omega_Mcap = (2*np.pi)*(2*Cj*C_det*C_to_GHz/np.sqrt(eps_L*eps_R))
37     omega_Mind = (2*np.pi)*(EJ*np.sqrt(eps_L*eps_R)/2)
38     H_LR = (omega_Mcap*( a.dag()*b - a.dag()*b.dag() + a*b.dag() - a*b )
39             - omega_Mind*( a.dag()*b + a.dag()*b.dag() + a*b.dag() + a*b ))
40     H0 = H_L + H_R + H_LR              #Total first order Hamiltonian
41     # Anharmonic energy scales
42     Omega_L = (2*np.pi)*(eps_L**2/16)*(EjL*np.exp(-eps_L/4)
43                                        + EJ*np.exp(-np.sqrt(eps_L*eps_R)/4))
44     Omega_R = (2*np.pi)*(eps_R**2/16)*(EjR*np.exp(-eps_R/4)
45                                        + EJ*np.exp(-np.sqrt(eps_L*eps_R)/4))
46     Omega_LR = (2*np.pi)*(eps_L*eps_R/4)*(EJ*np.exp(-np.sqrt(eps_L*eps_R)/4))
47     H_int1 = -Omega_L*( (a.dag()**2)*(a**2) )
48     H_int2 = -Omega_R*( (b.dag()**2)*(b**2) )
49     H_int3 = -Omega_LR*( (a.dag()*a) * (b.dag()*b) )
50     H_int = H_int1 + H_int2+ H_int3    #Total Interaction Hamiltonian
51
52     H = H0 + H_int                     #Total Hamiltonian
53     return H
54
55 #=============================================================================
56 #            Generating Calculation Parameters and Storage
57 #=============================================================================
58
59 #Sweep flux through SQUID
60 phi = np.linspace(-0.5,0.5,1001)
61 #Driving Operators
```

```
a = qt.tensor(qt.destroy(n),qt.qeye(n))
b = qt.tensor(qt.qeye(n),qt.destroy(n))
Hopping_a = a+a.dag()                #   (a + adag) X I
Hopping_b = b+b.dag()                #   I X (b + bdag)
#Generate Basis States
gg = qt.tensor(qt.basis(n,0),qt.basis(n,0))
eg = qt.tensor(qt.basis(n,1),qt.basis(n,0))
ge = qt.tensor(qt.basis(n,0),qt.basis(n,1))
ee = qt.tensor(qt.basis(n,1),qt.basis(n,1))
fg = qt.tensor(qt.basis(n,2),qt.basis(n,0))
gf = qt.tensor(qt.basis(n,0),qt.basis(n,2))
#Store basis vectors
basislist = [gg,eg,ge,fg,ee,gf]
#Generate various storage variables
Eval_mat = np.zeros((len(phi),n*n))  #Store eigenvalues
#Create Transition Elements matrices
Eval_mat1a = np.zeros((len(phi),n*n))
Eval_mat2a = np.zeros((len(phi),n*n))
Eval_mat3a = np.zeros((len(phi),n*n))

Eval_mat1b = np.zeros((len(phi),n*n))
Eval_mat2b = np.zeros((len(phi),n*n))
Eval_mat3b = np.zeros((len(phi),n*n))

Eval_mat1c = np.zeros((len(phi),n*n))
Eval_mat2c = np.zeros((len(phi),n*n))
Eval_mat3c = np.zeros((len(phi),n*n))

Eval_mat1d = np.zeros((len(phi),n*n))
Eval_mat2d = np.zeros((len(phi),n*n))
Eval_mat3d = np.zeros((len(phi),n*n))
#Coupling Matrices (CHANGE SIZE TO MATCH Transition_List)
Coupling_matA = np.zeros((len(phi),8))
Coupling_matB = np.zeros((len(phi),8))
Coupling_matC = np.zeros((len(phi),8))
Coupling_matD = np.zeros((len(phi),8))
#Generate matrices to store composition of first 6 eigenstates
EvecMat_gnd = np.zeros((len(phi),6))
EvecMat_first = np.zeros((len(phi),6))
EvecMat_second = np.zeros((len(phi),6))
EvecMat_third = np.zeros((len(phi),6))
EvecMat_fourth = np.zeros((len(phi),6))
EvecMat_fifth = np.zeros((len(phi),6))

#=============================================================
#                    Calculations from Hamiltonian
#=============================================================

for i,Phi in enumerate(phi):
    if (i %((len(phi)-1)/10))==0:
        print('%f Percent Completed' %(i/(len(phi)-1)*100))
    #Compute Hamiltonian as a function of flux
    H = Link_Hamiltonian(17.0,16.0,65e-15,48.8e-15,20.0,40.0e-15,Phi)
    H.tidyup(atol=1e-12)
```

```
    evals,evecs = H.eigenenergies()        #Diagonalize
    #Assign low lying eigen states
    gnd = evecs[0]
    first = evecs[1]
    second = evecs[2]
    third = evecs[3]
    fourth = evecs[4]
    fifth = evecs[5]
    #define transitions
    gnd_to_first = first*gnd.dag()
    gnd_to_second = second*gnd.dag()

    first_to_second = second*first.dag()
    first_to_third = third*first.dag()
    first_to_fourth = fourth*first.dag()
    first_to_fifth = fifth*first.dag()

    second_to_first = first*second.dag()
    second_to_third = third*second.dag()
    second_to_fourth = fourth*second.dag()
    second_to_fifth = fifth*second.dag()

    gnd_to_third = third*gnd.dag()
    gnd_to_fourth = fourth*gnd.dag()
    gnd_to_fifth = fifth*gnd.dag()
    #Calculate occupation probabilities and store them
    for j in range(6):
        Number_gnd = basislist[j].dag()*gnd
        Number_first = basislist[j].dag()*first
        Number_second = basislist[j].dag()*second
        Number_third = basislist[j].dag()*third
        Number_fourth = basislist[j].dag()*fourth
        Number_fifth = basislist[j].dag()*fifth
        EvecMat_gnd[i,j] = np.abs(Number_gnd[0,0])**2
        EvecMat_first[i,j] = np.abs(Number_first[0,0])**2
        EvecMat_second[i,j] = np.abs(Number_second[0,0])**2
        EvecMat_third[i,j] = np.abs(Number_third[0,0])**2
        EvecMat_fourth[i,j] = np.abs(Number_fourth[0,0])**2
        EvecMat_fifth[i,j] = np.abs(Number_fifth[0,0])**2
    #Store evals to plot
    Eval_mat[i,:] = evals
    #Store transition energies between levels
    Eval_mat1a[i,:] = evals - evals[0]
    Eval_mat2a[i,:] = evals - evals[1]
    Eval_mat3a[i,:] = evals - evals[2]

    Eval_mat1b[i,:] = evals - evals[0]
    Eval_mat2b[i,:] = evals - evals[1]
    Eval_mat3b[i,:] = evals - evals[2]
    #Define the transition elements in terms of the eigenstates
    Transition_List = [gnd_to_first,gnd_to_second,
                       first_to_third,first_to_fourth,first_to_fifth,
                       second_to_third,second_to_fourth,second_to_fifth]
    #Calculate transition matrix elements
```

```
    for j in range(len(Transition_List)):
        Coupling_matA[i,j] = np.abs(qt.expect(Hopping_a,Transition_List[j]))
        Coupling_matB[i,j] = np.abs(qt.expect(Hopping_b,Transition_List[j]))
    cutoff = 0.04
    #Calculate which transtion element is below cutoff
    if Coupling_matA[i,0]/(2*np.pi) < cutoff:
        Eval_mat1a[i,1] = np.nan
    if Coupling_matA[i,1]/(2*np.pi) < cutoff:
        Eval_mat1a[i,2] = np.nan
    if Coupling_matA[i,2]/(2*np.pi) < cutoff:
        Eval_mat2a[i,3] = np.nan
    if Coupling_matA[i,3]/(2*np.pi) < cutoff:
        Eval_mat2a[i,4] = np.nan
    if Coupling_matA[i,4]/(2*np.pi) < cutoff:
        Eval_mat2a[i,5] = np.nan
    if Coupling_matA[i,5]/(2*np.pi) < cutoff:
        Eval_mat3a[i,3] = np.nan
    if Coupling_matA[i,6]/(2*np.pi) < cutoff:
        Eval_mat3a[i,4] = np.nan
    if Coupling_matA[i,7]/(2*np.pi) < cutoff:
        Eval_mat3a[i,5] = np.nan

    if Coupling_matB[i,0]/(2*np.pi) < cutoff:
        Eval_mat1b[i,1] = np.nan
    if Coupling_matB[i,1]/(2*np.pi) < cutoff:
        Eval_mat1b[i,2] = np.nan
    if Coupling_matB[i,2]/(2*np.pi) < cutoff:
        Eval_mat2b[i,3] = np.nan
    if Coupling_matB[i,3]/(2*np.pi) < cutoff:
        Eval_mat2b[i,4] = np.nan
    if Coupling_matB[i,4]/(2*np.pi) < cutoff:
        Eval_mat2b[i,5] = np.nan
    if Coupling_matB[i,5]/(2*np.pi) < cutoff:
        Eval_mat3b[i,3] = np.nan
    if Coupling_matB[i,6]/(2*np.pi) < cutoff:
        Eval_mat3b[i,4] = np.nan
    if Coupling_matB[i,7]/(2*np.pi) < cutoff:
        Eval_mat3b[i,5] = np.nan

#=============================================================================
#    Visualization of Results (Comment/Uncomment to plot sections)
#=============================================================================
#Plot Energy Levels of the Hamiltonian as a function of flux
for i in range(21):
    plt.plot(phi,Eval_mat[:,i]/(2*np.pi))
plt.ylabel(r'Freqnecy [GHz]',fontsize=15)
plt.xlabel(r'$\Phi/2\pi$',fontsize=15)
plt.title(r'Total Energy Spectrum',fontsize=15)
plt.grid()
plt.annotate(r'$N=0$',xy=(0.45,0))
plt.annotate(r'$N=1$',xy=(0.45,8))
plt.annotate(r'$N=2$',xy=(0.45,15.4))
plt.annotate(r'$N=3$',xy=(0.45,22.5))
plt.show()
```

```
#Plot Transition Energies
#Gnd -> Single Excitation manifold
plt.plot(phi,(Eval_mat1a[:,1])/(2*np.pi),'b')
plt.plot(phi,(Eval_mat1b[:,1])/(2*np.pi),'b')
plt.plot(phi,(Eval_mat1a[:,2])/(2*np.pi),'r')
plt.plot(phi,(Eval_mat1b[:,2])/(2*np.pi),'r')
plt.ylabel(r'Freqnecy [GHz]',fontsize=14)
plt.xlabel(r'$\Phi/2\pi$',fontsize=14)
plt.title(r'Transition Energies of Ground/Single Manifold',fontsize=12)
plt.grid()
plt.show()
#Single Excitation -> double manifold
plt.plot(phi,(Eval_mat2a[:,3])/(2*np.pi),'b--')
plt.plot(phi,(Eval_mat2b[:,3])/(2*np.pi),'b--')
plt.plot(phi,(Eval_mat2a[:,4])/(2*np.pi),'r--')
plt.plot(phi,(Eval_mat2b[:,4])/(2*np.pi),'r--')
plt.plot(phi,Eval_mat3a[:,4]/(2*np.pi),'r-.')
plt.plot(phi,Eval_mat3b[:,4]/(2*np.pi),'r-.')
plt.plot(phi,Eval_mat3a[:,5]/(2*np.pi),'g-.')
plt.plot(phi,Eval_mat3b[:,5]/(2*np.pi),'g-.')
plt.ylabel(r'Freqnecy [GHz]',fontsize=14)
plt.xlabel(r'$\Phi/2\pi$',fontsize=14)
plt.title(r'Transition Energies of Single/Double Manifold',fontsize=12)
plt.grid()
plt.show()
#Plot Transition Matrix Elements
#Change second index to plot various transitions corresponding to
#transition_list
# a + a^dag
plt.plot(phi,Coupling_matA[:,0]/(2*np.pi),'b')
plt.plot(phi,Coupling_matA[:,1]/(2*np.pi),'r')
plt.plot(phi,Coupling_matA[:,2]/(2*np.pi),'g')
plt.ylabel(r'Frequency [GHz]',fontsize=15)
plt.xlabel(r'$\Phi/2\pi$',fontsize=15)
plt.title(r'$<\psi_{i}|(a+a^{\dagger})\otimes \mathbb{1}|\psi_{j}>$',
          fontsize=20)
plt.plot([-0.5,0.5],[0.005,0.005],'k--')
plt.legend([r'$|\psi_{g}> \rightarrow |\psi_{1}>$',
            r'$|\psi_{g}> \rightarrow |\psi_{2}>$',
            r'$|\psi_{1}> \rightarrow |\psi_{2}>$',
            r'Threshold'],loc='upper right',fontsize=12)
plt.grid()
plt.show()
# b + b^dag
plt.plot(phi,Coupling_matB[:,0]/(2*np.pi),'b')
plt.plot(phi,Coupling_matB[:,1]/(2*np.pi),'r')
plt.plot(phi,Coupling_matB[:,2]/(2*np.pi),'g')
plt.ylabel(r'Frequency [GHz]',fontsize=15)
plt.xlabel(r'$\Phi/2\pi$',fontsize=15)
plt.title(r'$<\psi_{i}|\mathbb{1}\otimes (b+b^{\dagger})|\psi_{j}>$',
          fontsize=20)
plt.plot([-0.5,0.5],[0.005,0.005],'k--')
plt.legend([r'$|\psi_{g}> \rightarrow |\psi_{1}>$',
            r'$|\psi_{g}> \rightarrow |\psi_{2}>$',
```

```
            r'$|\psi_{1}> \rightarrow |\psi_{2}>$',
            r'Threshold'],loc='upper right',fontsize=12)
#Eigenstate probabilities
#Change EvecMat_blah[:,i] to plot the composition of the various levels
for i in range(6):
    plt.plot(phi,EvecMat_gnd[:,i])
plt.grid()
plt.title(r'Composition of Ground State',fontsize=15)
plt.legend([r'|gg>',r'|eg>',r'|ge>',r'|ee>',r'|fg>',r'|gf>'],loc='upper right'
    ,
           fontsize=12)
plt.ylabel(r'Occupation Probability',fontsize=15)
plt.xlabel(r'$\Phi/2\pi$',fontsize=15)
plt.show()
```

A.3 Time Domain Calculations

```
"""
@author: Chris Warren
@Institute: Institute for Quantum Computing, University of Waterloo

Calculate the time evolution of the full four qubit Hamiltonian and
various observables of interest such as occupation probability and
occupation number with decoherence

FourQubit(args): Calculate the Hamiltonian of the full four qubit device
                takes a keyword argument inres to determine whether the
                two matter qubits start in resonance or are pulsed into
                resonance later
"""
import qutip as qt
import numpy as np
import matplotlib.pyplot as plt
import datetime as dt

n = 4
def FourQubit(wq1,wq2,lambda1,lambda2,EjL,EjR,CL,CR,Ej,Cj,phi=0,inres=True):
    #Constants
    e_charge = 1.602e-19                #electron charge
    h = 6.626e-34                       #planck's constant
    EJ = Ej*np.abs(np.cos(phi*2*np.pi))
    C_to_GHz = (e_charge**2)/(h*1e9)    # e^2/(hC)  gives frequency in GHz
    C_det = 1.0/(Cj*CL + Cj*CR + CL*CR)
    eps_L = 2*np.sqrt((Cj+CR)*C_det*C_to_GHz/(EJ+EjL))
    eps_R = 2*np.sqrt((Cj+CL)*C_det*C_to_GHz/(EJ+EjR))
    # Qubit Operators
    sm1 = qt.tensor([qt.destroy(2),qt.qeye(n),qt.qeye(n),qt.qeye(2)])
    sm2 = qt.tensor([qt.qeye(2),qt.qeye(n),qt.qeye(n),qt.destroy(2)])
    a = qt.tensor([qt.qeye(2),qt.destroy(n),qt.qeye(n),qt.qeye(2)])
    b = qt.tensor([qt.qeye(2),qt.qeye(n),qt.destroy(n),qt.qeye(2)])
    # Harmonic energy scales
    omega_L = ((EJ+EjL)*eps_L * (2*np.pi))
    omega_R = ((EJ+EjR)*eps_R * (2*np.pi))
```

```
    H_L = omega_L*a.dag()*a
    H_R = omega_R*b.dag()*b
    # Mixing Coefficients (capacitive & inductive)
    omega_Mcap = (2*np.pi)*(2*Cj*C_det*C_to_GHz/np.sqrt(eps_L*eps_R))
    omega_Mind = (2*np.pi)*(EJ*np.sqrt(eps_L*eps_R)/2)
    H_LR = (omega_Mcap*( a.dag()*b - a.dag()*b.dag() + a*b.dag() - a*b )
            - omega_Mind*( a.dag()*b + a.dag()*b.dag() + a*b.dag() + a*b ))
    H_HarmLink = H_L + H_R + H_LR
    # Anharmonic Link elements
    Omega_L = (2*np.pi)*(eps_L**2/16)*(EjL*np.exp(-eps_L/4)
                                       + EJ*np.exp(-np.sqrt(eps_L*eps_R)/4))
    Omega_R = (2*np.pi)*(eps_R**2/16)*(EjR*np.exp(-eps_R/4)
                                       + EJ*np.exp(-np.sqrt(eps_L*eps_R)/4))
    Omega_LR = (2*np.pi)*(eps_L*eps_R/4)*(EJ*np.exp(-np.sqrt(eps_L*eps_R)/4))
    H_int1 = -Omega_L*( (a.dag()**2)*(a**2) )
    H_int2 = -Omega_R*( (b.dag()**2)*(b**2) )
    H_int3 = -Omega_LR*( (a.dag()*a) * (b.dag()*b) )
    H_AnharmLink = H_int1 + H_int2+ H_int3
    # Total Link Hamiltonian
    H_link = H_HarmLink + H_AnharmLink
    #Matter Qubits (check if in resonance with link or if pulsed)
    if inres:
        wq1 = omega_L
        wq2 = omega_R
    else:
        wq1 = wq1*2*np.pi
        wq2 = wq2*2*np.pi
    Hqb = (wq1)*sm1.dag()*sm1 + (wq2)*sm2.dag()*sm2
    H0 = Hqb + H_link
    #JC-like coupling
    H_lambda = ( (2*np.pi*lambda1)*(sm1.dag()*a + sm1*a.dag())
                +(2*np.pi*lambda2)*(sm2.dag()*b + sm2*b.dag()))
    #Total Hamiltonian
    H = H0 + H_lambda
    return H,Hqb,omega_L,omega_R

H_nopulse,Hqb,omega_L,omega_R = FourQubit(6,6.4,          #qubit frequencies
                                          0.1,0.1,        #coupling energies
                                          17.0,16.0,      #EjL, EjR
                                          65e-15,48.8e-15, #C_L, C_R
                                          20.0,40.0e-15,  #EJ, CJ
                                          -0.151,         #flux
                                          inres=True)
#Time dynamics of IN RESONANCE Hamiltonian
tlist = np.linspace(0,400,1001)
evals,evecs = H_nopulse.eigenstates()
#Initial State
psi_0 = qt.tensor([qt.basis(2,1),qt.basis(n,0),qt.basis(n,1),qt.basis(2,0)])
#Initialize various basis states of interest
psi0000 = qt.tensor(qt.basis(2,0),qt.basis(n,0),qt.basis(n,0),qt.basis(2,0))
psi1010 = qt.tensor(qt.basis(2,1),qt.basis(n,0),qt.basis(n,1),qt.basis(2,0))
psi0101 = qt.tensor(qt.basis(2,0),qt.basis(n,1),qt.basis(n,0),qt.basis(2,1))

psi1110 = qt.tensor(qt.basis(2,1),qt.basis(n,1),qt.basis(n,1),qt.basis(2,0))
```

```
psi0201 = qt.tensor(qt.basis(2,0),qt.basis(n,2),qt.basis(n,0),qt.basis(2,1))
psi0111 = qt.tensor(qt.basis(2,0),qt.basis(n,1),qt.basis(n,1),qt.basis(2,1))
psi1020 = qt.tensor(qt.basis(2,1),qt.basis(n,0),qt.basis(n,2),qt.basis(2,0))
#2D Param
#phi_list = np.linspace(-0.16,-0.14,201)   #If 2D is wanted
#Sz_2D = np.zeros((len(phi_list),len(tlist)))
#Initialize lists to contain observables and collapse ops
e_ops = []
c_ops = []
#Projectors onto single excitation manifold of interest
e_ops.append(psi1010*psi1010.dag())
e_ops.append(psi0101*psi0101.dag())
#Create occupation number observables
sm1 = qt.tensor([qt.destroy(2),qt.qeye(n),qt.qeye(n),qt.qeye(2)])
sm2 = qt.tensor([qt.qeye(2),qt.qeye(n),qt.qeye(n),qt.destroy(2)])
a = qt.tensor([qt.qeye(2),qt.destroy(n),qt.qeye(n),qt.qeye(2)])
b = qt.tensor([qt.qeye(2),qt.qeye(n),qt.destroy(n),qt.qeye(2)])

e_ops.append(sm1.dag()*sm1)
e_ops.append(sm2.dag()*sm2)
e_ops.append(a.dag()*a)
e_ops.append(b.dag()*b)
#Create Collapse rates for each element in GHz
kappa1 = 0.0005
kappa2 = 0.0005
kappa3 = 0.0005
kappa4 = 0.0005

c_ops.append(np.sqrt(kappa1)*a)
c_ops.append(np.sqrt(kappa2)*b)
c_ops.append(np.sqrt(kappa3)*sm1)
c_ops.append(np.sqrt(kappa4)*sm2)
#run time domain simulation
result = qt.mesolve(H_nopulse,psi_0,tlist,c_ops,e_ops,progress_bar=True)
#save results in qutip format
today = dt.datetime.now()
qt.fileio.qsave(result, 'NoPulseTimeDomain_{}{}{}'.format(today.year,
                                                          today.month,
                                                          today.day) )
#Plot results
plt.plot(result.times,result.expect[0])
plt.plot(result.times,result.expect[1])
plt.ylabel(r'Occupation Probability',fontsize=15)
plt.xlabel(r'Time [ns]',fontsize=15)
plt.title(r'Initial State $|\uparrow 0 1 \downarrow>$',fontsize=18)
plt.legend([r'$|\uparrow 01\downarrow>$',
            r'$|\downarrow 10 \uparrow>$'],
            loc='upper right',fontsize=12)
plt.ylim([0,1])
plt.grid()
plt.show()
#Plot Occupation Number
plt.plot(result.times,result.expect[2])
plt.plot(result.times,result.expect[3])
```

```
plt.plot(result.times,result.expect[4])
plt.plot(result.times,result.expect[5])
plt.xlabel(r'Time [ns]',fontsize=15)
plt.ylabel(r'Excitation Number',fontsize=15)
plt.title(r'Initial State $|\uparrow 0 1 \downarrow>$',fontsize=18)
plt.legend([r'$<\sigma^{+}_{1} \sigma^{-}_{1}>$',
            r'$<\sigma^{+}_{2}\sigma^{-}_2>$',
            r'$<a^{+} a>$',r'$<b^{+} b>$'],
            fontsize=12,loc='upper right')
plt.ylim([0,2])
plt.grid()
plt.show()

#Pulsed Time Dynamics of out of resonance Hamiltonian
H_pulse,Hqb,omega_L,omega_R = FourQubit(6,6.4,          #qubit frequencies
                                        0.1,0.1,        #coupling energies
                                        17.0,16.0,      #EjL, EjR
                                        65e-15,48.8e-15, #C_L, C_R
                                        20.0,40.0e-15,  #EJ, CJ
                                        -0.151,         #flux
                                        inres=False)
evals,evecs = H_pulse.eigenstates()
psi0 = evecs[0] # Initialize in the ground state of the system
##Find the state that mostly corresponds to a particular transition
#State_of_Interst = qt.tensor([qt.basis(2,1),
#                              qt.basis(n,0),
#                              qt.basis(n,1)
#                              ,qt.basis(2,0)])
#for i,evec in enumerate(evecs):
#    print(i,blah.dag()*evec)
## Evecs[8] corresponds mostly to the state  |1010>
## Want to drive the transition between |1000> and |1010>
omega_dr = np.abs(evals[8]-evals[1])
#Initialize various states in the manifold of interest
psi_1 = qt.tensor([qt.basis(2,1),qt.basis(n,0),qt.basis(n,0),qt.basis(2,0)])
psi_2 = qt.tensor([qt.basis(2,0),qt.basis(n,0),qt.basis(n,1),qt.basis(2,0)])
psi_3 = qt.tensor([qt.basis(2,1),qt.basis(n,0),qt.basis(n,1),qt.basis(2,0)])
psi_4 = qt.tensor([qt.basis(2,0),qt.basis(n,1),qt.basis(n,0),qt.basis(2,1)])
#set master equation options to store final state for fidelity calc
opts = qt.Options(max_step=0.01,nsteps=100000,store_final_state=True)
# Find qubit drive frequency before being brought into res
wq1 = np.abs(evals[1]-evals[0])
# Create driving coefficients
#Can change the overlap by changing (t-t0) in Gaussian
def Pulse_Coeff1(t,args):
    HWHM = args['HWHM']
    sigma = HWHM/np.sqrt(2*np.log(2))
    A = np.sqrt(np.pi*np.log(2))/HWHM
    f = A*np.exp(-((t-20)/sigma)**2/2)*(np.sin(wq1*t))
    return f

def Pulse_Coeff2(t,args):
    HWHM = args['HWHM']
    sigma = HWHM/np.sqrt(2*np.log(2))
```

```
    A = np.sqrt(np.pi*np.log(2))/HWHM
    f = A*np.exp(-((t-50)/sigma)**2/2)*(np.sin(omega_dr*t))
    return f

def step(t,args):
    t0 = args['t0']
    return 1*(t>t0)

HWHM = 5    #Gaussian pulse HWHM
t0 = 50     #step function start time to bring into resonance

args = {'HWHM':HWHM,'t0':50}
#Collapse operators, comment out to select which you want
#c_ops = [np.sqrt(0.002)*sm1,
#         np.sqrt(0.002)*a,
#         np.sqrt(0.002)*b,
#         np.sqrt(0.002)*sm2]
c_ops = []
# Create drive Hamiltonians for 0000->1000
H1 = sm1+sm1.dag()
# Selectively drive state 1000->1010
state1 = evecs[1]
state2 = evecs[8]
state1_to_state2 = state2*state1.dag()
H2 = state1_to_state2.dag() + state1_to_state2
# Bring Qubits back into resonance with adjacent link
H3 =  omega_L*sm1.dag()*sm1 + omega_R*sm2.dag()*sm2 - Hqb
#Define time-dependent Hamiltonians
#w/ final z-pulse
#H = [H_pulse,[H1,Pulse_Coeff1],[H2,Pulse_Coeff2],[H3,step]]
#w/o final z-pulse
H = [H_pulse,[H1,Pulse_Coeff1],[H2,Pulse_Coeff2]]
#Run time dynamics
tlist = np.linspace(0,100,201)

e_ops = [psi_1*psi_1.dag(),
         psi_2*psi_2.dag(),
         psi_3*psi_3.dag(),
         psi_4*psi_4.dag(),
         psi0*psi0.dag()]
e_ops.append(sm1.dag()*sm1)
e_ops.append(a.dag()*a)
e_ops.append(b.dag()*b)
e_ops.append(sm2.dag()*sm2)
output = qt.mesolve(H,psi0,tlist,
                    c_ops,e_ops,
                    args=args,
                    progress_bar=True,
                    options=opts)
qt.fileio.qsave(output,'Pulsed_TimeDomain_{}{}{}'.format(today.year,
                                                         today.month,
                                                         today.day) )
# Compute fidelity of state of interest
psi_f = qt.tensor(qt.basis(2,1),qt.basis(n,0),qt.basis(n,1),qt.basis(2,0))
```

```
A = psi_f*psi_f.dag()
B = output.final_state*output.final_state.dag()
print(qt.fidelity(A,B))
#Plot occupation probabilities
plt.plot(output.times,output.expect[0])
plt.plot(output.times,output.expect[1])
plt.plot(output.times,output.expect[2])
plt.plot(output.times,output.expect[3])
plt.plot(output.times,output.expect[4])
plt.xlabel(r'Time [ns]',fontsize=15)
plt.ylabel(r'Occupation Probability',fontsize=15)
plt.title(r'Pulsed Gauge Invariant Dynamics',fontsize=15)
plt.legend([r'1000',
            r'0010',
            r'1010',
            r'0101',
            'gnd'],
            loc='upper right',fontsize=12)
plt.grid()
plt.show()
#Plot Occupation Numbers
plt.plot(output.times,output.expect[5])
plt.plot(output.times,output.expect[6])
plt.plot(output.times,output.expect[7])
plt.plot(output.times,output.expect[8])
plt.xlabel(r'Time [ns]',fontsize=15)
plt.ylabel(r'Excitation Number',fontsize=15)
plt.title(r'Pulsed Gauge Invariant Dynamics',fontsize=15)
plt.legend([r'$<\sigma^{+}_{1} \sigma^{-}_{1}>$',
            r'$<a^{+} a>$',
            r'$<b^{+} b>$',
            r'$<\sigma^{+}_{2}\sigma^{-}_2>$'],
            fontsize=12,loc='upper right')
plt.grid()
plt.show()
```

Appendix B

Fabrication Recipe

1. **Wafer Cleaning**
    - Piranha cleaning 15min (4:1 ratio of $H_2SO_4 : H_2O_2$)
    - DI water soak 5min
    - Quick dump rinse & spin rinse dryer
    - HF-dip clean 90s (2% solution)
    - DI water soak 5min ($\times$3, new water each time)
    - YES-ash ashing cycle to clean leftover organic material
    - Acetone bath @ 40C with sonication, 10min
    - IPA bath @ 40C with sonication, 10min
    - Rinse fresh IPA, 1min
2. **Marker Layer (Palladium)**
    - Wafer dehyration in Fisher oven @ 200C for 10min
    - YES-HMDS oven to prime surface for vapor deposition
    - Spin PMGI SF7, 5000RPM for 60s
    - Bake @ 140C for 90s
    - Spin S1811, 5000RPM for 60s
    - Bake @ 110C for 90s
    - Expose under mask aligner 4s, vacuum contact, UV 405nm, 25mW/cm^2
    - Develop resist in MF-319
    - Stop developer in DI water ($\times$2), 30s
    - Yes-ash descum (plasma ashing), 20s
    - E-beam evaporator (Intlvac-Ebeam) Ti/Pd, 5nm/100nm
    - Lift-off with PG-remover @ 80C, $\sim$45min or overnight cold lift-off

- IPA clean, 5min

3. **Circuit Layer (Aluminum)**
   - YES-ash descum
   - Repeat wafer dehydration and YES-HMDS priming
   - Spin MaN-1410, 3000RPM for 60s
   - Bake @ 100C for 90s
   - Expose under mask aligner 20s, vacuum contact, UV 365nm, 10mW/cm^2
   - Develop resist in MaD 533S, 120s
   - Stop developer in DI water ($\times$2), 30s
   - YES-ash descum, 20s
   - E-beam evaporator (Intlvac-Ebeam or Plassys) Al, 70-100nm (pump overnight in Intlvac down to 1×10^{-7} torr)
   - Lift-off in PG Remover @ 80C, 1h (agitate to remove ground squares)
   - Warm IPA bath, 15min (agitate)
   - Clean IPA bath 5min
4. **Wafer Dicing**
   - Spin S1811, 5000RPM for 60s
   - Soft bake @ 50C
   - Dice wafer leaving 100μm of chip
   - Break and clean blocks in DI water then acetone & IPA
5. **Qubit Layer (Aluminum)**
   - Clean bloack in warm acetone and IPA
   - Spin PMGI SF11, 500RPM for 5s, 2800RPM for 50s
   - Bake @ 220C for 15min
   - Spin PMMA, 500RPM for 5s, 6000RPM for 60s
   - Bake @ 210C for 15min
   - Write with e-beam (RAITH), coarse features with 60μm aperture and 15kV beam @ 150μC/cm^2 dose, fine features with 10μm aperture and 25kV beam @ 250μC/cm^2 dose
   - Develop PMMA with MIBK:IPA 1:3 for 60s then stop in IPA for 30s
   - Develop PMGI with Microposite Developer Concentrate for 35s, stop in DI water ($\times$2) for 30s then 10s
   - Load in double angle evaporator and pump down pressure

- Argon milling 11s
- Evaporate aluminum at first angle to 40nm
- Oxidation @ 25 torr for 15min
- Evaporate aluminum at second angle to 60nm
- Lift-off with PG Remover @ 80C for 30min
- Warm IPA bath at 40C for 5 min, clean IPA 1min

6. **Device Dicing**

- Spin PMMA A5
- Bake @ 100C for 5min
- Dice chip leaving 100μm
- Clean device in DI, then warm acetone (10min) and IPA (10min)